MANTLE HETEROGENEITY AND THE ORIGINS OF PRIMITIVE ARC LAVAS: AN EXPERIMENTAL STUDY WITH A FOCUS ON THE TRANS-MEXICAN VOLCANIC BELT

by

STEPHANIE LEIGH WEAVER

A DISSERTATION

Presented to the Department of Geological Sciences
and the Graduate School of the University of Oregon
in partial fulfillment of the requirements
for the degree of
Doctor of Philosophy

September 2012

DISSERTATION APPROVAL PAGE

Student: Stephanie Leigh Weaver

Title: Mantle Heterogeneity and the Origins of Primitive Arc Lavas: An Experimental Study with a Focus on the Trans-Mexican Volcanic Belt

This dissertation has been accepted and approved in partial fulfillment of the requirements for the Doctor of Philosophy degree in the Department of Geological Sciences by:

Paul J. Wallace	Co-Chair
A. Dana Johnston	Co-Chair
Alan Rempel	Member
Darren Johnson	Outside Member

and

Kimberly Andrews Espy	Vice President for Research & Innovation/Dean of the Graduate School

Original approval signatures are on file with the University of Oregon Graduate School.

Degree awarded September 2012

DISSERTATION ABSTRACT

Stephanie Leigh Weaver

Doctor of Philosophy

Department of Geological Sciences

September 2012

Title: Mantle Heterogeneity and the Origins of Primitive Arc Lavas: An Experimental Study with a Focus on the Trans-Mexican Volcanic Belt

Primitive, mantle-derived magmas provide important clues about the formation and equilibration conditions of magmas at depth. In subduction zones, it is uncommon for primitive magmas to ascend through the shallow mantle and crust without undergoing chemical modification. Instead, magmas commonly differentiate through fractional crystallization, crustal assimilation, or magma mixing. Those rare primitive lavas that do erupt along a volcanic arc are useful for elucidating subduction-related processes within the mantle wedge (~30-80 km depth) and are the focus of this research.

I used piston-cylinder apparatuses to investigate the high-pressure, high-temperature, H_2O-undersaturated phase equilibria for several primitive compositions that have erupted at volcanic arcs. I aimed to reveal the permissible residual mantle mineralogy, as well as the P-T-H_2O conditions over which the putative mantle melts last equilibrated before erupting. My work focuses on the Trans-Mexican Volcanic Belt (TMVB), where primitive compositions span a range of SiO_2, total alkalies (K_2O+Na_2O), magmatic H_2O, and incompatible trace element enrichments. Variations among these components are presumed to result from melting heterogeneous mantle that has been affected, to varying degrees, by a subduction component. Chapter III focuses on the

phase equilibria of a Mexican basaltic andesite and an Aleutian basalt. Results show that hydrous basaltic andesite equilibrated with harzburgite in the shallow mantle, whereas the basalt equilibrated with lherzolite. The former appears more common in continental arcs and the latter in intraoceanic arcs. Chapter IV focuses on two alkaline lavas of varying K_2O content from the TMVB that are transitional between potassic, hydrous minette and H_2O-poor intraplate alkali basalt. Experimental phase relations and trace element modeling reveals that melting and/or mixing of peridotite and clinopyroxene-rich veins are likely involved in producing these transitional lava types.

These experimental data are integrated with other petrologic and geophysical data to provide an along-arc perspective of mantle-melt equilibration in the TMVB. Primitive melts appear to commonly equilibrate with chemically heterogeneous mantle at depths above the “hot nose” of the mantle wedge. It is apparent that the shallow mantle wedge is a key component for understanding the geochemical complexities of subduction zone magmas.

This dissertation includes previously published and unpublished co-authored material.

CURRICULUM VITAE

NAME OF AUTHOR: Stephanie Leigh Weaver

GRADUATE AND UNDERGRADUATE SCHOOLS ATTENDED:

University of Oregon, Eugene
James Madison University, Harrisonburg, VA
University of Florida, Gainesville

DEGREES AWARDED:

Doctor of Philosophy, Geological Sciences, 2012, University of Oregon
Master of Science, Geological Sciences, 2007, University of Oregon
Bachelor of Science, Geology, 2003, James Madison University

AREAS OF SPECIAL INTEREST:

Experimental Igneous Petrology
Subduction Zone Processes
Experimental/Physical Rock Mechanics

PROFESSIONAL EXPERIENCE:

Staff Geologist, Kennec Inc., 2008

Secondary (9-12) Earth and Space Science Teacher, Prince William County Public Schools, 2003-2005

GRANTS, AWARDS, AND HONORS:

Johnston Scholarship, Department of Geological Sciences, University of Oregon, 2012

Marthe E. Smith Memorial Science Scholarship, College of Arts and Sciences, University of Oregon, 2011-2012

Staples Fellowship, Department of Geological Sciences, University of Oregon, 2007, 2011

University of Oregon Doctoral Dissertation Award (departmental nominee), 2011

Graduate Research Award, Department of Geological Sciences, University of Oregon, 2007

Wilbur T. Harnsberger Field Scholarship, James Madison University, 2003

NSF-REU Researcher, Center for Materials Science, James Madison University, 2003

PUBLICATIONS:

Weaver SL, Wallace PJ, Johnston AD (2011) A comparative study of continental vs. intraoceanic arc mantle melting: Experimentally determined phase relations of hydrous, primitive melts. Earth Planet Sci Lett 308: 97–106

Rempel AW, Weaver SL (2008) A model for flash weakening by asperity melting during high-speed earthquake slip. J Geophys Res doi: 10.1029/2008JB005649

Amenta RV, Ewing AM, Jenson A, Roberts S, Stevens K, Summa M**,** Weaver S, Wertz, P (2007) A modeling approach to understanding the role of microstructure development on crystal size distributions and on recovering crystal size distributions from thin slices. Am Min 92:1936–1945

ACKNOWLEDGMENTS

The development and completion of this dissertation is because of the incredible professional and personal support I have received over the years. I owe much gratitude to both of my academic advisors, Dana Johnston and Paul Wallace, who welcomed me back to the department to "finish what I started" several years prior. Without their encouragement and financial support, I would not have been able to achieve this goal. Dana consistently conveyed trust in my academic abilities and allowed me the freedom needed to become an independent scientist. I am grateful for his open-door policy even when his career took him across campus and out of the lab. Although Paul's deep understanding of geochemistry and petrology were essential for my success, his patience, optimism, and enthusiasm for all things Mexico (from cinder cones to tequila) were the keys to my maintaining a positive attitude through the more difficult days. Thanks to Alan Rempel for introducing me to the rock mechanics community and for encouraging me to seek projects with an interdisciplinary focus. John Logan acted as an unofficial advisor and provided encouragement and valuable career advice. I also thank Scott Eaton for his friendship and guidance over the past ten years. Thanks to the UO Geology department faculty and staff, especially Dave Stemple. I will greatly miss our daily office visits and silly banter.

Many people have helped with the nuts-and-bolts of data collection: Dave Senkovich readily worked his magic in the lab as he defied the lab "gremlins" and their attempts at experimental sabotage; John Donovan provided his assistance on the electron microprobe; Hannah Grist and Helen Metts spent many hours making furnace parts; and Celestine Mercer and Rachel Weber were valuable lab mates. Thanks to Gordon Moore

and Terry Plank for their constructive reviews of Chapter III, and additional thanks to Gordon for the experimental advice over the years. I am grateful for the many brain-stretching scientific discussions with DoGS faculty and students, particularly Gene Humphreys, Brandon Schmandt, Leland O'Driscoll, Kathy Cashman, and Ilya Bindeman.

I am thankful for many Eugene friends who made my graduate years memorable. The members (old and new) of Friday Breakfast Club understood the soothing properties of waffles and bacon and appreciated that pineapple is the only acceptable fruit option. Nick Deardorff and Ben Mackey were regular sources of entertainment and great friends who I miss dearly. Jenna Fribley, Shannon Oliver, Carrie Kehrein, and the rest of the JHMT led me to sanity during Sunday long runs and the post-run pastry/coffee face-stuffings. My girlfriends Emily Johnson, Celeste Mercer, Christine Metzger and Emily Gottesfeld are like sisters to me and continue to provide much needed laughs, wine, crazy cat stories, and sound scientific and life advice when needed.

Thank you to Steve, who has been an incredible partner through this whole experience. We completed our dissertations side-by-side and managed to remain positive and supportive for each other through it all. His love, encouragement, strength, and superior culinary skills kept me motivated, and I look forward to conquering more of life's challenges together in the future. Finally, thank you to my parents and my brother for keeping me grounded by making me laugh and always reminding me of what is really important.

For the late Dr. Roddy V. Amenta, Professor Emeritus, James Madison University.
Your wicked sense of humor and sharp scientific mind will forever be with me

TABLE OF CONTENTS

Chapter Page

Chapter Page

Chapter Page

LIST OF FIGURES

Figure Page

Figure Page

LIST OF TABLES

CHAPTER I

INTRODUCTION

General Overview

The way geologists view the earth was revolutionized in the mid 20th century as researchers discovered that new oceanic crust is created at spreading ridges and destroyed during subduction at convergent margins. Subduction of the dense oceanic lithosphere causes deep seismicity, large-magnitude earthquakes, and significant tsunami hazards (most recently in Sumatra [2005], Chile [2010], and Tohoku, Japan [2011]). Moreover, subduction processes are responsible for the formation of both continental margin (Cascades, Andes) and island arc (western Aleutians, Philippines) volcanoes. Magma genesis in subduction zones is among the most complex processes occurring on earth. In these systems, minerals in the downgoing plate may change in composition or structure, dehydrate, and/or partially melt as they undergo a complex series of metamorphic reactions (e.g., Schmidt and Poli 1998). Slab fluids or melts rich in volatiles (H_2O, CO_2, F, Cl, S) and trace elements percolate into the overlying mantle wedge and initiate partial melting.

Recent efforts by geochemists and geophysicists have made significant progress toward understanding the processes that influence magma genesis. These efforts include modeling the thermal state of the downgoing and overriding plates (Peacock et al. 1994; van Keken et al. 2002; Abers et al. 2006), determining metamorphic mineral stabilities with increasing pressure and temperature (Schmidt and Poli 1998; Hacker et al. 2003a), and quantifying the effects of volatiles on mantle melting behavior (Gaetani and Grove 1998; Liu et al. 2006; Médard and Grove 2008). Most mantle-derived (i.e., primary)

magmas will undergo significant chemical modification upon their ascent from their mantle sources (either by fractionating crystallizing minerals, mixing with other magmas, and assimilating surrounding crust; see Figure 1, #4). Consequently, few magmas erupted at the surface will retain information about their origins within in the mantle. Those rare magmas that do erupt at the surface as near-primary, or *primitive* magmas can be used to infer details about processes that occur at depth. My research focuses on these rare, primitive magmas in an effort to address some outstanding questions pertaining to magma genesis in subduction zones. How does the thermal state of the subducted slab affect the behavior of fluids as they percolate through the wedge and induce melting? How do chemical heterogeneities in the mantle affect the compositions of primitive melts from which more evolved melts are derived? What are the fates of initial mantle melts from the time they form at depths of ~80-100 km, to the time they reach the uppermost mantle (30-45 km), and eventually the surface? The research in this dissertation uses an experimental approach to address these questions. I use high-pressure, high-temperature mineral-melt phase equilibrium relations to investigate how mantle heterogeneity (with respect mineralogy), enrichment by slab-derived fluids or melts, and lateral or vertical temperature gradients promote chemical diversity of primitive magmas.

Subduction Zone Volcanism

It is well established that H_2O-rich fluids from the subducted plate plays a crucial role in mafic magma genesis within the mantle wedge beneath arcs. Experimental studies have shown that the introduction of a slab-derived, hydrous fluid or melt significantly lowers the peridotite solidus (e.g., Kushiro 1969b; Kushiro 1972; Nicholls and Ringwood 1973) and induces partial melting in the mantle wedge. One model holds that as hydrous

fluids are released from the downgoing plate (Figure 1, #1), melting is initiated deep in the wedge at the H_2O-saturated solidus. These melts rise through an inverted geothermal gradient in the wedge, where they become diluted in H_2O as additional melt is added from the hotter, shallower mantle. The now H_2O-*under*saturated magmas may then reequilibrate with surrounding mantle (Grove et al. 2006) (Figure 1, #2-3). The details of this process—particularly with respect to reequilibration in the shallow mantle—remain poorly understood. Much of the experimental work to date has focused on magma genesis either under anhydrous conditions now no longer considered to be relevant, or at the H_2O-saturated solidus deeper in the mantle wedge (Figure 1, #2) (Yoder and Tilley 1962; Stern et al. 1975; Hirose and Kawamoto 1995; Hirose 1997; Gaetani and Grove 1998; Falloon and Danyushevsky 2000). Few experimental studies are aimed at understanding the H_2O-undersaturated melts that may re-equilibrate shallower in the mantle (Figure 1, #3) (Baker et al. 1994; Pichavant et al. 2002; Hesse and Grove 2003; Parman and Grove 2004). This prompts a need for additional H_2O-undersaturated experiments at shallow mantle pressures, where basaltic magmas likely equilibrate prior to segregating from the mantle and ascending into the crust. Since there is a wide spectrum of H_2O contents in arc lavas (0-6 wt%; Wallace 2005), there may be several processes acting in the mantle that induce melting. Melts that show strong enrichments in volatiles and slab-derived trace elements may form by fluxing of slab fluids or melts, while H_2O-poor magmas may form by decompression-melting of upwelling, anhydrous asthenosphere (Figure 1, #5). Centers that are under regional extension allow for mantle-derived, primitive magmas to erupt by providing easier pathways for them to ascend through a thick crust. Primitive magmas

that span the range of H_2O concentrations may represent different melting processes and are one focus of this study.

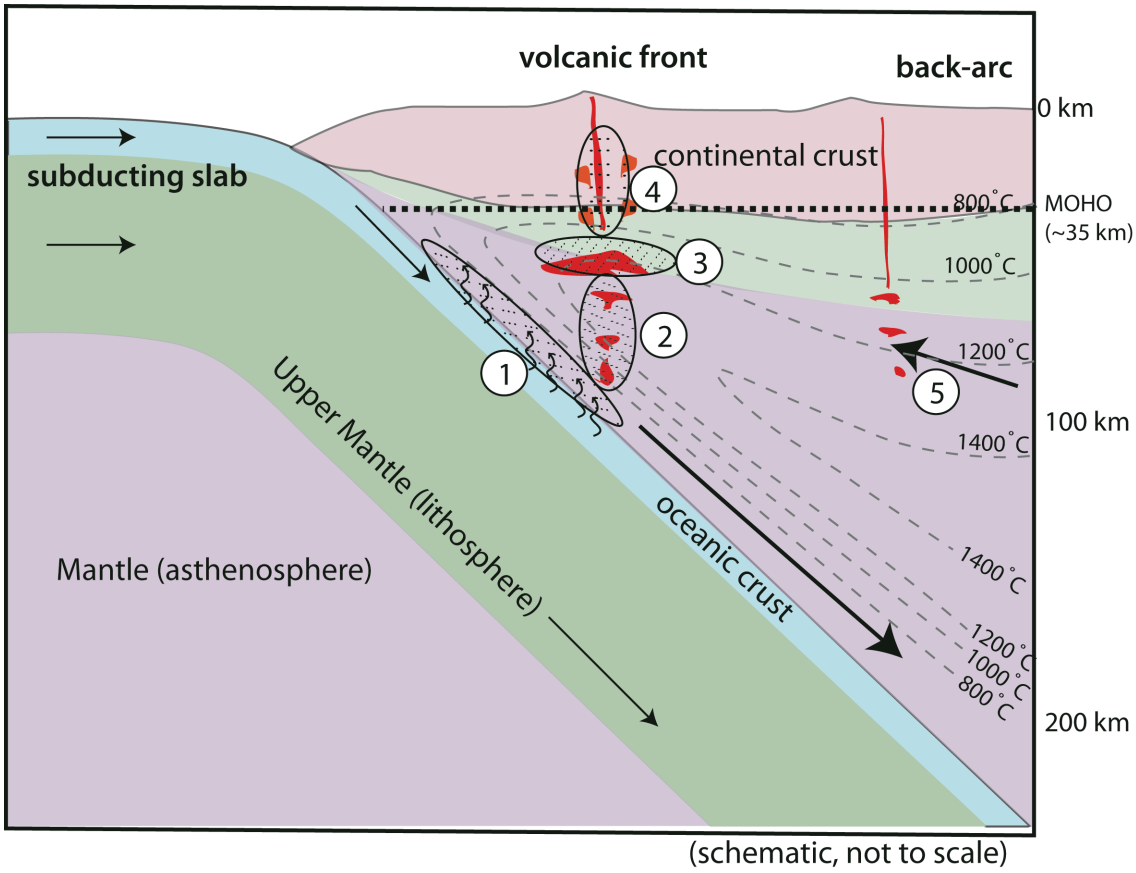

Figure 1. Schematic cross section and key processes within a continental arc. 1) Dehydrating minerals from the downgoing slab release H_2O-rich fluids into the overlying mantle wedge. Corner flow drags metasomatized mantle and fluids deeper. 2) Mantle melting begins near the H_2O-saturated mantle solidus and continues through the "nose" of the wedge. Primitive melts rise through an inverted geothermal gradient where they may become diluted in H_2O and other components. 3) Melts pond (underplate) at the base of the lithosphere or crust, and may re-equilibrate with surrounding mantle. 4) Melts may assimilate crustal material or fractionally crystallize to become more evolved silicic compositions. Alternately, primitive melts may erupt directly from the shallow mantle through dikes. 5) Upwelling asthenosphere and back-arc extension may induce anhydrous decompression mantle melting. Figure after Winter (2001), isotherms for MGVF from Johnson et al. (2009).

I focus my research on basaltic and basaltic andesite compositions that have erupted in the Trans-Mexican Volcanic Belt. This active volcanic arc contains stratovolcanoes (Popocatepetl, Colima), monogenetic mafic cinder cones (Jorullo, Paricutin), medium sized shields, and rhyolite domes and dome complexes. The cinder cones erupt predominantly basalt to basaltic andesite, generally show little to no crustal contamination, and in some cases include primitive, mantle-derived compositions. The most primitive compositions from these volcanic centers are the best surface representation of mantle processes occurring at depth in the region. This very broad continental arc also offers a window into how processes may change with depth along a subducting slab, as the volcanoes in the central TMVB overly a shallower slab than those of the western TMVB.

Geologic Setting: The Trans-Mexican Volcanic Belt

The Trans-Mexican Volcanic Belt (TMVB) is a 1000 km long east-west trending belt of mafic cinder cones, shields, and maars, intermediate stratovolcanoes, and rhyolite domes (Figure 2a). The volcanic features in the TMVB are associated with subduction of the Rivera plate (west) and the Cocos plate (central and east) beneath the North American continent. Convergence rates at the trench increase from 23 mm/yr (Rivera plate) beneath the Jalisco block to 59 mm/yr (Cocos plate) beneath the Chichinautzin Volcanic Field (CVF) (Pardo and Suarez 1995). The Rivera plate is separated from the larger Pacific Plate at the Rivera Fracture Zone and from the eastern Cocos Plate at the East Pacific Rise (EPR) (Figure 2a). The active volcanic front is subparallel to the Middle America Trench due to complex slab geometry beneath the arc; the Rivera slab steeply dips in the

west (Pardo and Suarez 1993; Yang et al. 2009) whereas the Cocos slab is shallower to flat toward the east (Manea et al. 2004; Perez-Campos et al. 2008).

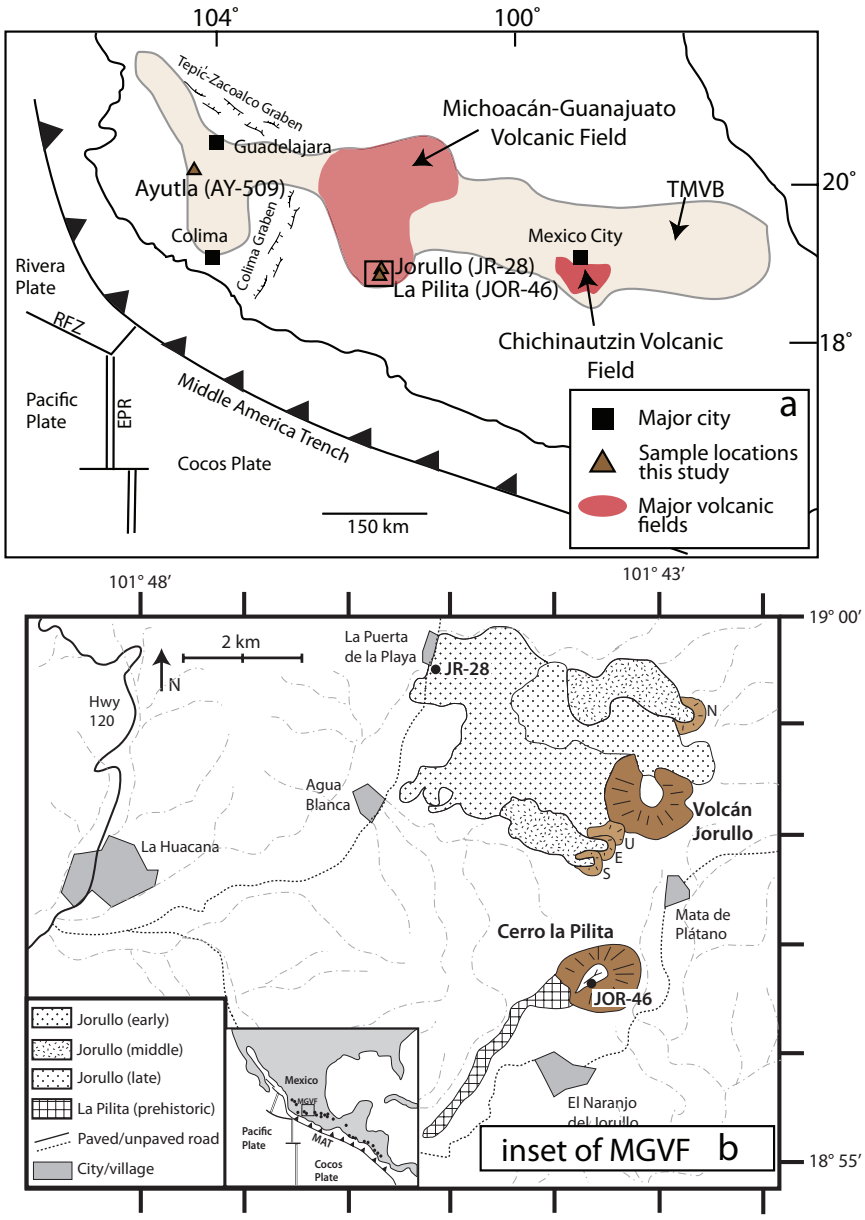

Figure 2. Location map of the Trans-Mexican Volcanic Belt (a) and the region near Jorullo Volcano, Michoacán (b). Sample AY-509 is from Ayutla Volcano, Western Mexico (Righter and Rosas-Elguera 2002), Samples JR-28 and JOR-46 are from Jorullo and La Pilita cinder cones, respectively (Luhr and Carmichael 1985). Figure b modified from Luhr and Carmichael (1985).

Since the late Miocene (~10 Ma) there has been a trenchward (generally north to south) migration of the volcanic front in response to slab steepening and slab rollback (Ferrari et al. 2001). This migration has likely subjected the sub-arc mantle wedge to enrichment by hot, upwelling asthenosphere (Luhr 1997; Ferrari et al. 2001; Ferrari 2004). Replenishment by an enriched mantle source, depletion by repeated melt extraction, and transfer of slab components have likely led to a chemically heterogeneous mantle wedge. The experimental phase relations from this work reveal these heterogeneities.

Three samples used in this study come from the Michoacán Region in the central TMVB and Ayutla in the western TMVB. The Michoacán Guanajuato Volcanic Field (MGVF) is a distinct 40,000 km^2 region characterized by ~1000 basalt to basaltic andesite cinder cones. These cinder cones (Late Pliocene to Quaternary) are monogenetic (probably <15 years eruption duration) and erupt some of the more primitive compositions found in the TMVB (Luhr and Carmichael 1985). Two of the three Mexican samples (JR-28 and JOR-46) in this study are from cinder cones in the MGVF (Figure 2b). The third Mexican sample (AY-509) comes from Ayutla, just west of the MGVF. This center lies in the Jalisco block, which is structurally defined by the Tepic-Zacoalco and Colima Grabens to the north and east, respectively. The compositions used in this study come from regions along the volcanic front. Due to their primitive geochemistry (the criteria for which are discussed next) they are the best candidates for investigating mantle melting beneath the arc. The specific geochemistry and significance of each sample is discussed further in the next section.

Scientific Goals and Approach

The goal of this work is to use experimental techniques to elucidate mantle melting processes that generate chemically distinct primitive basalts that erupt either along, or just behind the volcanic front in subduction zones. This dissertation focuses primarily on three primitive compositions from the Trans-Mexican Volcanic Belt (TMVB), but also includes experiments on a fourth primitive sample from the Aleutians. The latter allows for a comparison of magma formation processes in continental arcs (such as the TMVB) and intraoceanic arcs (Aleutians). Experimental data are used to approximate the pressures (P) and temperatures (T) over which mantle melts likely equilibrated before ascending into the crust. The lavas investigated in this work are all considered primitive, as they have geochemical characteristics that resemble mantle melts that have not been subsequently modified through crystal fractionation or assimilation of crustal materials (Table 1). The criteria commonly used to discern primitive from differentiated magmas are high MgO contents (>8 wt%), Mg# >0.65 (molar MgO/[molar MgO+FeO]), and elevated Ni (>250 ppm), and Cr (>300 ppm) contents. Melts with these characteristics indicate that they have undergone little to no differentiation by crystal fractionation. The samples in this study were chosen based on their variability in SiO_2, alkalies (Na_2O+K_2O), and magmatic volatiles (H_2O, CO_2). Since these compositions are all primitive and are presumed to have undergone little to no chemical modification upon ascent from the upper mantle, any variations among these components are interpreted as largely due to heterogeneity in source mineralogy and distribution of slab-derived components within the mantle wedge. I investigate high-pressure phase relations for four distinct primitive compositions aiming to:

1) Describe the role of mantle heterogeneity in producing primitive melts with a range of major element (SiO_2, Na_2O, K_2O), incompatible trace element, and volatile (H_2O, CO_2) concentrations.
2) Constrain the pressures and temperatures at which primitive melts equilibrated in the mantle wedge prior to rapidly ascending to the surface.
3) Compare experimentally derived P-T profiles beneath the TMVB with the results of geodynamic models that describe the thermal structure of the subduction zone.

To address these goals, I determined the near-liquidus mineralogy of each sample to seek P-T-H_2O conditions where a primitive melt is multiply saturated with mantle minerals (olivine + orthopyroxene ± clinopyroxene ± garnet/spinel) on its H_2O-undersaturated liquidus. These multiple saturation points are then interpreted to represent the average P-T conditions under which the studied primitive melts equilibrated with the indicated mantle mineral assemblages prior to their segregation from the mantle (Asimow and Longhi 2004). This method, known as the inverse approach, is described in further detail in Chapter II.

This experimental study builds on previous petrologic studies of TMVB volcanics (e.g., Luhr and Carmichael 1985; Luhr et al. 1989; Lange and Carmichael 1990; Carmichael et al. 1996; Luhr 1997; Wallace and Carmichael 1999; Johnson et al. 2009) that have used major element, trace element, and volatile analyses to infer slab-derived inputs and mantle source residues. I integrate my experimental data set with other analytical, thermodynamic, and observational data to describe the conditions under which these, and similar, primitive melts equilibrated in the mantle.

Table 1. Starting materials for high-pressure experiments

Oxide	JR-28 (Jorullo)		ID-16 (Aleutians)		JOR-46[3] (La Pilita)	AY-509[4] (Ayutla)
	1	2	1	2		
SiO_2	53.16	52.44 (0.55)	48.94	49.32 (0.99)	49.21	48.83
TiO_2	0.77	0.77 (0.02)	0.7	0.60 (0.08)	1.33	1.09
Al_2O_3	16.18	16.84 (0.25)	16.01	15.84 (0.48)	14.19	14.69
FeO	7.57	7.47[1] (0.42)	7.95	8.81[1] (0.22)	3.75	8.09[1]
Fe_2O_3			1.06		4.54	
MnO	0.13	0.13 (0.01)	0.17	0.165 (0.05)	0.12	0.128
MgO	9.43	9.40 (0.09)	11.42	11.35 (0.31)	8.32	9.84
CaO	8.41	8.43(0.42)	10.89	10.67 (0.16)	7.68	8.29
Na_2O	3.42	3.44 (0.18)	2.21	2.10 (0.09)	4.59	4.97
K_2O	0.79	0.80 (0.02)	0.52	0.51 (0.03)	2.82	1.57
P_2O_5	0.15	0.24 (0.03)	0.12	0.10 (0.04)	1.37	1.00
Total	100.00	100.00	99.99	99.46	99.11	98.5
Ni (ppm)		261[3]		266	248	230
Cr (ppm)		564[3]		662	293	370
Mg#		0.69[2]		0.70	0.66	0.69

Bulk composition of starting compositions.
[1]All Fe reported as FeO, also denoted FeO^T
[2]Mg# reported as Molar MgO/(Molar MgO+FeO^1)
[3]Values reported by Luhr and Carmichael 1985 (JR-28 is equivalent to JOR-44)
[4]Values reported by Righter and Rosas-Elguera (2001)

Organization of Dissertation

Following this introduction, the dissertation is organized into three main body chapters and a concluding synthesis chapter. The first body chapter (Chapter II: Perspectives from Experimental Petrology) provides a historical framework and literature review of high-pressure experimentation as well as detailed methodological information relevant to this study. I detail two different experimental approaches that have been used to study mantle melting processes and give the rationale for the approach used in my work. In addition, I present the advantages of, and drawbacks to each approach and

discuss their consequences when interpreting experimental data. The subsequent body chapters focus on the experimental phase relations.

Chapter III "A Comparative Study of Continental vs. Intraoceanic Arc Mantle Melting" was co-authored by Drs. Paul J. Wallace and A. Dana Johnston and published in *Earth and Planetary Science Letters*. In Chapter III I contrast experimental data for a primitive melt from Okmok Volcano, Aleutian Islands, Alaska with those from Jorullo Volcano, Central Mexico. These melts represent two endmember lavas that commonly erupt from each tectonic setting (intraoceanic arc at Okmok, continental arc at Jorullo). There are two significant findings discussed in the paper: 1) We argue that Jorullo (and similar) magmas that are H_2O-rich and have relatively high SiO_2 (basaltic andesite) are derived from hydrous partial melting of a refractory mantle source (harzburgite), and we challenge arguments that their distinctive chemical characteristics result from magma mixing or melting of non-peridotite (pyroxenite) ultramafic sources (e.g., Streck et al. 2007; Straub et al. 2008); 2) Upper mantle temperatures obtained through experiments are significantly hotter than predicted by steady-state geodynamic models for central Mexico and the Aleutians, indicating that the processes responsible for producing arc volcanoes may not be adequately predicted in such thermal models.

In Chapter IV "Experimental Constraints on the Origins of Shoshonitic and Intraplate Alkaline Basalts from the Trans-Mexican Volcanic Belt" also co-authored by Drs. Wallace and Johnston, I examine the origins of two alkaline (Na_2O+K_2O rich) basalts that differ in their K_2O and magmatic H_2O contents. These basalts are likely derived from heterogeneous mantle that has been variably enriched through

metasomatism. Trace element enrichments and elevated H_2O contents suggest that the previously enriched source was melted with the aid of fluid-fluxing.

Alkaline lavas are often associated with intraplate rifting environments or back-arc extension, and are relatively rare at the volcanic front. Though more abundant in western Mexico, and somewhat rare and volumetrically minor in the MGVF, potassic alkaline magmas have erupted at the volcanic front. The experiments from this study show the conditions under which these melts may be produced along the volcanic front and the roles of subduction fluids and enriched mantle in their genesis.

The three Mexican compositions studied in Chapters III and IV span the natural chemical diversity of primitive magmas erupted in subduction zones. Consequently, the results of these two independent studies can be integrated with other experimental and petrologic studies to provide an along-arc perspective of melt equilibration in the sub-arc mantle wedge beneath the TMVB. This synthesis, as well as an overall summary of this dissertation is presented in Chapter V.

I am the sole author of each chapter in this dissertation and performed all experimental and analytical work. Paul J. Wallace and A. Dana Johnston advised the work and provided editorial input and financial support. Chapter III has been published in *Earth and Planetary Science Letters* with Drs. Wallace and Johnston as coauthors. Chapter IV is in preparation for a special themed issue of *Contributions to Mineralogy and Petrology*, also with Drs. Wallace and Johnston as coauthors.

CHAPTER II

PERSPECTIVES FROM EXPERIMENTAL PETROLOGY

> One must begin with the simplest problems, and then proceed in an orderly way to those more complicated — first, the properties of single materials of the entire range of their stable existence; then combinations of two, in which both remain stable; then similar combinations in which exceptional phenomena occur; then simple rocks of three components, etc. — the general principle of effective progress being to meet and study the unknown phenomena *one at a time*.
> –Arthur L. Day (1906)

Introduction

Many geochemical and theoretical tools are used to understand mantle processes and the genesis of primitive magmas. Experimental petrology enables simulation of mantle pressures (P) and temperatures (T), allowing examination of potential processes that may account for the wide range of basaltic lavas observed at the surface. In this chapter I review the history of experimental work related to mantle petrology and basalt genesis to place my work in a historical context. I pay particular attention to the common difficulties encountered in conducting such experiments and give rationale for the methods chosen in this work.

Historical Overview

The establishment of the Geophysical Lab of the Carnegie Institution of Washington in 1905 set the stage for experimental investigations of equilibrium mineral-melt relationships beginning most notably with the pioneering work of Norman L. Bowen (Bowen 1914; Bowen and Anderson 1914). Early high-temperature experiments focused on simple two- or three-component systems with an aim of applying a theoretical, physical chemistry-based framework, rather than a field perspective, to physical and

chemical mineralogy (Day 1906). This departure from field-based petrology, though generally well received in rhetoric, was not applied in practice until the mid 20th century when it steadily progressed as additional labs were built worldwide (Geschwind 1995). The advancement of experimental petrology from binary and ternary to four-component systems in the late 1960s was significant; however, it is generally appreciated that natural systems contain eight or more essential chemical components so even these studies provided only rough guides to the real world.

We owe much of our understanding of partial melting of the Earth's upper mantle to early experimental work primarily on simple analog systems involving mainly CaO-MgO-Al_2O_3-SiO_2 (Presnall 1966; Kushiro 1968; Kushiro 1969b) with few using natural rocks (Yoder and Tilley 1962; Green and Ringwood 1967). These four components account for ~90% of the earth's mantle by weight, and thus were generally viewed to be sufficiently representative of the mantle. These early studies explored the partial melting behavior of synthetic peridotite as well as the crystallization trends of basaltic melts. A major motivation for these studies was to explain the origins of basaltic lavas, particularly those that are saturated or oversaturated in SiO_2, (e.g., the tholeiites or quartz tholeiites that compose the oceanic crust). Two endmember processes to derive these melts were considered: 1) they are the direct products of partial melting of mantle peridotite (i.e., they are primary or near-primary; e.g., Kushiro 1968); or 2) they are residual liquids of more primitive, parental melts that have differentiated by crystal fractionation (e.g., O'Hara 1965).

As researchers began to appreciate the impact of H_2O on magmatic processes in volcanic arcs, new experimental studies began investigating the effect of H_2O on mantle

melting, and how it might further our understanding of how basaltic and andesitic arc crust are derived (Kushiro 1969a; Wyllie 1971; Kushiro 1972; Nicholls and Ringwood 1973). Some of the liquids produced in these early hydrous experiments were elevated in SiO_2 and were taken as evidence that andesitic melts were primary, rather than residual liquids. These results have been controversial, largely due to the difficulties in interpreting modified glass compositions resulting from quenching problems and questionable approach to equilibrium due to very short experimental durations (e.g., 5-180 min). Further, more recent experiments have shown that hydrous fertile peridotite (lherzolite) melting produces compositions similar to anhydrous lherzolite (e.g., Hirose and Kawamoto 1995). However, there is experimental evidence that suggests some andesitic compositions may be products of hydrous melting of depleted mantle, or harzburgite (Tatsumi 1982; Baker et al. 1994; Parman and Grove 2004; Weaver et al. 2011; Weber et al. 2011). The origins of arc andesite are still debated (Gill 1981; Kelemen 1995; Grove et al. 2002; Streck et al. 2007; Straub et al. 2008) and potential mechanisms for their origins can be tested with additional experimental studies.

My work furthers progress toward understanding processes that generate a range of primitive basaltic and basaltic andesite liquids in subduction zones. I provide observations and interpretations from nearly 150 new high-pressure hydrous experiments using natural volcanic materials at P-T conditions appropriate for the upper mantle in many subduction zones. This data set is significant, given the relatively short history of experimental petrology in general, and the even shorter history of well-controlled experiments that utilize natural hydrous melts. Complete experimental data sets that cover a wide range of P-T-H_2O conditions are necessary for refining and calibrating

geochemical (e.g., Ghiorso et al. 2002; Lee et al. 2009) and geophysical (e.g., Cagnioncle et al. 2007; van Keken et al. 2008) models that depend on such parameters. Moreover, experiments are a direct way to test hypotheses about the compositional heterogeneity in the mantle, otherwise inferred only from geochemical tracers.

Experimental Design

The design of an experimental study may vary depending on the motivating questions. There are two primary approaches an investigator might take to probe questions pertaining to mantle melting: a forward or an inverse approach. I highlight the advantages and shortcomings of each method and provide the rationale for my using the inverse approach in this research.

Forward Experiments

The seemingly most logical way to explore the geochemical range of melts that may be produced by melting the mantle is to partially melt mantle peridotite directly; this is the so-called forward approach. The temperatures and pressures of melting can be observed and the stoichiometry of the melting reaction can be constrained by observing how the relative proportions and chemical compositions of melts and coexisting residual minerals change with increasing melt fraction, *F*. These experiments most closely simulate the onset of melting deep in the mantle wedge (See Chapter I, Figure 1).

Forward experiments utilize either synthetic, reagent grade oxides or natural mineral separates to create starting bulk compositions representative of mantle peridotite. The mantle solid is then partially melted, resulting in an experimental run product that consists mostly of residual, crystalline, starting material and small amounts of melt (usually F=0.01-0.2, or 1-20%). This approach is useful for determining the

compositional range of melts that may be in equilibrium with a mantle residuum at any P, T, H_2O content, or *F*. It is also useful in determining the likely reactions by which melting occurs. For example, a classic study by Baker and Stolper (1994) determined the following melting reaction as fertile peridotite (lherzolite: 50% olivine [ol] + 30% orthopyroxene [opx] + 17% clinopyroxene [cpx] + 3% spinel [sp]) melts:

$$0.35\ \text{opx} + 0.71\ \text{cpx} + 0.13\ \text{sp} = 0.22\ \text{oliv} + 1\ \text{melt}$$

The reaction coefficients express the rates at which the modal proportions of each phase change as melting proceeds (dX/dF, where X is the modal fraction of solid and F is the melt fraction). In this example, although the starting composition consisted of only 17% cpx, cpx contributes to the melt at a very high rate (dX/dF=0.71). There are two significant consequences of this reaction: 1) as melting of fertile mantle proceeds, cpx is the first phase to be consumed, indicating that low modal abundance of cpx in residual mantle (harzburgite: ol+opx) may be indicative of mantle depletion by prior melting; and 2) additional olivine forms as melting proceeds since the reaction is peritectic in nature. This second point may seem somewhat counterintuitive, but it is not uncommon for solid phases and melt to both be products of a melting reaction. The mineralogy of the mantle residue, with respect to mode and mineral chemistry, will become significant for experiments that use the inverse approach.

Despite the obvious advantages, there are drawbacks to the forward method. One disadvantage is the extreme difficulty of analyzing very small degree melt pockets (F<0.10) within a predominantly crystalline matrix. Several techniques have been developed to trap small degree melts for easier analysis with modern analytical tools (electron probe microanalysis, EPMA). In one technique, a layer of diamond aggregate is

added between or above the peridotite layers in the experimental capsule (Hirose and Kushiro 1993; Baker and Stolper 1994). This diamond layer creates a pressure gradient that draws the melt away from residual crystals towards the interstitial space between diamond grains as melting occurs. The diamond layer is effective at creating segregated melt pools, but is difficult to polish to a smooth and flat surface for EPMA. A modification of this technique avoids the polishing problem by utilizing vitreous carbon spheres instead of diamond to create a porous melt trap (e.g., Schwab and Johnston 2001). While both techniques are appropriate for some systems, the use of vitreous carbon-based traps results in experiments at reducing conditions that may be inappropriate for hydrous, more oxidized systems such as subduction zones.

The complications of trapping and analyzing low degree melts become significant when we observe how dramatically melt compositions change during incipient melting of peridotite, as *F* increases from 0-0.05 (0-5%). Figure 3 shows the average SiO_2, K_2O, Na_2O, and CaO compositions of anhydrous, partial melts produced using such forward approach experiments (Baker and Stolper 1994; Baker et al. 1995; Hirschmann et al. 1998; Pickering-Witter and Johnston 2000; Schwab and Johnston 2001). These experiments were conducted with the goal of assessing the range of melts that may be produced by variable mantle peridotite sources (fertile to intermediate). Figure 3 shows that incompatible (with respect to solid phases) elements such as K strongly partition into the melt initially (evidenced by the spike in K_2O at low *F*), and become diluted as melting proceeds. The strong SiO_2 enrichment at low melt fractions is postulated to be due to the modification of silicate networks by alkalies at moderate to low pressures (Hirschmann et al. 1998), while the sharp increase in CaO with increasing *F* is due to the

preferential melting of calcium-rich clinopyroxene, until the point when it is exhausted. It is apparent that anhydrous mantle melting produces a wide array of melts, with significant chemical changes occurring over just a few percent melting. It is important to note that Figure 3 shows melt compositions produced from anhydrous peridotite, and does not include the range of melts that may be produced with the addition of slab-derived, hydrous and/or silica rich fluids and melts.

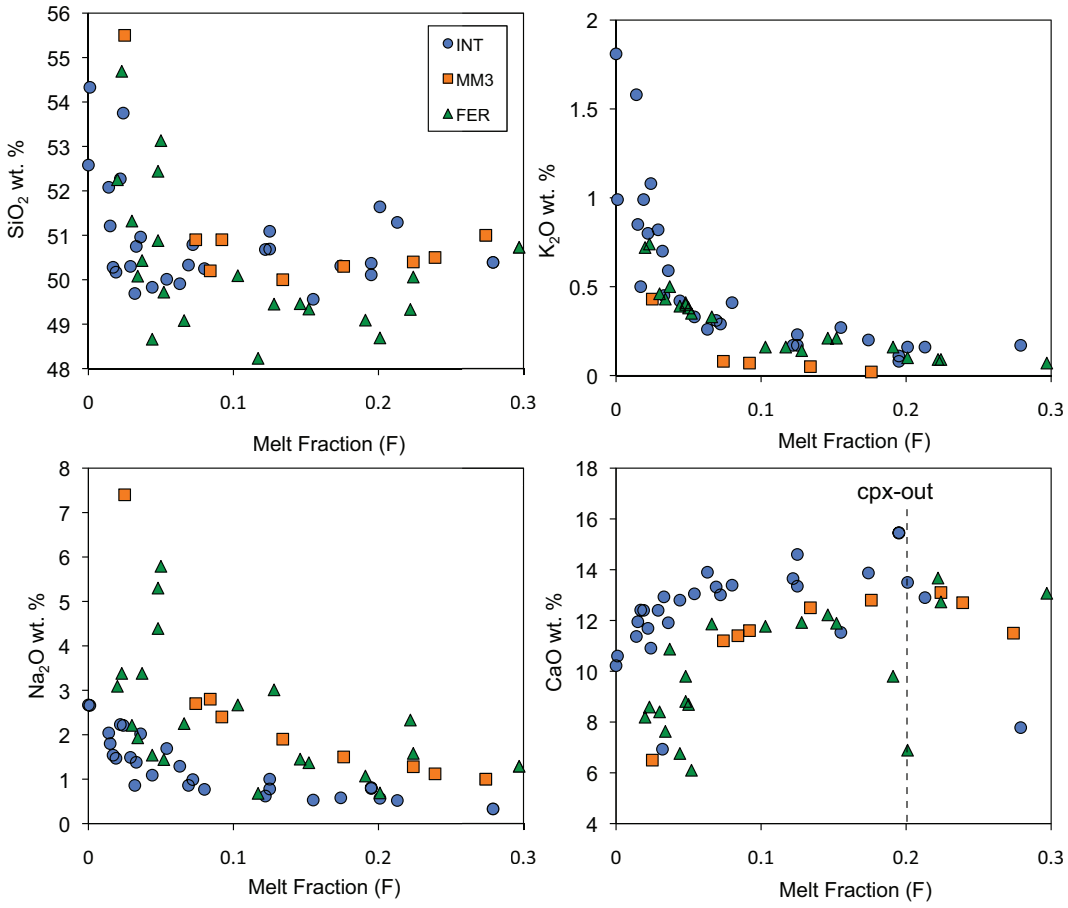

Figure 3. Average oxide components of anhydrous partial melts from fertile and intermediate peridotite vs. melt fraction *F*. MM3 glass data from Baker and Stolper (1994), Baker et al. (1995), and Hirschmann et al. (1998). FER are variably fertile lherzolite of Pickering-Witter and Johnston (2000) and INT are intermediate lherzolite from Schwab and Johnston (2001).

Despite the drawbacks, forward experiments are appropriate for assessing the range of basaltic melts that may be produced by, or in equilibrium with, a given mantle residue. However, because a broad spectrum of melts is produced by melting variable residues under a range of P-T conditions, this method may not be the best choice when the goal is to constrain the source residuum of a particular natural basaltic melt. Under these circumstances, the starting mantle composition is not known *a priori.* An investigator would need to melt an unknown, hypothetical starting peridotite under a variety of conditions (P, T, H_2O, F) to observe if the partial melt resembles the natural melt of interest. This procedure would likely be exceedingly labor-intensive, so a different method is warranted.

Inverse Experiments

So-called inverse approach experiments are most appropriate when the scientific question revolves around constraining the mantle residue of a particular natural basaltic melt that has erupted at the surface as lava or tephra. In inverse experiments, the basalt (melt) of interest is the starting composition, and potential mantle residues are explored under a range of P-T ± H_2O conditions. I use this approach in my work to constrain potential source mineralogies for several chemically distinct basaltic melts. The inverse approach presumes that the basaltic melt of interest is, in fact, a mantle-derived, or primitive melt. Primitive melts have geochemical characteristics (e.g., Mg# ~0.70–0.72, Ni ~250 ppm, Cr~500 ppm) indicating they were last in equilibrium with a mantle residue, and have undergone little to no chemical modification since segregating from the mantle and erupting. If this presumption is true, then the melt should be saturated in mantle minerals on its liquidus at the P-T-H_2O conditions of last equilibration. This

concept is illustrated in the hypothetical experimental P-T phase diagram in Figure 4. Here, a supposed melt (± H_2O) is partially crystallized over a range of temperatures and pressures. The liquidus temperature is constrained and stabilities of crystallizing minerals are mapped in P-T space.

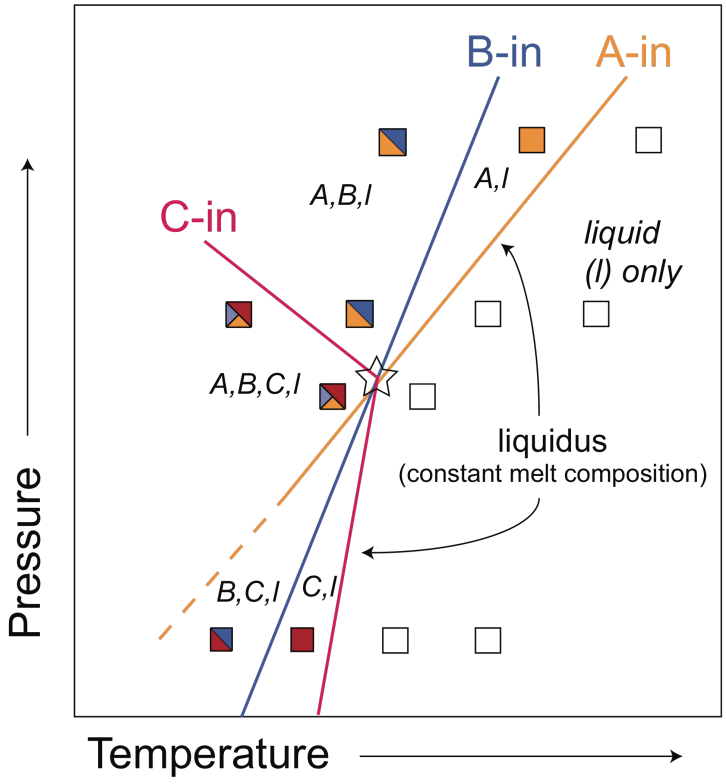

Figure 4. Schematic near-liquidus P-T phase diagram. Each box represents one experiment at constant P and T. Open boxes indicate superliquidus conditions and consist of liquid (*l*) only. Filled boxes indicate the presence of a crystalline phase A, B, or C, in addition to melt. Solid lines are drawn where phase stability boundaries are constrained by experiments, dashed where phase relations are uncertain. The liquidus line represents the appearance of the first crystals and is a line of constant melt composition. The liquids at subliquidus temperatures differ significantly from the starting melt due to partial crystallization. The open star denotes the multiple saturation point, where, in this example, a melt with the composition of the starting material would be simultaneously saturated in crystalline phases A+B+C, indicating that the melt may have last equilibrated with a residue consisting of these phases with their measured compositions.

For inverse experiments, only the near-liquidus mineralogy is significant because, as crystallization proceeds with decreasing temperature, the melt composition changes sufficiently that it no longer resembles the starting bulk composition. Small degrees of crystallization (near-liquidus) do not change the melt composition significantly, so along the liquidus I can consider the melt composition to be a constant, the starting suspected primary melt composition I have chosen to work with. The P-T conditions at which the melt is in equilibrium with two or more minerals on its liquidus is described as a *multiple saturation point*. The multiple saturation point is interpreted as the average of the range in P-T conditions over which the primitive melt last equilibrated while ascending and continually reequilibrating with the mantle material it traverses. The mineralogy at such a point reveals the permissible phases (and their compositions) within the mantle residue from which the melt segregated at those P-T conditions.

There are two primary caveats to inverse experiments. First, the multiple saturation points are only representative of the site of *last* equilibration and will not be representative of the original source composition or pressure at which melting initiated. Recall from Chapter I that melts are generated in the deep portion of the wedge, then likely reequilibrate while traversing the shallower mantle before erupting. Forward experiments explore the former process while inverse experiments reveal the latter. Second, the inverse approach may not crystallize a phase if that phase is involved in a peritectic reaction with the silicate melt. A relevant example is the reaction between olivine (ol) and silicate melt to produce orthopyroxene (opx):

$$Mg_2SiO_4 \text{ (ol)} + SiO_2 \text{ (liquid)} \Leftrightarrow Mg_2Si_2O_6 \text{ (opx)}.$$

A melt saturated in olivine will not crystallize olivine as its liquidus phase if it is involved in this reaction. In this example, the absence of liquidus olivine may indicate that either 1) the melt is not saturated with olivine, or 2) the melt is saturated, but that it was dissolving and reacting to produce orthopyroxene when the melt was segregated. Similar reactions occur with other potential mantle phases (such as garnet, orthopyroxene, and biotite) and must be considered when interpreting near liquidus mineralogy.

Common Experimental Difficulties

The ultimate goal of most experimental studies is to reproduce natural conditions or simulate natural processes while maintaining equilibrium among all of the phases present in the system. These phases may include a hydrous or anhydrous quenched melt (glass), crystals of one or more minerals, and possibly a vapor phase (bubbles). This is a non-trivial challenge when investigating multi-component systems such as natural volcanic melts. It is further complicated by potential unwanted chemical interaction between materials under investigation and the experimental assembly itself. High-pressure experiments have proven difficult in the past, particularly when the compositions of interest are Fe-bearing and/or hydrous. Noble metal capsules (Au, Pt, Ag) capsules have been successfully used in high-pressure melting experiments, but present two main problems: Fe tends to alloy with, and H_2 diffuses through, these metals to differing degrees. These issues are commonly referred to as the "iron-loss" and "hydrogen- or water-loss" problems. Au has been successfully used in Fe and H_2O-bearing systems, but its low melting point precludes its use at the higher temperatures required for experimentation with basalts. Alloys of Au and Pd enable higher temperature

experiments than pure Au, but are also more susceptible to alloying with Fe in the melt through exchange with the capsule:

$$FeO\ (melt) \Leftrightarrow Fe^0\ (alloy) + \tfrac{1}{2}\ O_2$$

Iron loss to the capsule material changes the bulk composition of the sample and affects the compositions of both the melt and the crystallizing minerals. Consequently, the resulting experimental charge will bear little resemblance to the initial starting composition.

If the starting composition is hydrous, hydrogen may diffuse through the capsule walls after dissociation of H_2O by the reaction:

$$H_2O \Leftrightarrow H_2 + \tfrac{1}{2}\ O_2$$

The O_2 generated may then be consumed in an oxidation reaction with FeO in the melt becoming Fe_2O_3 (melt). If the starting materials are oxidized to start with, both Fe- and H_2O-losses are minimized (Kawamoto and Hirose 1994; Hall et al. 2004). The samples in this study range from somewhat oxidized (Fe^{2+}/Fe^{Total} ~0.6) to reducing (Fe^{2+}/Fe^{Total} ~0.8) and are susceptible to H_2 and Fe exchange during high-pressure experiments.

In this study, I use gold-palladium ($Au_{75}Pd_{25}$) alloy capsules, which, while better with respect to Fe-loss than pure Pt, are still susceptible to Fe-loss, requiring extra procedures to mitigate the problem. Here I address the Fe-loss problem by presaturating the $Au_{75}Pd_{25}$ capsules with Fe prior to using them in our high-pressure experiments (Gaetani and Grove 1998). This technique is discussed in detail in Chapters III and IV, however I address the consequences of Fe-loss further in the next section of this chapter ("Oxygen Fugacity"). The remainder of the experimental furnace assembly consists of

inner, crushable MgO spacers, a graphite heater, and an outer sleeve of pressed and sintered fluorite (CaF_2). The assembly is capped with a stainless steel plug through which the thermocouple passes, which, in turn, is electrically insulated from the WC pressure vessel with a precision ground Pyrex collar (Figure 5).

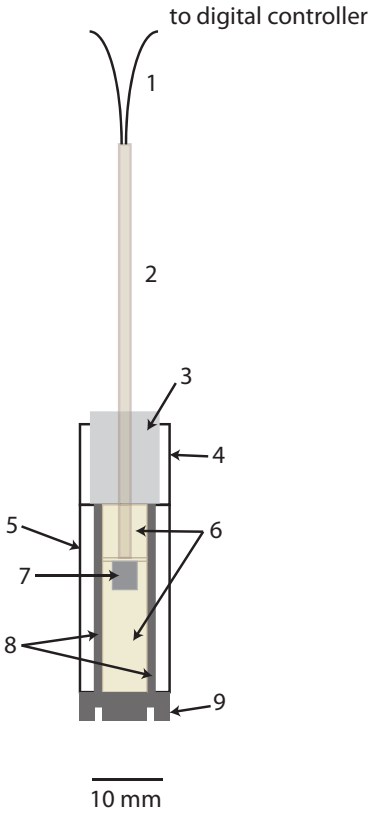

Figure 5. Scale drawing of experimental furnace assembly. 1: thermocouple wires connected to digital controller, 2: four-bore alumina thermocouple tube, 3: steel base plug, 4: outer Pyrex glass sleeve, 5: pressed and sintered fluorite (CaF_2) sleeve, 6: crushable inner MgO spacers (bushing, wafer, pedestal), 7: rock powder ± H_2O inside sealed, preconditioned AuPd capsule, 8: graphite heater, 9: graphite spacers.

Oxygen Fugacity

One problem inherent to H_2O-undersaturated experiments is the inability to directly control the redox state of the experiment using a solid-solid oxygen fugacity buffer. The interplay between (fO_2), Fe-exchange, and H_2O loss can have significant consequences if not considered in an experimental design. Since the goal of my inverse experiments is to investigate saturation with mantle minerals, particular attention must be

paid to the compositions of ferromagnesian phases because of their sensitivity to redox reactions. The prevailing fO_2 of the system defines the redox state of the system, and therefore the Mg/Fe^{2+} ratios of solid solution minerals such as olivine and orthopyroxene—changes in mineral assemblages due to changing oxygen fugacity (fO_2) are often a result of the oxidation state of iron. Typical mantle olivine would have an Mg# [molar Mg/(molar $Mg+Fe^{2+}$)] ranging from 0.88-0.92 (denoted Fo_{88-92}), depending on the peridotite source. Without some attempt to mimic the system's natural fO_2, Fe may readily exchange with the capsule, Fe^{2+} may oxidize to Fe^{3+}, and equilibrium crystals may not resemble mantle phases, becoming much more magnesian than they otherwise would be. Though fO_2 is not explicitly controlled in my experiments, it may be influenced by using capsules that are preconditioned with Fe. As described in greater detail in Chapters III and IV, this presaturation technique enables experimentation over a range of fO_2 commonly accepted as prevailing in subduction zones (e.g., Wood et al. 1990); however, deviations from the true redox state (and therefore, equilibrium state) of the natural system may affect the compositions of crystallizing phases.

I demonstrate this effect using the thermodynamic modeling program pMELTS (Ghiorso et al. 2002). Figure 6 illustrates the effect of fO_2 on the composition of crystallizing olivine and the co-saturation P-T conditions of olivine + clinopyroxene for one of the basaltic melts (JOR-46) used in Chapter IV. Using this basalt as the starting composition, I numerically crystallized the melt at constant pressure and fixed fO_2 and repeated the procedure over a range of these variables. The fO_2 was fixed relative to the Quartz-Magnetite-Fayalite (QFM) equilibrium curve (Myers and Eugster 1983), where fayalite reacts with oxygen to form magnetite and quartz according to the reaction:

3 Fe_2SiO_4(fayalite) + O_2 ⇔ 2 Fe_3O_4(magnetite) + 3 SiO_2(quartz).

For this reaction, an equilibrium constant *K* can be calculated:

$$K = \frac{(a_{mt}^2)(a_{qtz}^3)}{(a_{fa}^3)(f_{O_2})} = \exp\left(\frac{-\Delta G^\circ}{RT}\right)$$

where *a* is the activity of magnetite(mt), quartz(qtz), fayalite(fa), and f_{O2} is the fugacity of oxygen(O_2). If the activities of solid phases and $\Delta G^\circ_{reaction}$ are known, then at equilibrium fO_2 can be calculated as a function of T by

$$\ln f_{O_2} = \frac{\Delta G^\circ_{reaction}}{RT}.$$

Crystallization simulations were conducted at from one log unit more reducing (QFM-1) to 2 log units more oxidizing (QFM+2) than this reaction at any given T. I mapped the crystallizing phases for each simulation to locate the P and T at which olivine transitions to clinopyroxene on the liquidus and recorded the composition of the liquidus olivine. This thermodynamically-based simulation provides a direct comparison to the observed experimental phase relations (Chapter IV) and liquidus olivine compositions. Figure 6 indicates the starting liquid is in equilibrium with mantle olivine (Fo_{90}) at QFM+2 whereas under conditions one log unit more reducing (QFM+1), the equilibrium olivine shifts in composition to Fo_{88}. More generally, as the prevailing fO_2 becomes more reducing, the $Fe^{2+}/(Mg+Fe^{2+})$ ratio of the liquidus olivine increases (Fo content decreases), highlighting the importance of reproducing accurately the appropriate fO_2 in the experiments. We also see in Figure 6 that fO_2 also influences the P-T position of the liquidus, although the apparent shifts resulting from a one log unit fO_2 variation would be relatively minor (~0.05 GPa, 15 °C), and perhaps undetectable given the resolution of piston cylinder experiments. As will be discussed in subsequent chapters, the fO_2 range

for a set of experiments may vary by 1–2 log units. Therefore, it is expected that the crystallizing olivine will show a range of Fo contents. I take these factors into consideration when arguing the potential for a primitive melt to be in equilibrium with a mantle assemblage.

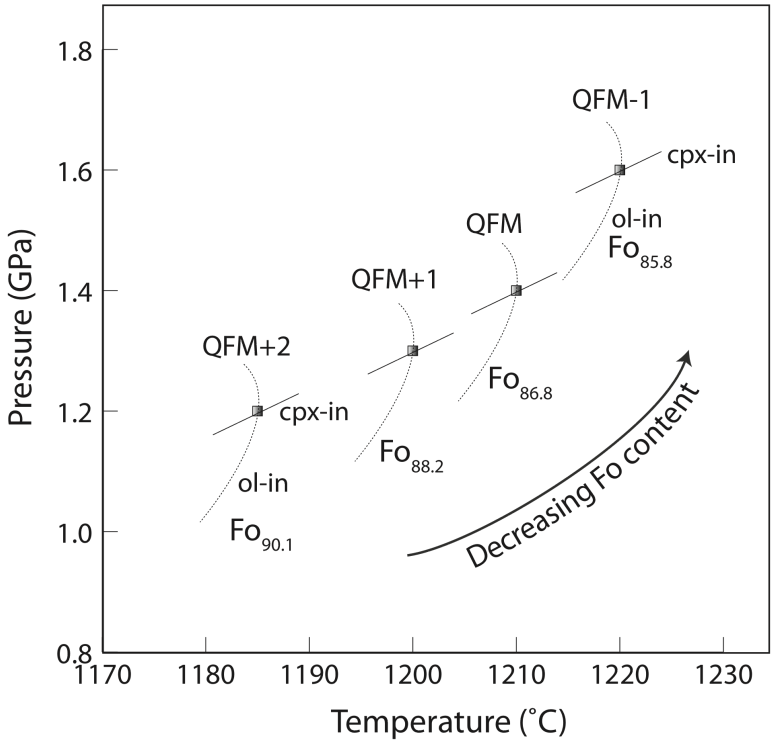

Figure 6. Effect of fO_2 on equilibrium olivine compositions. Olivine (ol) and clinopyroxene (cpx) saturation is plotted in P-T space as a function of varying fO_2 as modeled using pMELTS.

Bridge

In this chapter I described the motivation and rationale for choosing the experimental methods used in this research. In the next chapter I apply these experimental techniques to primitive basalts from Central Mexico and the Aleutian Islands, Alaska. These compositions represent common endmember lavas that erupt in continental (Mexico) and intraoceanic island (Aleutians) volcanic arcs. The experimental,

near-liquidus phase relations under H_2O-undersaturated conditions are used to infer the P-T-H_2O conditions of mantle equilibration, and explore the differences in mantle sources for lavas from each tectonic setting

CHAPTER III

A COMPARATIVE STUDY OF CONTINENTAL VS. INTRAOCEANIC ARC MANTLE MELTING: EXPERIMENTALLY DETERMINED PHASE RELATIONS OF HYDROUS, PRIMITIVE MELTS

This chapter was published in *Earth and Planetary Science Letters*, Volume 308, in August 2011 and is co-authored by Drs. Paul Wallace and Dana Johnston. I was the primary author of this manuscript, completed all laboratory experiments, and performed data analyses. Both co-authors contributed editorial and financial support for this work.

3.1. Introduction

It is well established that H_2O from the subducted oceanic plate plays a crucial role in basaltic magma genesis within the mantle wedge beneath arcs. Experimental studies have shown that the introduction of a slab-derived hydrous fluid or melt to the mantle wedge significantly lowers the peridotite solidus. One possible model is that rising fluids initiate melting at the vapor-saturated solidus in the deep part of the wedge, and as the hydrous melt continues rising through the inverted thermal gradient, the higher temperatures cause further melting of peridotite and dilution of the initial H_2O content of the melt (e.g., Grove et al., 2006). The details of this process are poorly understood, however, and there are still few high-pressure experiments that investigate the H_2O - undersaturated equilibration conditions of hydrous primitive arc melts (Hesse and Grove, 2003; Medard and Grove, 2008; Muntener and Ulmer, 2006; Parman and Grove, 2004; Pichavant and Macdonald, 2007; Ulmer, 2007).

Furthermore, the origins of primitive melts that are elevated in SiO_2 relative to MgO (high-Mg andesites and boninites) are uncertain. The extent to which slab-derived fluids or melts, source depletion, and melt reaction in the subarc mantle contribute to their generation has been debated (Kelemen et al., 2003b; Parman and Grove, 2004; Wood and Turner, 2009), and in some cases their mantle origin has been questioned (Streck et al., 2007). An additional question is whether refractory sources beneath arcs (harzburgite) form by large degrees of melting due to fluxing of fluids from the subducted plate (e.g., Grove et al., 2002) or from reactions between ascending basaltic melt and mantle lherzolite in which clinopyroxene is dissolved and orthopyroxene is precipitated (e.g., Kelemen et al., 1992).

Here we present new results from H_2O-understaturated piston-cylinder rock melting experiments on two primitive but chemically distinct arc magma compositions: a basaltic andesite from Central Mexico (SiO_2=53.2 wt%) and a basalt from the Central Aleutians (SiO_2=48.9 wt%). The geochemistry of these samples (e.g., Mg#, MgO and Ni contents) suggests they are both mantle-derived. The goal of this work is to constrain the P-T-H_2O conditions of mantle melt segregation and describe the mantle mineralogy with which these melt compositions last equilibrated. We present our data with those of other rock-melting experiments to constrain the range of primitive melt compositions produced by melting various mantle lithologies, from fertile lherzolite to refractory harzburgite. Our experimental results support the interpretation that fluid-fluxed melting of, or shallow reequilibration with, harzburgite can produce SiO_2-rich primitive melts (e.g., Grove et al., 2003).

The experiments reported here are also useful for testing hydrous olivine-melt thermometers (Medard et al., 2008; Sugawara, 2000) and petrologic models that constrain the pressures (P) and temperatures (T) of mantle-melt equilibration (Katz et al., 2003; Lee et al., 2009; Medard and Grove, 2008; Sugawara, 2000; Wood and Turner, 2009). In addition, we can compare our experimental P-T estimates with geodynamic models of arcs that provide P-T profiles through the mantle wedge (Manea et al., 2004; Peacock and Wang, 1999; Peacock, 1991; Syracuse et al., 2010; van Keken, 2003; van Keken et al., 2002). A complete experimental data set that explores the P-T conditions of melt generation and subsequent melt extraction is also important for development of geodynamic models that couple mantle and melt flow (e.g., Cagnioncle et al., 2007). This investigation adds to this data set by constraining the P-T-H_2O conditions of near-primary melt extraction from two contrasting subduction zones, the continental arc of Central Mexico and the intraoceanic island arc of the Central Aleutians.

3.2. Geologic Setting and Starting Materials

This work focuses on two primitive compositions: a basaltic andesite from central Mexico and a basalt from the central Aleutian volcanic arc (Table 2). JR-28, collected and provided by Dr. J. Roberge (UNAM), is a basaltic andesite (similar in composition to JOR-44 of Luhr and Carmichael, 1985) from the earliest lava flows of Volcán Jorullo, a monogenetic cinder cone in the Michoacán-Guanajuato Volcanic Field (MGVF) of the Trans-Mexican Volcanic Belt (TMVB). The TMVB is an east-west trending belt of volcanic features resulting from the subduction of the Cocos and Rivera plates beneath the North American plate. Volcanism along this arc has produced rock compositions that range from primitive basalt and basaltic andesite to rhyolite (Hasenaka and Carmichael,

1985; Luhr et al., 1989). The MGVF contains abundant cinder cones of basalt and basaltic andesite (Hasenaka and Carmichael, 1985, 1987). JR-28 contains olivine phenocrysts (~5 vol%) with Cr-spinel inclusions and a groundmass of plagioclase, augite, olivine, spinel and glass (Luhr and Carmichael, 1985). It is among the most primitive and hydrous of the magmas erupted within this arc (Luhr, 1997). Olivine-hosted melt inclusions from early erupted tephra at Jorullo (olivine phenocrysts up to Fo_{91}) have H_2O contents as high as 5.7 wt%, providing a minimum value for the H_2O content of the primitive melt (Johnson et al., 2008). Accordingly, the majority of the experiments with this sample were run with 5 and 7 wt% added H_2O.

The second sample, ID-16, is a primitive basalt erupted at Okmok Volcano in the Central Aleutian arc. This shield volcano is located between the Four Mountains and Cold Bay arc segments, where the Pacific plate transitions from subducting beneath the oceanic part of the North American plate in the west to subducting beneath the continental Alaskan Peninsula in the east (Kay et al., 1982). Quaternary basaltic lavas comprise the early-formed part of the volcano (Byers, 1959). Nye and Reid (1986) collected and analyzed the least fractionated basalts from Okmok, including ID-16, which Dr. C. Nye kindly provided to ADJ. ID-16 has olivine phenocrysts (Fo_{88-89} cores) in a groundmass of olivine, plagioclase, clinopyroxene, and glass. This sample is characteristic of a near-primary mantle melt. Draper and Johnston (1992) investigated the anhydrous phase relations of ID-16, though by comparison with other arc magmas, it is likely that it contained some dissolved H_2O. We note that there have been two previous attempts to determine the hydrous phase relations for ID-16, Dewey (1996) and Weaver (2007), but the former suffered from uncertainties in the experimental H_2O contents and

the latter suffered from unacceptable Fe loss to the Au-Pd capsules. Reliable hydrous phase relations for this sample are needed to provide more accurate P-T estimates of melt equilibration than have been suggested in previous work (Draper and Johnston, 1992; Nye and Reid, 1986). Although we do not have melt inclusion data to estimate the pre-eruptive H_2O content for ID-16 melts, we chose to investigate its near liquidus phase relations with 2 and 5 wt% H_2O based on the range of water contents of mafic arc magmas (Wallace, 2005). The primitive nature of JR-28 and ID-16 makes these lavas appropriate starting compositions for investigating mantle-melting conditions beneath the MGVF and Central Aleutian arcs.

Table 2. Bulk composition of starting materials. JR-28. Analysis 1 provided by J. Roberge (unpublished data), analysis 2: average glass composition of all superliquidus experiments (n=14) normalized to 100% anhydrous. ID-16 analysis 1: XRF analysis from Nye and Reid (1992). FeO calculated by assuming Fe3+/Fe2+=0.12. Analysis 2: Average of 9 microprobe analyses of glass of superliquidus run product reported by Johnston and Draper (1992). Parentheses indicate 1σ standard deviation where available

Oxide	JR-28		ID-16	
	1	2	1	2
SiO_2	53.16	52.44 (0.55)	48.94	49.32 (0.99)
TiO_2	0.77	0.77 (0.02)	0.7	0.60 (0.08)
Al_2O_3	16.18	16.84 (0.25)	16.01	15.84 (0.48)
FeO	7.57	7.47[1] (0.42)	7.95	8.811 (0.22)
Fe_2O_3			1.06	
MnO	0.13	0.13 (0.01)	0.17	0.165 (0.05)
MgO	9.43	9.40 (0.09)	11.42	11.35 (0.31)
CaO	8.41	8.43(0.42)	10.89	10.67 (0.16)
Na_2O	3.42	3.44 (0.18)	2.21	2.10 (0.09)
K_2O	0.79	0.80 (0.02)	0.52	0.51 (0.03)
P_2O_5	0.15	0.24 (0.03)	0.12	0.10 (0.04)
Total	100.00	100.00	99.99	99.46
Ni (ppm)		261[3]		266
Cr (ppm)		564[3]		662
Mg#[2]		0.70		0.70

[1]Total Fe calculated as FeO
[2]molar MgO/(MgO+FeO[1])
[3]Luhr and Carmichael (1985)

3.3. Methods

3.3.1. Inverse Approach

We employed inverse approach experiments to constrain the P-T-H_2O conditions under which these primitive melts could have been in equilibrium with a mantle residue. The approach presumes that these primitive compositions represent liquids that have undergone essentially no chemical modification since last equilibrating within the mantle before erupting. If this is the case, then our starting compositions should be multiply saturated with mantle minerals on their liquidii at the P-T-H_2O conditions of last equilibration within the mantle. Thus, by performing experiments that bracket the H_2O-undersaturated liquidus surfaces of our samples, we can map the liquidus mineralogy onto these surfaces and seek conditions of multiple saturation in two or three phases, which we can then interpret as permissive conditions under which our samples could have been in equilibrium with these phase assemblages. It is important to note that the observed multiple saturation points would represent real pressures of final equilibration and melt segregation only if the melts had sufficient time to thoroughly reequilibrate at some final depth in the mantle before rapidly ascending to the surface in dikes (Asimow and Longhi, 2004). If not, the experimentally determined multiple saturation points would instead record a signal of polybaric reequilibration and reveal the average pressure over which the melts reequilibrated (Asimow and Longhi, 2004).

3.3.2. Experimental Techniques

We used $Au_{75}Pd_{25}$ alloy capsules that were preconditioned with Fe in a 1 atm Deltec gas-mixing (CO_2-H_2) furnace in order to minimize Fe-loss from the sample to the capsule (e.g., Medard and Grove, 2008). Analysis of the post-experimental run products

demonstrated that the preconditioning process maintains the starting FeO contents to within ±10% relative, with some products apparently losing a little, and others apparently gaining a little from the capsule alloy (Appendix A).

For the phase equilibrium runs, we used the 1/2-inch endloaded piston-cylinder apparatuses at the University of Oregon. The preconditioned (Fe)-Au-Pd capsules were packed with finely ground natural rock powder and the desired amount of distilled H_2O was added using a microsyringe. Capsules were crimped, suspended in a cold water bath, and welded shut using a carbon arc welder. Each capsule was weighed before and after welding to evaluate whether H_2O was lost during the loading or welding process. The sealed capsules were positioned in the "hot spot" (target T±10°C) of a graphite/MgO/CaF_2 furnace assembly (Pickering et al., 1998). Temperature was measured using W-Re_5/W-Re_{26} thermocouples and monitored using a Eurotherm digital controller with an Omega cold-junction compensator. Reported pressures are nominal with no friction correction. Samples were held at constant P and T for 10–24 hours and rapidly quenched by cutting power to the furnace. Previous results from our lab (Mercer and Johnston, 2007) demonstrated that such durations are long enough to achieve an acceptable approach to equilibrium in these melt-rich near-liquidus experiments but short enough to minimize H_2O loss.

3.3.3. Analytical Techniques

After each experiment, the recovered capsules were sectioned, mounted in epoxy, and polished for microanalysis. Sample textures were evaluated using a FEI Quanta Scanning Electron Microscope (SEM) and analyzed for major and minor element composition using a Cameca SX100 electron microprobe at the University of Oregon.

The following analytical conditions were used for microprobe analyses: crystalline phases, 15 kV accelerating voltage, 30 nA beam current and <1 μm beam diameter; hydrous glasses, 15 kV accelerating voltage, 10 nA beam current and a 10-30 μm beam diameter. To correct for Na migration in the glasses during analysis, the count rate for Na was measured as a function of time and then extrapolated back to time zero.

Glass H_2O contents estimated using the water-by-difference method (Roman et al., 2006) typically exceeded the quantities added by microsyringe, reflecting systematically slightly low totals on our glass microprobe analyses. However, analyses by reflection Fourier Transform Infrared (FTIR) spectroscopy suggest that the experimental H_2O contents match the microsyringe quantities to better than 1.5 wt.% absolute. Any mismatches between the nominal H_2O contents and the reflection FTIR values are attributed to evaporation during welding and/or weighing errors, rather than to loss through capsules during the experiments.

While oxygen fugacity (fO_2) could not be buffered in our experiments because they were H_2O-undersaturated, we could use the Fe contents of our post-run (Fe)-Au-Pd sample capsules to monitor the experimental fO_2, using the calibrations developed in our lab (Weber, 2010) and by Barr and Grove (2010). These calibrations are rooted in the fO_2-dependence of the equilibrium between Fe in the capsule metal and coexisting melt. For our experiments, this method yielded fO_2 values straddling the NNO buffer (Huebner and Sato, 1970), ranging from NNO-0.5 to NNO+0.2. These fO_2 conditions are slightly more reducing than has been estimated for magmas at Jorullo based on whole rock Fe^{3+}/Fe^{2+} ratios (~NNO+1; Luhr and Carmichael, 1985), but are within the range appropriate for primitive magmas from the TMVB as a whole (e.g., Wallace and

Carmichael, 1999). Redox conditions for ID-16 have been assumed to be near the FMQ buffer (~NNO-0.7) based on spinel analyses from the pre-caldera lavas at Okmok (Nye and Reid, 1986). The fO_2 ranges of our experiments are therefore also appropriate for ID-16 melts.

3.3.4. Approach to Equilibrium

We used the following criteria to assess experimental equilibrium: 1) chemically homogeneous glass and sub- to euhedral, unzoned crystals, 2) mass balance calculations with sums of the squares of the residuals, $\sum r^2$, less than 1.0, and 3) olivine-melt Fe/Mg partition coefficients (K_D) within the range 0.33±0.03 (Toplis, 2005). Mass balance calculations that yielded $\sum r^2 > 1.0$ were commonly traceable to discrepancies in Na_2O or FeO. Some experiments, particularly those with higher H_2O contents, underwent slight quench modification resulting in quench overgrowths on equilibrium crystals (e.g., dendrites and thin Fe-rich rims), which contributed to poorer mass balance results. When mass balance results were inconsistent with visual estimates of mineral modes, we used visual estimates of the modal abundances of phases (Appendix A), provided that the experiment met the other criteria for equilibrium.

3.4. Results

3.4.1. P-T-H_2O Phase Relations for Basaltic Andesite JR-28

In Figure 7a-c, we show the near-liquidus P-T phase relations for JR-28 at three different nominal H_2O contents: 3, 5, and 7 wt.% H_2O. Our focus is on the silicate phase stabilities, and we do not ascribe significance to the appearance, or not, of trace quantities of spinel, because this phase's stability is a strong function of fO_2, which was not explicitly controlled in our experiments. The quantities of spinel, when it appears, are

vanishingly small and so do not affect our mass balance calculations or the silicate phase equilibria in any significant way. The compositions of experimental glasses and crystalline phases are given in Appendix B.

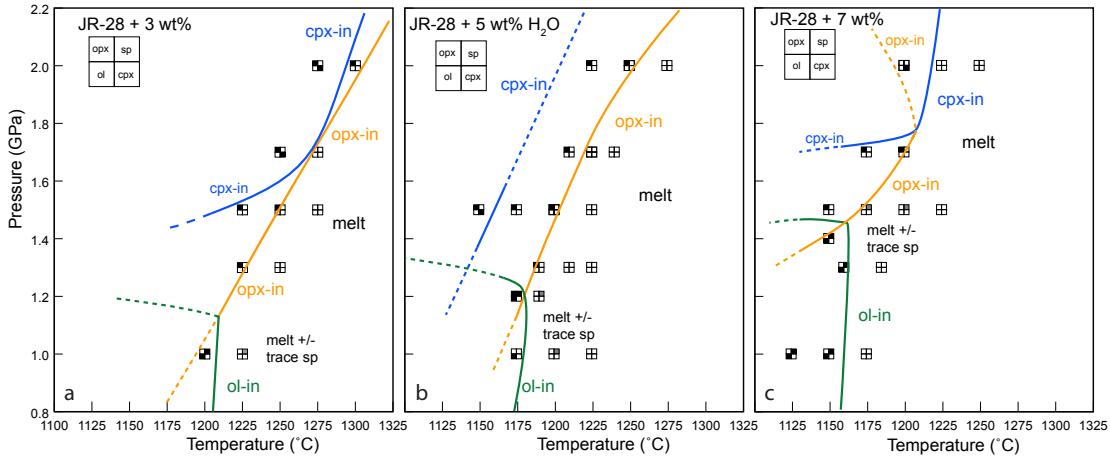

Figure 7. P-T phase relations for JR-28 with a) 3 wt% H_2O b) 5 wt% H_2O and c) 7 wt% H_2O.Open symbols are superliquidus conditions, and stable crystalline phases in sub-liquidus runs are indicated by filled squares. Light gray filled squares indicate the mineral is present in trace amounts. Mineral-in curves are shown as solid lines, grading to dashed lines where uncertainty increases due to sparse experimental coverage. Ol: olivine, cpx: clinopyroxene, opx: orthopyroxene, sp: spinel

With 3 wt% added H_2O (Figure 7a), olivine (ol) is the liquidus phase until ~1.1 GPa, above which it is replaced by orthopyroxene (opx). JR-28 co-saturates with augite (cpx) and opx at 1.7 GPa. Augite joins the assemblage 10–20ºC below the liquidus at 2.0 GPa. Experiments with 5 wt% H_2O show similar results, with olivine persisting as the primary crystalline phase to pressures ≤1.2 GPa. The melt (98% by mass) is multiply saturated with ol, opx, and Cr-rich spinel at 1.2 GPa and 1175 ºC. At pressures ≥1.3 GPa, the primary liquidus phase is opx. In contrast to the 3 wt% H_2O experiments, we observe cpx in only one 5 wt% H_2O experiment, crystallizing 50ºC below the liquidus at 1.5 GPa. With 7 wt% H_2O, the olivine stability field expands, and olivine remains the liquidus

phase to ~1.4 GPa, where it is replaced by opx to 1.7 GPa. At this higher H_2O content, cpx replaces opx as the primary liquidus phase at high pressure. In all near-liquidus experiments, olivine compositions are Fo_{87-88} and orthopyroxene En_{85-88}. Of particular note in Figure 7 is the migration of the point of ol+opx co-saturation to lower T and higher P with increasing H_2O content.

3.4.2. P-T-H_2O Phase Relations for High-MgO Basalt ID-16

P-T diagrams were also constructed for ID-16 with 2 and 5 wt% added H_2O, with particular emphasis on constraining the liquidus (Figure 8).

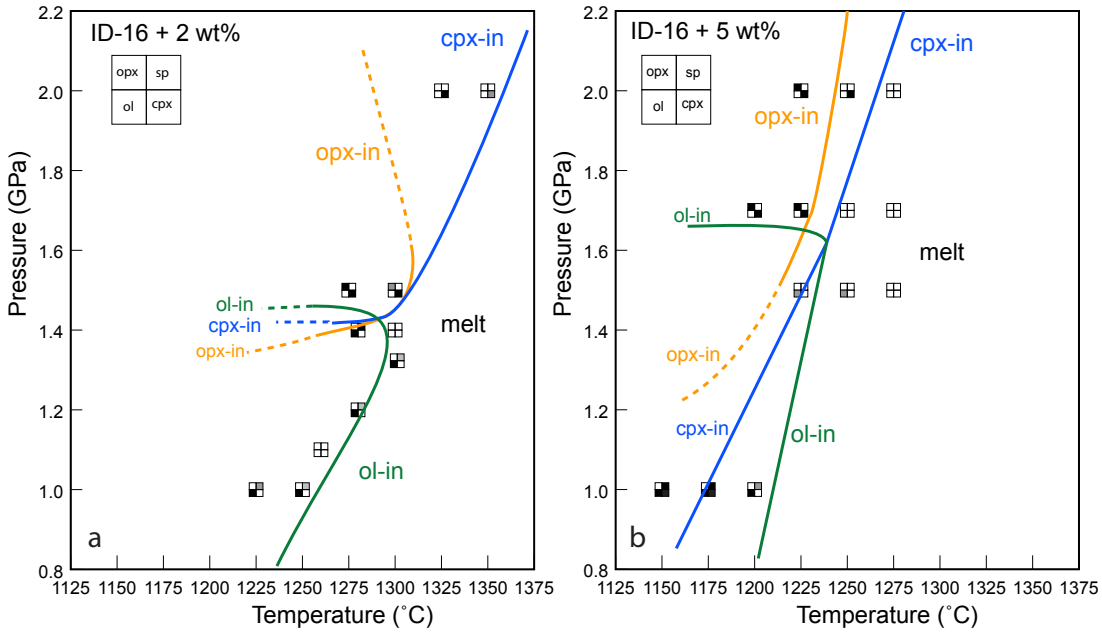

Figure 8. P-T phase relations for ID-16 with a) 2 wt% H_2O and b) 5 wt% H_2O.Open symbols are superliquidus conditions, and stable crystalline phases in sub-liquidus runs are indicated by filled squares. Lines and symbols as in Figure 7.

With 2 wt% added H_2O, olivine appears on the liquidus at pressures 1.0–1.4 GPa (Figure 8a). At 1.5 GPa and 1300 °C the mineralogy changes, and the melt (94% by mass) is multiply saturated with clinopyroxene and trace amounts of orthopyroxene

(Appendix A). This is the only experiment with ID-16 where opx crystallizes on the liquidus. Clinopyroxene is the only crystalline phase observed at 2.0 GPa. With 5 wt% H_2O (Figure 8b) at 1.0 GPa, olivine appears on the liquidus at 1200 °C, followed by cpx at 1175°C. Olivine remains the primary crystalline phase until it is apparently replaced by cpx at 1.7 GPa. We base this inference on the fact that our hottest crystal-bearing experiment at 1.7 GPa at 1225 °C, contains both cpx and opx, but in very different proportions (12.7 wt% and 1.4 wt%, respectively). We interpret the more abundant phase, cpx, to be the true liquidus phase and infer that a slightly hotter experiment would lack opx, and contain only cpx in addition to melt. Orthopyroxene appears to crystallize just beneath the cpx liquidus at pressures ≥1.7 GPa. These results, and those for JR-28, are summarized in the P-T projections of the H_2O-undersaturated liquidus surfaces for these compositions shown in Figures 9 and 10 and are discussed in the next section.

3.4.3. Near-liquidus Phase Relations of JR-28 and ID-16

Because we are interested in constraining the permissible residual mineralogy with which these two melts could have been in equilibrium, we will focus here solely on their near-liquidus phase relations. By considering only experiments with melt fractions, F, closely approaching 1.0 (F > 0.95, Appendix A), we can identify the crystalline phases that would be in equilibrium with melts with the bulk compositions of JR-28 or ID-16, with various H_2O contents, at the pressures investigated. Runs with melt fractions appreciably lower than 1.0 have correspondingly evolved melt compositions and so cannot be interpreted in this manner. By mapping the near-liquidus phase relations in P-T-H_2O space (Figures 9 and 10), we treat the liquid composition as constant and explore how permissible residual mineral assemblages change with P, T, and H_2O.

The results of Figure 7a-c are combined in Figure 9 as a summary projection of the H_2O-undersaturated liquidus surface onto the P-T plane for JR-28. We have mapped onto this diagram the identities of the mineral(s) that appear on the liquidus at each P, T, and H_2O content and have modeled the anhydrous mineralogy using pMELTS and MELTS (Asimow and Ghiorso, 1998; Ghiorso et al., 2002; Ghiorso and Sack, 1995).

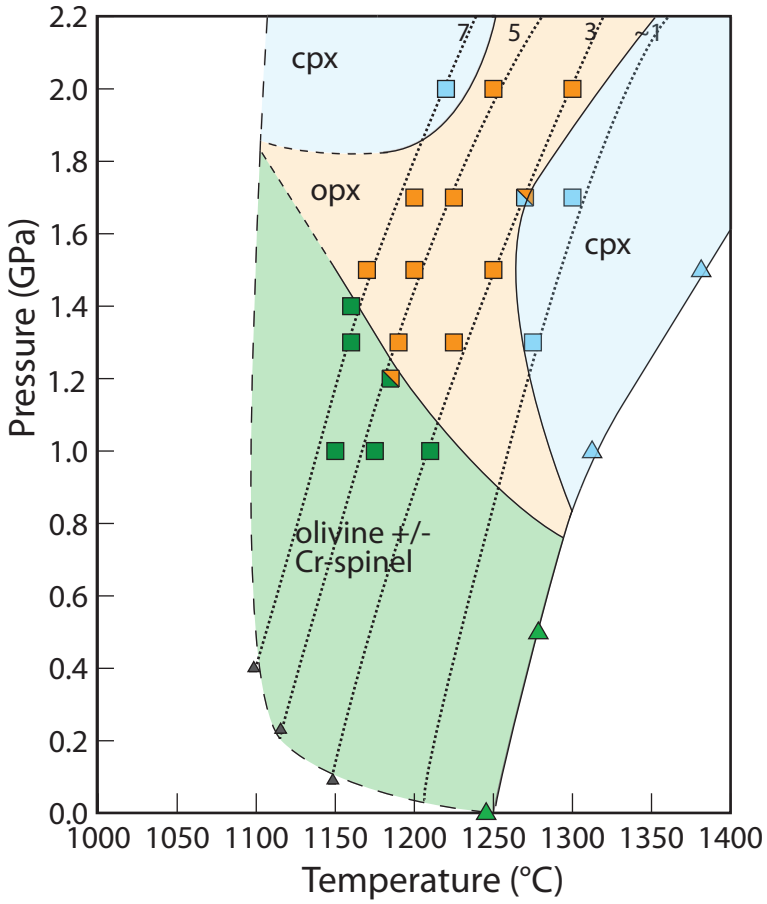

Figure 9. Near-liquidus P-T-H_2O phase relations for JR-28. The positively sloping, concave down curve at the highest temperatures is the dry liquidus (large triangles) calculated with pMELTS and MELTS using our starting composition (Ghiorso and Sack, 1995; Asimow and Ghiorso, 1998; Ghiorso et al., 2002). The leftmost dashed line represents the estimated H_2O-saturated liquidus constrained at low pressures (small triangles) using MELTS and VolatileCalc (Newman and Lowenstern, 2002) and unconstrained at high-pressure. The area between these curves shows the projected H_2O-undersaturated liquidus surface. The dotted curves represent the H_2O-undersaturated liquidus curves from Fig. 7 and are isopleths of constant H_2O content constrained by our lowest and highest temperature superliquidus and subliquidus experiments, respectively.

We can infer from this projection the P-T-H_2O conditions at which JR-28 melts would be in equilibrium with two or more mantle minerals by observing where two or more mineral stability fields intersect in P-T-H_2O space.

In Figure 9 we observe that at the highest pressures investigated, opx is the liquidus phase at 3 and 5 wt% H_2O but is replaced by cpx at more H_2O-poor conditions as seen experimentally and predicted by pMELTS. One experiment at 3% wt% H_2O, 1.7 GPa, and 1250 °C constrains the cpx-opx cotectic. The opx-ol cotectic is well constrained by the experiments with 5 and 7 wt% H_2O, with olivine becoming stable at higher pressures at the expense of opx with increasing H_2O contents. Our constraints on the ol-opx cotectic at H_2O contents less than 3 wt% are poor due to sparse experimental coverage.

Figure 10 is a summary projection for ID-16 that shows the hydrous, near liquidus mineralogy with 2 and 5 wt% H_2O (from Figure 8). The lower bulk SiO_2 and higher CaO contents of ID-16 relative to JR-28 lead to different P-T-H_2O phase stability fields. At 1.7–2.0 GPa, cpx is the liquidus phase at all H_2O contents explored. At 1.5 GPa, cpx is on the anhydrous liquidus, cpx and opx are on the liquidus with 2 wt% H_2O, and olivine and spinel are on the liquidus with 5 wt% H_2O. This phase assemblage (olivine ± spinel) persists on the liquidus at all H_2O contents at P<1.5 GPa, with near liquidus olivine of Fo_{87-89}.

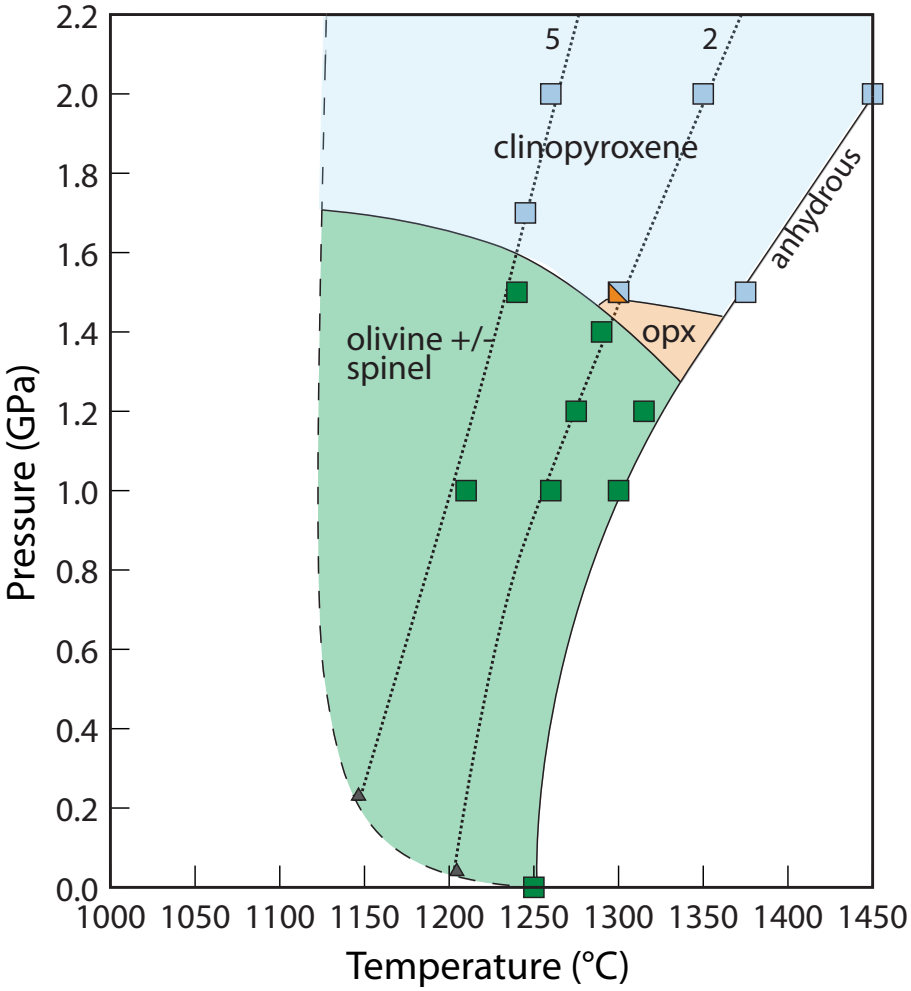

Figure 10. Near-liquidus P-T-H_2O phase relations for ID-16. Lines and symbols as in Figure 9. Note point of three-phase saturation at ~1.4 GPa and 1280 °C

Olivine and opx compositions in our experiments are typically slightly more Fe-rich (e.g. Fo_{87-89}, En_{87}) than would be expected for mantle values (Appendix A). Both starting compositions are calculated to be in equilibrium with $Fo_{89.6}$ olivine at the experimental fO_2 of NNO (with Fe^{3+}/Fe^{2+} calculated from Kress and Carmichael, 1991). The slightly more reducing fO_2 of some experiments, together with modest Fe-gain from the capsules that was detected in some runs are likely the cause of the more Fe-rich olivines. However, because the pressure dependence of olivine-opx saturation is mainly a

function of the SiO_2 activity in the melt rather than Fe-Mg exchange (Ghiorso et al., 1983), these small differences in olivine and opx composition should have only minimal effects on inferred equilibration pressures. Thus the phase relations shown in Figures 9 and 10 should be appropriate for interpreting pressures of equilibration of these primitive melts with a mantle assemblage.

3.4.4. Multiple Saturation

Phase diagrams like Figures 9 and 10 enable tracking of multiple saturation points in P-T space as a function of H_2O content. Figure 10 shows that there are no P-T conditions at H_2O contents of interest (>5% H_2O) under which JR-28 could be in equilibrium with lherzolite (ol, opx, cpx ± sp). However, there exist multiple P-T-H_2O conditions where this melt could be saturated with harzburgite, shown by the opx-ol boundary. The conditions of permissible multiple saturation in this assemblage shift to lower temperatures and higher pressures with increasing H_2O content (see also Figure 7). Such a point was found experimentally at 5 wt% H_2O at 1175 °C and 1.2 GPa. While we also observe a permissible pyroxenite assemblage (cpx+opx only) at 2.0 GPa and ~1225°C, we do not consider this an appropriate source assemblage for JR-28 for reasons that are discussed in Section 3.5.1. Our observations from Figure 9 lead us to conclude that JR-28 last equilibrated with a harzburgitic mantle source between 1.2–1.4 GPa and at temperatures of 1150–1175 °C for H_2O contents consistent with the melt inclusion data (≥5.5 wt% H_2O). To test whether a harzburgite assemblage is in equilibrium with our starting compositions at the P-T-H_2O conditions of interest, we performed two forced saturation experiments at 1.2 GPa, 1175 °C, 5 wt% H_2O, and 1.4 GPa, 1150 °C, 7 wt% H_2O. For these experiments we added mineral separates of $Fo_{90.9}$ olivine and $En_{91.6}$

orthopyroxene to our natural rock powder, thereby forcing our composition to be in equilibrium with a harzburgite residue. These experiments produced large pools of homogeneous glass with well-developed olivine crystals and zoned crystals of orthopyroxene. The olivine in equilibrium with JR-28 melt and 5 wt% H_2O was Fo_{89}, while the orthopyroxene had cores of En_{90} and rims of En_{88} composition. Olivine compositions in equilibrium with JR-28 melt and 7 wt% H_2O were Fo_{87} and En_{87-88}. The melt compositions in these experiments were similar to JR-28, but had slightly lower SiO_2 and slightly higher Al_2O_3 and FeO^T (Appendix B). Thus, the results of our forced saturation experiments agree with our inverse experiments, with similar olivine and orthopyroxene compositions in equilibrium with our starting melt composition.

In contrast to JR-28, there are P-T-H_2O conditions where ID-16 is saturated in a lherzolitic mantle assemblage, estimated from Figure 10 to be at 1.4 GPa, ~1280 °C, and ~2% H_2O (see also Figure 8a). These experimental results are consistent with the H_2O estimates (~2.5 wt%) of younger Okmok magmas based on melt inclusions (Zimmer et al., 2010). Draper and Johnston (1992) observed a point they interpreted to represent 5 phase saturation (ol, opx, cpx, plagioclase, and spinel) near the anhydrous liquidus at 1.2 GPa and 1315 °C. However, despite being <10 °C cooler than the liquidus at this pressure, this experiment contained ~45% crystals with a coexisting melt that differs considerably from the starting ID-16 bulk composition. In addition, their experiments were estimated to be at more reducing fO_2 conditions than those performed here. We repeated their 'multiple saturation' experiment in Fe-preconditioned capsules at the same pressure and temperature (1.2 GPa and 1315 °C) and found ID-16 melt in equilibrium with only trace amounts of olivine. Clearly the ol-opx and opx-cpx mineral-in curves

under anhydrous conditions converge on or very near the liquidus at 1.3–1.5 GPa but the details are not resolvable given our ±10 °C temperature uncertainty and the large amount of crystallization that occurs just beneath the liquidus at this pressure. Our results for ID-16 suggest that the primary melts beneath Okmok were derived by <~20% melting of a wet lherzolite source such that clinopyroxene remained in the residuum. This is contrary to the 30–35% lherzolite source melting originally suggested by Nye and Reid (1986) based on incompatible trace element abundances. Further, our hydrous experimental phase relations suggest subarc mantle temperatures of ~1275–1300 °C at the inferred depth of equilibration (~45 km), as opposed to the much hotter (1500–1600 °C) mantle required for their original model of magma genesis (Nye and Reid, 1986).

3.5. Discussion

Although there is a general consensus that primitive basaltic magmas in arcs form by hydrous melting of mantle peridotite, there have been surprisingly few experimental studies that test this interpretation using high-pressure phase equilibria of primitive melt compositions under H_2O-undersaturated conditions. In the following sections, we use the results of our experiments to test some models for arc magma generation and make generalizations about the effects of source composition (lherzolite vs. harzburgite) in intraoceanic and continental arc settings. In addition, we put our experiments in context with current geodynamic models that make predictions about the thermal structure of the mantle wedge beneath arcs.

3.5.1. Source Composition for Jorullo Volcano: Pyroxenite vs. Harzburgite Residue

We interpret the phase relations of Figure 9 as evidence that JR-28 last equilibrated with a harzburgite source in the upper mantle and observe that there are no

hydrous P-T conditions where a fertile lherzolite source is permissible. An alternative possibility, however, is that JR-28 formed in equilibrium with a pyroxenite residue at 2.0 GPa and ~1225 °C at H_2O contents of ~5–7 wt%. Recently, Straub et al. (2008) concluded that a pyroxenite source beneath the Mexico City region to the east of Jorullo volcano was responsible for generating primitive andesitic melts that crystallize Ni-rich olivine. They suggested that the pyroxenite formed as a Si-rich slab component reacted with mantle olivine to produce "reaction orthopyroxene" to a sufficient extent that residual olivine in the original peridotite was eliminated. In their model, the pyroxenite partial melts subsequently mix with peridotite partial melts to form a range of calc-alkaline basaltic andesite to andesite compositions. According to Straub et al. (2008), the main diagnostic criterion for distinguishing pyroxenite melts is higher Ni in olivine phenocrysts than is found in melts derived from peridotite melting. Jorullo olivines contain Ni contents as high as 0.43 wt% in Fo_{91}, close to the maximum values that would be expected for melts derived from refractory harzburgite and lower than values calculated for pyroxenite melts (see Figure 12 of Straub et al., 2008). Therefore, the Ni-in-olivine criterion does not provide strong support for a pyroxenite source for JR-28. Moreover, the high-pressure experiments of Kogiso et al. (2004) show that in order to produce high-Mg basaltic andesite melts such as JR-28 from pyroxenite melting, the residue must be silica-saturated, with residual garnet and accessory quartz. The absence of these phases in our high-pressure experiments, therefore, is also inconsistent with a pyroxenite source. Finally, we note that the very low Nb, Ta and Y concentrations in Jorullo lavas (Johnson et al., 2009) support the interpretation that JR-28 formed in equilibrium with a refractory harzburgite source.

3.5.2. Natural and Experimental Melts of Peridotite

Our results indicate that melting of, or reequilibration with, refractory mantle produces primitive liquids that are relatively rich in SiO_2 (52-56 wt%). Figure 11 shows the SiO_2 vs. TiO_2 systematics of natural primitive basalts to andesitic lavas from the TMVB, the Aleutians, and several other continental (Figure 11a) and intraoceanic (Figure 11b) arcs. These lavas all have MgO >8 wt%, with the exception of the modern Tonga boninites, whose most primitive compositions contain 6% MgO (Cooper et al., 2010). As mentioned above, the melt SiO_2 content appears to provide information regarding equilibration of primitive melts with lherzolitic versus harzburgitic sources.

Melt TiO_2 contents are affected by both the extent of depletion of the mantle source by previous melt extraction (Portnyagin et al., 2007) and the degree of melting during melt generation, with high degree melts, and/or melts from previously depleted sources having lower TiO_2 contents. A similar diagram has been used by Cooper et al. (2010, Figure 7) to characterize magma sources and processes in arc volcanic rocks. In general, primitive arc magmas show a wide range of TiO_2 concentrations that generally decrease with increasing SiO_2, with boninites as the most extreme endmember (Figure 11).

To compare experimental results with natural basalts and basaltic andesites, we have plotted our experimental starting compositions (large black stars) as well as experimental data (shaded fields) from studies that explored partial melting of compositionally variable mantle sources under hydrous and anhydrous conditions. We include experimental liquids that represent partial melts ($0.05<F<0.2$) of lherzolite (before cpx-out) and those that equilibrated with a harzburgite assemblage.

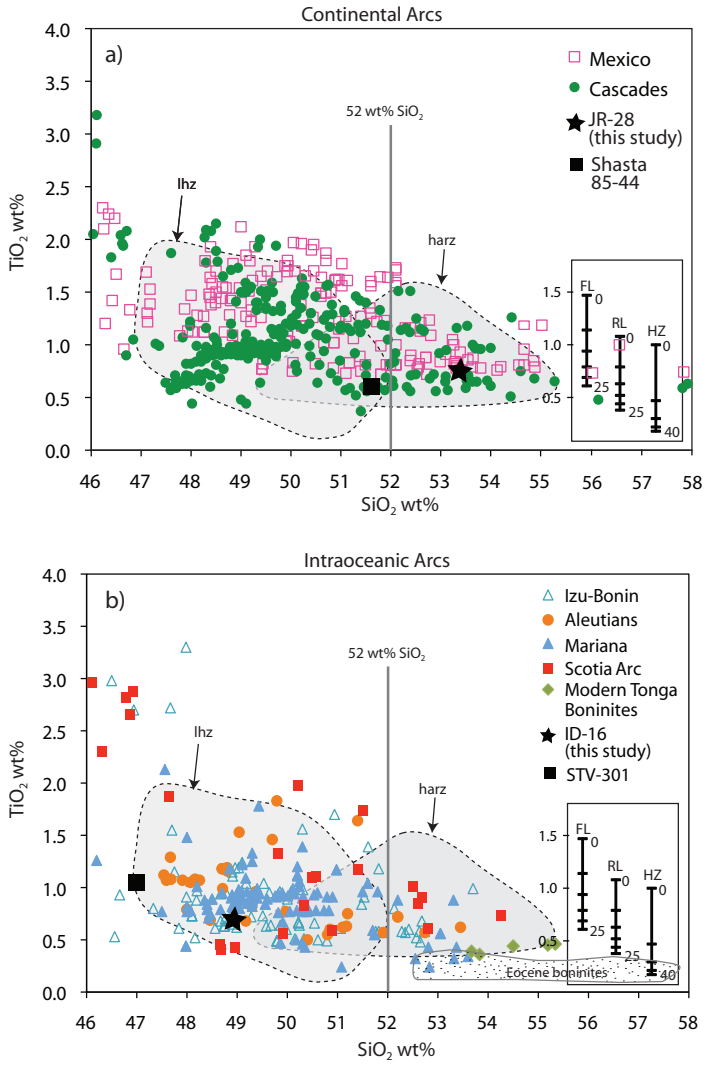

Figure 11. SiO_2 vs TiO_2 of mafic volcanic rocks with greater than 8 wt% MgO for a) continental and b) intraoceanic arcs. All data are from the GEOROC database. The data in b also include modern Tonga boninites with MgO of ~6 wt% (Cooper et al., 2010). Shaded fields show the range of experimental melts (F~0.05-0.2) in equilibrium with lherzolite (lhz) or harzburgite (harz) (Baker and Stolper, 1994; Falloon and Danyushevsky, 2000; Hirose and Kawamoto, 1995; Hirose and Kushiro, 1993; Kushiro, 1996; Pickering-Witter and Johnston, 2000; Schwab and Johnston, 2001). Black stars represent melts in this study (JR-28 and ID-16) plotted with melts from similar studies (Shasta 85-44, Baker et al. 2004; STV-301, Pichavant et al. 2002). Vertical lines show the range of TiO_2 expected for fertile lherzolite (FL), refractory lherzolite (RL), and harzburgite (HZ) for 0-25% or 0-40% partial melting using a batch melting model. FL is HK-66 (Hirose and Kushiro 1993), RL and HZ are TQ-40 and synthetic harzburgite HZ, respectively (Falloon and Danyushevsky, 2000). We use constant bulk distribution coefficients of 0.15 (FL), 0.12 (RL), and 0.08 (HZ).

Figure 11 shows that hydrous and anhydrous lherzolite melting produces basaltic compositions but does not produce liquids with >52 wt% SiO_2. While there is some compositional overlap with lherzolite melts, it appears that only a harzburgite assemblage can produce primitive melts that range from basalt to basaltic andesite in composition. Our results agree with observations of Kushiro (1972) and Wood and Turner (2009), who showed that increased SiO_2 and MgO contents in primitive melts are related to clinopyroxene undersaturation. On Figure 11, ID-16 lies within the region that can only be produced by lherzolite melting, whereas JR-28 lies within the field of experimental liquids that can only equilibrate with a harzburgite residue.

For comparison, we have also plotted a basaltic andesite from the Mount Shasta region (85-44, SiO_2=51.7, TiO_2=0.60) whose experimental hydrous phase relations were described by Baker et al. (1994). Their results suggest that 85-44 last equilibrated with a harzburgite residue at ~1.0 GPa and ~1200 °C with 3–5 wt% H_2O. This hydrous melt plots at the boundary of the lherzolite-melting field in Figure 11; however, it falls well within the harzburgite-melting field. In contrast, the near-liquidus hydrous phase relations of a primitive basalt from the Lesser Antilles (STV-301, SiO_2= 47.0 wt%, TiO_2=1.1 wt%) show a hydrous melt in equilibrium with fertile lherzolite at 1.15 GPa and 1235 °C with 1.5 wt% H_2O (Pichavant et al., 2002). When plotted on Figure 11, the bulk composition of STV-301 clearly falls within the field of melts from a lherzolite source. Provided a primitive rock composition does not plot in the area of overlap of the lherzolite and harzburgite fields, the relations shown in Figure 11 are useful for distinguishing the type of peridotite residues with which different primitive arc magmas last equilibrated.

Several other interesting features are apparent in Figure 11. With the exception of boninites, primitive melts in equilibrium with harzburgite appear to be more common in continental margin arcs compared to intraoceanic arcs (see also Cooper et al., 2010). In the case of continental arcs, true basaltic compositions come from a wide range of enriched to depleted lherzolite, with Mexico showing a greater proportion from an enriched source (Luhr 1997) and the Cascades showing a wider range of TiO_2 and, compared to Mexico, more depleted sources. In contrast, the intraoceanic arcs show generally more depleted basaltic compositions. The few basaltic andesites shown are from Alexander Island near the Antarctic Peninsula (Scotia), which are fore-arc magmas argued to be products of ridge subduction (McCarron and Smellie, 1998), and Kanaga Volcano (Aleutians), which are argued to be slab melts that have reacted with peridotite in the shallow mantle (Kelemen et al., 2003b). These comparisons suggest that at least some continental arcs have a greater proportion of harzburgite in the uppermost mantle wedge compared to intraoceanic island arcs. This harzburgite must be distributed heterogeneously, as both primitive basaltic and basaltic andesite melts occur in the continental arcs.

We have employed a simple batch melting model to show the range of TiO_2 concentrations for 0-25% partial melts of fertile lherzolite (FL) and refractory lherzolite (RL), and 0-40% partial melting of harzburgite (HZ) using experimental compositions of natural and synthetic peridotites (Falloon and Danyushevsky 2000; Hirose and Kushiro 1993). These models further illustrate that the most SiO_2-rich, TiO_2-poor samples from Mexico, including JR-28, have TiO_2 contents that are consistent with high-degree partial melting of FL or RL, past the point of cpx exhaustion, or low degree melting of, or

equilibration with, a harzburgite source. Figure 11 also suggests that the very high SiO_2 and low TiO_2 contents of boninites require equilibration with a harzburgite residue formed by either 1) larger extents of single-stage melting at unusually hot mantle conditions (e.g., Sobolev and Danyushevsky, 1994) or 2) smaller degrees of fluid-fluxed melting of depleted harzburgite residuum at typical mantle temperatures (~1300 °C) after multistage back-arc melting events (Cooper et al., 2010).

3.5.3. Thermal State of Arcs

Recently, there have been significant efforts focused on modeling the thermal structure of arcs worldwide to quantify the effects of slab geometry, slab-mantle coupling depth, temperature-dependent mantle viscosity, and convergence rate (Kelemen et al., 2003a; Manea et al., 2005; Syracuse et al., 2010; van Keken et al., 2009; Wada and Wang, 2009). These models attempt to account for geophysical observations and make predictions about the steady-state thermal conditions in subduction zones. However, petrologic estimates of temperatures within the mantle wedge beneath arcs are commonly several hundred degrees hotter than are predicted from 2D thermal models (Elkins-Tanton et al., 2001; Kelemen et al., 2003a). In this section, we compare our experimental P-T conditions to geodynamic models of the thermal structure of the subarc mantle wedge. We also use our experimental P-T estimates to test a recent thermobarometer for calculation of P-T conditions of mantle-melt equilibration for primitive compositions such as JR-28 and ID-16.

The experimental pressures of equilibration can be converted to depth assuming an average crustal density of 2800 kg/m^3 for the MGVF (Ortega-Gutierrez et al., 2008) and 3000 kg/m^3 for the Central Aleutians (Shillington et al., 2004). This results in

apparent melt-mantle equilibration depths of 42–48 km (MGVF) and 46 km (Central Aleutians). Calculated P-T conditions using the thermobarometer of Lee et al. (2009) for our experimental compositions are 1.0–1.1 GPa (35–37 km) and 1157–1182 °C for JR-28 with 5–7 wt% H_2O, respectively. The same thermobarometer applied to ID-16 with 2 wt% H_2O yields P-T estimates of 1.1 GPa (39 km) and 1276 °C. The calculated temperatures agree well with our experimental results, but the calculated pressures are underestimated. We note, however, that our experiments fall within the limits of uncertainty, ±0.2 GPa, of the barometer.

Because the experimental olivine in JR-28 is less magnesian than the most Fo-rich olivine at Jorullo (Fo_{91}) and also less magnesian than olivine in natural refractory harzburgite, we calculated the P-T conditions of mantle-melt equilibration expected for a compositionally similar melt that is in equilibrium with Fo_{91} instead of Fo_{90}. To do this we added 0.1 wt% increments of equilibrium olivine back into the JR-28 composition until a new composition was reached that was in equilibrium with Fo_{91}. Pressures calculated by the Lee et al. model are sensitive to changes in SiO_2 and MgO, with decreasing melt SiO_2 resulting in higher equilibration pressures. The calculated P-T conditions for JR-28 (5-7 wt% H_2O) in equilibrium with Fo_{91} are increased in both temperature (~25 °C) and pressure (~0.1 GPa), thereby increasing equilibration depths by about 4 km relative to calculations at Fo_{90}.

In Figure 12 we plot the approximate depths of last melt equilibration from our experimental results (labeled “JR-28 exp” and “ID-16 exp”) and thermobarometric calculations from the Lee et al. model (“Fo_{90}” and “Fo_{91}” for JR-28, “Fo_{90}” for ID-16) with temperature profiles of the wedge from the Moho to the hottest part of the wedge in

each region. We use steady-state thermal models of Syracuse et al. (2010) and Johnson et al. (2009) for the Central Aleutians and the MGVF volcanic fronts, respectively. The MGVF model predicts temperatures approaching, but still cooler than, our experimental results. The thermobarometric calculations of Fo_{90} vs. Fo_{91} show that a more refractory source causes a small increase in equilibration pressure and temperature. The model for the Central Aleutians predicts temperatures that are significantly cooler (>600 °C) at the depth of equilibration of ID-16. These discrepancies, particularly for the Aleutians, suggest that the steady-state thermal models fail to account for important processes occurring in the mantle wedge in subduction zones.

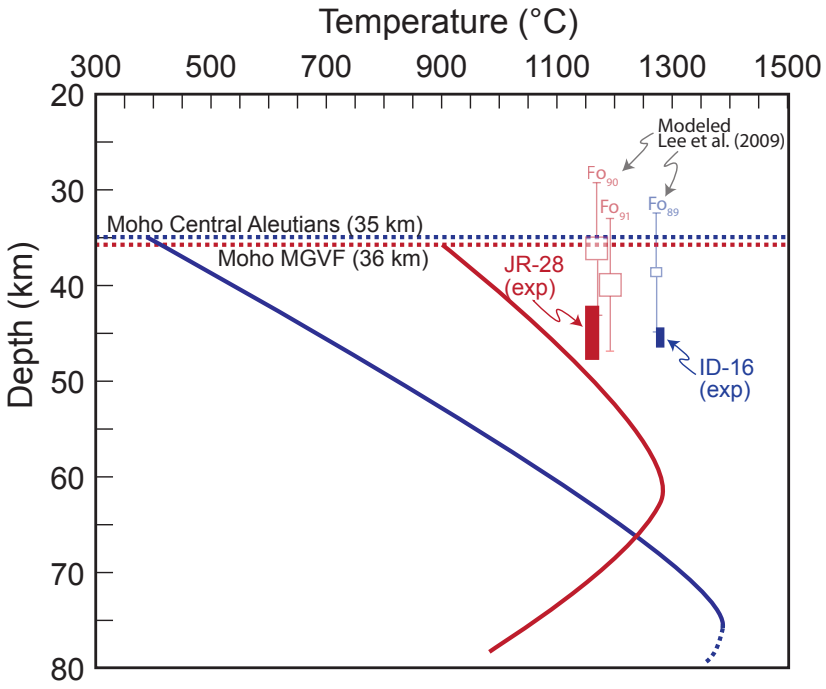

Figure 12. Geodynamic model temperature profiles (solid lines) from Moho (dashed lines) through mantle wedge for Aleutians (Syracuse et al., 2010, model X25) and MGVF (Johnson et al., 2009). Boxes labeled ID-16(exp) and JR-28(exp) indicate experimentally inferred P-T conditions of last melt equilibration. Also shown are P-T calculations for JR-28 in equilibrium with Fo_{90} and Fo_{91} and ID-16 in equilibrium with Fo_{90} using the thermobarometer by Lee et al. (2009) accounting for ±0.2 GPa uncertainty of model. Note that the experiments indicate hotter temperatures at a given depth than predicted by the geodynamic models. See text for discussion

This could be due to problems with the geodynamic models or their underlying assumption that arc systems are, in fact, at steady-state (Hall et al., 2010). More likely, the discrepancies could be caused by the tremendous quantities of heat advected upward by magmas ascending from depths where the thermal maxima within the wedge are predicted to occur. England and Katz (2010) recently invoked such a model, wherein magma segregation from the "hot nose" of the wedge heats the upper part of the mantle wedge sufficiently to perturb the isotherms upward, resulting in locally warmer temperatures at shallower depths. Kelemen et al. (2003a) provide a similar interpretation to account for such discrepancies between petrologic and geophysical estimates of temperature for a given depth. This local heating allows progressive melting of the surrounding peridotite causing the residue to become more refractory as clinopyroxene is exhausted and incompatible elements are removed into the melt phase.

We conclude that hydrous mafic melts initially form by melting in the hottest part of the mantle wedge and then reequilibrate with the shallow upper mantle before ascent into the crust. Where upper mantle lithologies include harzburgite, ascending melts can become more SiO_2-rich through the reequilibration process (e.g., Grove et al., 2003, 2006). The greater proportion of high-Mg basaltic andesite magmas in some continental arcs compared to intraoceanic arcs suggests that harzburgite is more widespread beneath continental margins, perhaps because the various processes that form continental crust lead to a greater proportion of refractory harzburgite in the shallow upper mantle. In contrast, with the exception of boninite-forming arcs, lherzolite appears to be the dominant residuum of the subarc mantle in intraoceanic arcs. Consequently, melts such as ID-16 that equilibrate at shallow depths beneath intraoceanic arcs are likely to remain

basaltic, rather than evolving to basaltic andesite. Our conclusion about shallow upper mantle reequilibration is consistent with previous studies of the Cascades (Elkins-Tanton et al., 2001) and Aleutians (Kelemen et al., 2003b), but contrast with the findings of Kelley et al. (2010) for the Marianas. They used primitive melt compositions estimated from melt inclusion data combined with the Lee et al. (2009) barometer to conclude that primitive Mariana arc melts last equilibrated within the hot core of the mantle wedge. Future experimental work should investigate these differences to further improve our understanding of melt generation and reequilibration beneath arcs.

3.6. Summary

Our high-pressure experiments on primitive compositions from two distinct subduction zone settings suggest that variations in upper mantle mineralogy (lherzolite vs. harzburgite) greatly affect the compositions of arc magmas. More SiO_2-rich primitive basaltic andesites such as JR-28 from Central Mexico are likely a result of H_2O-rich melts rising from the hot core of the wedge and reequilibrating with harzburgite in the shallow upper mantle. In contrast, basaltic magmas, such as ID-16 from the Central Aleutians equilibrate with a fertile lherzolitic residue. Experimental data for both compositions suggest hotter temperatures in the uppermost mantle wedge than are predicted by steady-state geodynamic model results, though the discrepancy is relatively small for Central Mexico. These discrepancies are probably due to advective heating by magma rising from the hot core of the mantle wedge. The common disagreement between petrologic P-T estimates and those of steady-state thermal models suggests that either melt reequilibration and advective heating of the shallow upper mantle are significant in most arcs or that temperature distributions in the subarc mantle are commonly not at

steady state, contrary to the assumption in most geodynamic models (e.g., Hall et al., 2010).

3.7. Bridge

In Chapter III I focus on comparisons between intraoceanic and continental arcs, using a Mexican basalt as representative of continental arcs as a whole. In the next chapter I explore the geochemical variations that occur among primitive continental arc basalts, all from the TMVB. I use experimental phase relations for Jorullo lavas in this chapter, and present experimental data for two additional primitive basalts from the TMVB. One aim of Chapter IV is to better characterize mantle heterogeneity within continental arc settings as expressed by variations in SiO_2, alkalies (Na_2O+K_2O), magmatic H_2O, and trace element signatures.

CHAPTER IV

EXPERIMENTAL CONSTRAINTS ON THE ORIGINS OF SHOSHONITIC AND INTRAPLATE ALKALINE BASALTS FROM THE TRANS-MEXICAN VOLCANIC BELT

This chapter is co-authored by Drs. Paul Wallace and Dana Johnston and will be submitted to a special issue of *Contributions to Mineralogy and Petrology* in honor of the late Professor Ian Carmichael. I am the primary author of this manuscript, completed all laboratory experiments, and performed data analyses. Both co-authors contributed editorial and financial support for this work.

Introduction

The variability of SiO_2, alkalies (Na_2O+K_2O), volatiles (H_2O, CO_2), and incompatible trace elements in primitive arc lavas worldwide indicates heterogeneities in both the distribution of slab-derived components and in the extent of prior depletion by melting of the subarc mantle. This study focuses on the origins of primitive lavas from the Trans-Mexican Volcanic Belt (TMVB) that appear to be transitional between two endmember components: highly potassic minette and leucitite, and intraplate alkaline (ocean island basalt, or OIB-type) basalt. In the TMVB, K_2O-rich magmas have erupted as phlogopite-bearing minette and leucitite, hornblende trachybasalt, and primitive absarokite, and these have erupted alongside more volumetrically abundant calc-alkaline basalt and basaltic andesite (Allan and Carmichael 1984; Luhr et al. 1989; Wallace et al. 1992). The potassic compositions erupted along the volcanic front in the western TMVB show geochemical signatures consistent with subduction processes (fluid-fluxing;

Vigouroux et al. 2008). In contrast, primitive alkaline lavas with OIB-like trace element patterns typically erupt behind the volcanic front in the rear-arc and are likely H_2O-poor decompression melts of upwelling asthenosphere (Luhr 1997; Cervantes and Wallace 2003; Johnson et al. 2009). There exists a spectrum of lavas between these two endmembers that spans a range of K_2O contents, pre-eruptive H_2O concentrations, and incompatible trace element signatures, signifying origins from an enriched mantle source (similar to the source for OIB or EMORB) that may have interacted with a subduction component. These transitional lavas have been observed across volcanic arcs at the volcanic front (e.g., Luhr 1997), toward the rear arc (Kurile Arc; e.g., Kuritani et al. 2008), and within back-arc basins (Vanuatu; e.g., Sorbadere et al. 2011). In this study we concentrate on alkaline lavas that have erupted at or just behind the volcanic front in Mexico.

We focus our experimental efforts on a hornblende-bearing trachybasalt erupted from Cerro La Pilita, Central Mexico and an alkali basalt from Ayutla, western Mexico. Both lavas are elevated in total alkalies (K_2O+Na_2O), vary in their K_2O contents, and indicate varying degrees of interaction with a slab-derived component as evidenced by incompatible trace element and estimated magmatic H_2O concentrations. In this study we use high-pressure phase equilibria to constrain the P-T conditions of magma equilibration at H_2O-undersaturated conditions. The near-liquidus mineralogy of these samples allows us to constrain the permissible mantle residues at such conditions and discuss heterogeneities in upper mantle chemistry. We also use trace element modeling to describe the compositional range of magmas that form by fluxing heterogeneous mantle components with high-temperature slab-derived fluids or melts. Although these

transitional compositions are less common at the volcanic front compared to the calc-alkaline lavas, they are an important lava type, as they reflect the complex history of fluid-driven mass transfer from the slab to the mantle wedge during arc development and the geochemical diversity of mantle source components.

Geologic Setting

Tectonic Overview

The Trans-Mexican Volcanic Belt (TMVB, Figure 2) is a 1000 km long east-west trending belt of mafic cinder cones, shields, and maars, intermediate stratovolcanoes, and rhyolite domes. The volcanic features in the TMVB are associated with subduction of two young, hot plates beneath the North American continent: the Rivera plate in the West, and the Cocos plate toward the east. The Rivera Plate (10-11 Ma) converges at a rate of 23 mm/yr, with slab dip angles beneath the volcanic front estimated to be relatively steep (~60-70°) (Yang et al. 2009). The Jalisco block in western Mexico is structurally defined by the Tepic-Zacoalco Rift to the north, and the Colima Rift to the east. Ayutla is located within the Jalisco block at the volcanic front. At the eastern edge of the Rivera plate there exists a gap between the two slabs, providing a window at depth where hot asthenosphere may flow around the plate boundaries (Ferrari et al. 2001; Yang et al. 2009). This gap, coupled with the initiation of slab steepening, rollback, and trench migration in the late Miocene may have induced flow of hot asthenosphere into the mantle wedge and is suggested to be responsible for many of the OIB-type lavas observed in the western TMVB (Ferrari et al. 2001).

The Michoacán-Guanajuato Volcanic Field (MGVF) lies east of Colima and is associated with relatively fast subduction of the Cocos plate. Convergence rates at the

Middle America Trench increase slightly eastward, from 52 mm/yr beneath the Michoacán-Guanajuato Volcanic Field (MGVF) to 59 mm/yr beneath Mexico City and the Chichinautzin Volcanic Field (CVF) (Pardo and Suarez 1995). The MGVF is characterized by monogenetic basalt to basaltic andesite cinder cones that are Late Pliocene to historic in age (Luhr and Carmichael 1985) and medium sized mafic to intermediate shield volcanoes (Hasenaka and Carmichael 1985). Though the slab dip angle is not well constrained beneath MGVF, it is estimated to be much shallower (~30°C) than the Rivera slab (Pardo and Suarez 1995). La Pilita lies within the MGVF approximately 3 km south of the historically active Jorullo volcano.

Geochemistry of Associated Lavas

Primitive magmas in the TMVB show a wide range of major element compositions. In Figure 13 we show the range in SiO_2 and K_2O of primitive (>8 wt% MgO) samples from western Mexico (including Colima, Jalisco, and Mascota), the MGVF, and the CVF. Magmas from the CVF and the MGVF generally are medium-K calc-alkaline basalt and basaltic andesite, whereas western Mexico magmas range from med-K calc-alkaline basaltic andesite to absarokite and potassic shoshonite (minette).

Incompatible trace element patterns normalized to depleted MORB mantle (DMM, Salters and Stracke 2004) are shown in Figure 14 for the two samples of this study. For comparison, primitive melt inclusions within olivine from MGVF basalts and basaltic andesites (hereafter referred to as BBAs), and western Mexico minettes and basanites (Vigouroux et al. 2008; Johnson et al. 2009) are also shown.

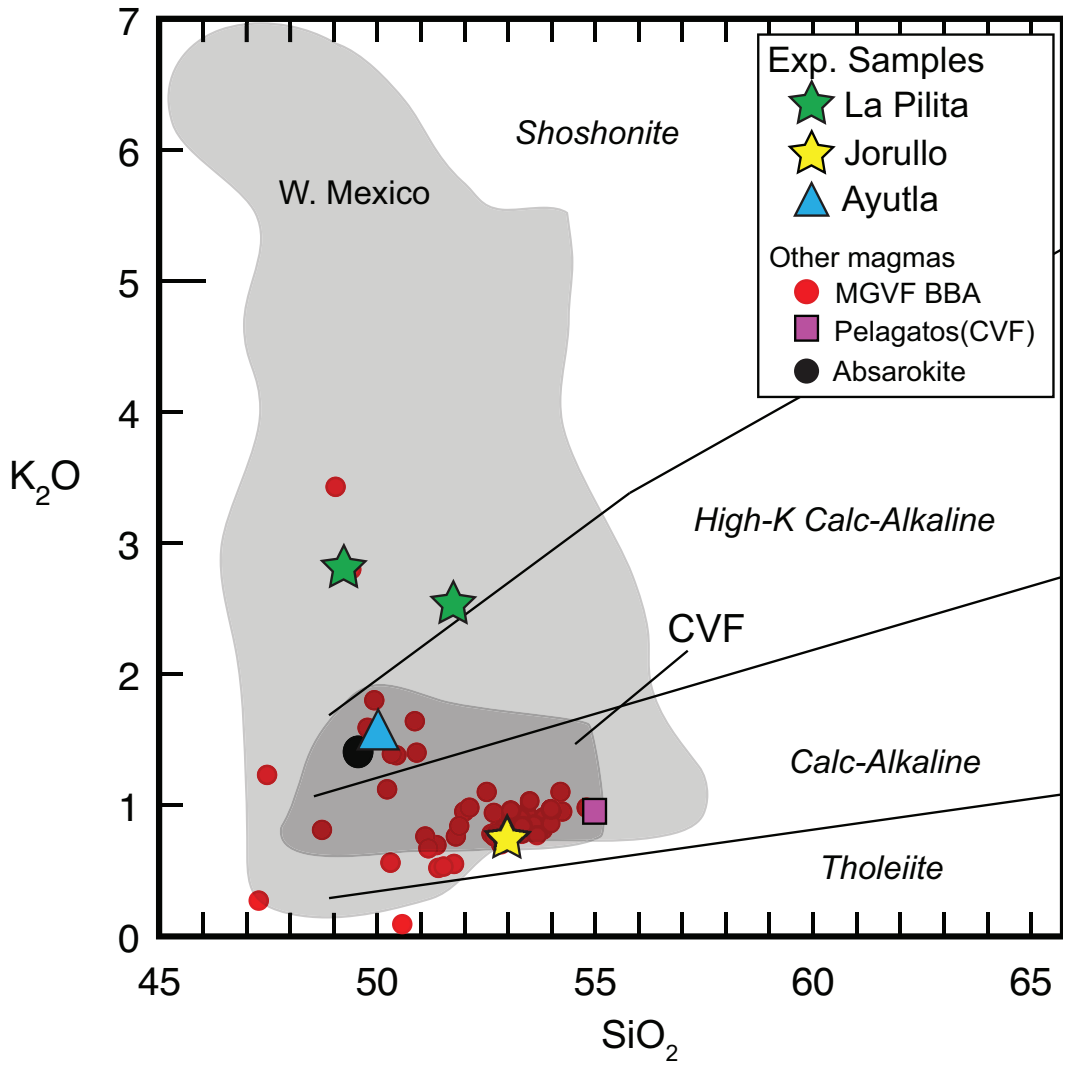

Figure 13. K_2O vs. SiO_2 for primitive (MgO>8 wt%) magmas from western Mexico, MGVF, and CVF. Samples in this work are JOR-46 (green stars, JOR-46d also shown) from La Pilita (Luhr and Carmichael 1985); Blue triangle AY-509 from Ayutla, western Mexico (Righter and Rosas-Elguera 2001). Other samples are JR-28 from Jorullo, MGVF (Luhr and Carmichael 1985) and d-25 from Pelagatos, CVF (Meriggi et al. 2008) whose experimental phase relations were studied by Weaver et al. (2011) and Weber et al. (2011), respectively. Absarokite M.102 from Carmichael et al. (1996). Experimental phase relations of this sample were studied by Hesse and Grove (2003). Whole rock data obtained from Georoc database.

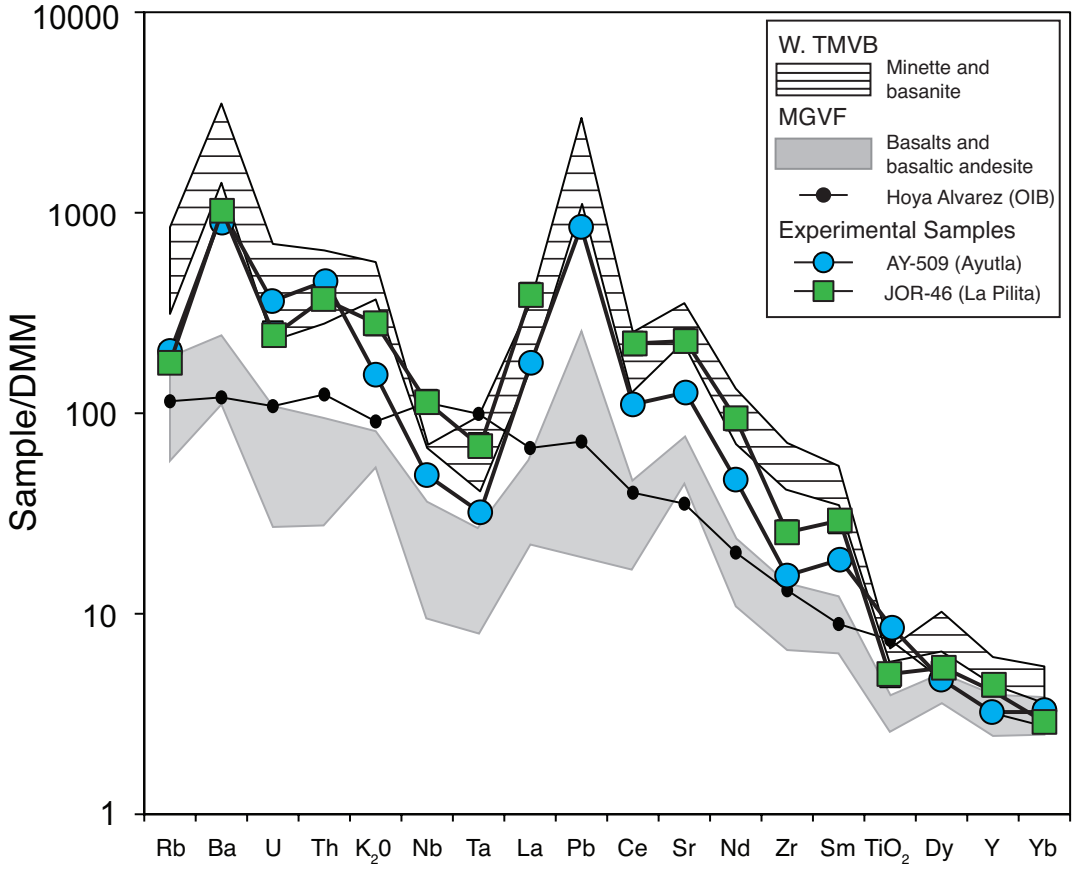

Figure 14. Incompatible trace element concentrations normalized to depleted MORB mantle (DMM, Salters and Stracke [2004]) for primitive melt inclusions from western TMVB minette and basanite (Vigouroux et al. 2008) and basalts and basaltic andesites from MGVF (Johnson et al. 2009). JOR-46 are whole rock data from Luhr and Carmichael (1989). Analyses for AY-509 are from Righter and Rosas-Elguera (2001) and this study. Also shown is a primitive, OIB-type magma from Hoya Alvarez (Johnson et al. 2009).

In general, there are three endmember primitive magma compositions that erupt along the TMVB. Most ubiquitous are the medium-K BBAs that erupt at shields and cinder cones along and behind the volcanic front and differentiates of the BBAs (andesite, dacite, rhyolite) that erupt at major stratovolcanoes. The primitive BBAs commonly show depletions in high field strength elements (HFSE; Ti, Nb, Zr) relative to light rare earth

elements (LREE; La, Ce). They also typically are enriched in volatiles (H_2O, CO_2, Cl) and are moderately elevated in large ion lithophile elements (LILE; K, Sr, Rb, and Ba) (Cervantes and Wallace 2003; Johnson et al. 2009). These patterns are generally interpreted to be a "subduction signature". Analyses of olivine-hosted melt inclusions and experimental evidence provide support that the BBAs are subduction-related magmas produced by fluid or hydrous slab-melt fluxing of a variably depleted mantle source (Johnson et al. 2008; Johnson et al. 2009; Weaver et al. 2011).

In western Mexico there are compositionally distinct potassic (shoshonitic) magmas (minettes, basanites, leucitites) that erupt along the volcanic front within the Jalisco Block. These lavas are highly elevated in LILE, HFSE, and LREE relative to BBAs, but also show the depletion of HFSE relative to LILE and LREE that is characteristic of the BBAs (Figure 14) (Luhr and Carmichael 1981; Allan and Carmichael 1984; Lange and Carmichael 1990). The trace element patterns of western Mexico minette and basanite lavas have previously been interpreted as resulting from deep fluid-flux melting of a metasomatically enriched source that contains garnet and phlogopite (Vigouroux et al. 2008).

A third endmember is intraplate alkaline or OIB-type lavas. These are typically H_2O-poor and do not display the typical "subduction signature" in incompatible trace elements in that they lack the depletion in HFSE relative to LREE and LILE. Primitive melt inclusions from behind the volcanic front at Hoya Alvarez (MGVF) show this geochemical signature (Figure 14). Primitive OIB-type lavas more commonly erupt behind the volcanic front in the back arc (Luhr 1997), but some have erupted at the volcanic front in the CVF (Marquez et al. 1999; Wallace and Carmichael 1999) and the

MGVF (Hasenaka and Carmichael 1987). These OIB-type lavas have been interpreted to be decompression melts of upwelling asthenosphere that has been influenced little (if at all) by a subduction component (Johnson et al. 2009).

Contemporaneous primitive lavas that cover this compositional spectrum and show distinct geochemical signatures are likely evidence of heterogeneous mantle that has been variably affected by depletion during previous partial melting, alteration by a metasomatic agent, and/or enrichment by asthenospheric influx during slab migration. The two compositions in this study are transitional with respect to the subduction-related highly potassic minettes and the alkaline intraplate basalts, so they are important for revealing such compositional heterogeneities in the mantle.

Cerro La Pilita and Volcán Jorullo

The potassic trachybasalt erupted from the Cerro La Pilita cinder cone is compositionally distinct from the BBAs of neighboring Volcán Jorullo. The petrogenic relationship between these two cones has been discussed by Luhr and Carmichael (1985), who state that the drastically different magmas from these cones "cannot be related to one another by any simple mechanism, and must represent fundamentally different partial melting events in the mantle." They argue that the Jorullo magmas likely formed by hydrous partial melting of fertile mantle (lherzolite) but provide little explanation for the origins of La Pilita basalts. Recent work provides evidence that primitive calc-alkaline magma erupted from Jorullo (JR-28) formed by fluid-flux melting (>5.5 wt% H_2O in primitive melt) of depleted mantle (harzburgite) (Johnson et al. 2009; Weaver et al. 2011). Luhr and Carmichael (1985) characterize scoria (JOR-46) and ejected blocks (JOR-46d) from La Pilita (Figure 13). The scoria contains olivine and augite phenocrysts

with primary amphibole, whereas the ejected blocks contain primary biotite. The scoria is more primitive than the blocks, so the high-pressure phase relations of JOR-46, rather than 46d, were investigated for this study. La Pilita lavas show trace element signatures similar to the potassic minettes and basanites of western Mexico. JOR-46 is elevated in LILE and HFSE, but also shows a moderate depletion in HFSE relative to LREE (Figure 14).

Ayutla

The Ayutla volcanic center is characterized by Pliocene-Early Quaternary age alkali basalts, potassic minettes, and calc-alkaline basalts to andesites which are described in detail by Righter and Rosas-Elguera (2001). Our experiments use alkali basalt AY-509 from their study. This sample has been described as an "intraplate alkaline basalt" (total alkalies ~6.5 wt%), but does not exhibit incompatible trace element patterns typical of OIB-like lavas. Instead, AY-509 shows a trace element signature similar to La Pilita lavas. It is elevated in LILE, and shows a moderate depletion of HFSE relative to LREE (Figure 14). The similarity in trace elements to western Mexico minettes suggests that a slab-component may have been involved in its genesis. The trace element pattern for AY-509 indicates that alkaline lavas erupted at the volcanic front are likely transitional and probably had some involvement of a slab component.

Methods

Sample Descriptions

The samples chosen for this study are primitive basalts that likely represent mantle melts that have undergone little to no olivine fractionation upon ascent. La Pilita trachybasalt JOR-46 is relatively oxidized [~NNO+2, where $NiO = Ni + ½ O_2$, (Huebner

and Sato 1970)] and contains phenocrysts of olivine (Fo_{86-88}), augite, and microphenocrysts of plagioclase (Luhr and Carmichael 1985). It is *ne*-normative with primary hornblende and apatite and has elevated Ni (248 ppm) and Cr (338 ppm) (Luhr and Carmichael 1985). Low-pressure experiments of Barclay and Carmichael (2004) reproduced this phenocryst assemblage at 970-1040 °C and 50-150 MPa under H_2O-saturated conditions. The presence of primary amphibole and lack of biotite tightly constrains the crystallization P-T-H_2O conditions and indicate that La Pilita lavas contained at least ~2.5-4.5 wt% H_2O during phenocryst equilibration. Considering their estimates to be minimum values for the initial H_2O content of the magma, we conducted H_2O-undersaturated, high-pressure experiments (1.0-2.0 GPa) with 4–6 wt% H_2O.

Ayutla alkali basalt AY-509 is also silica-undersaturated and contains few olivine phenocrysts (Fo_{88-90}) and microphenocrysts of plagioclase (An_{37-40}). Whole rock analyses show elevated Ni and Cr, at 230 ppm and 370 ppm, respectively and fO_2 estimates are near NNO+1 (Righter and Rosas-Elguera 2001). We conducted experiments with ~1-2 wt% H_2O because of its major element similarity to the OIB-basalts in Mexico. Such melts have been shown to contain pre-eruptive H_2O contents near 1 wt% (Cervantes and Wallace 2003; Johnson et al. 2009).

We obtained these samples as powders and further ground them under ethanol to reduce the size of some larger grains and create homogeneous starting powders for our experiments. Full geochemical data for these samples are provided in Table 1.

Experimental Methods

Fe-presaturation and Prevailing Oxygen Fugacity

The use of AuPd capsules has been shown to minimize hydrogen diffusion and iron dissolution from the starting material to the experimental capsule, though Fe loss continues to be an issue for experiments with primitive, Fe-rich compositions (e.g., Gaetani and Grove 1998; Hall et al. 2004; Kagi et al. 2005). To reduce the tendency for Fe to alloy with the capsules, we preconditioned the AuPd capsules prior to using them in our high-pressure experiments following the procedure of Medard and Grove (2007). The AuPd capsules were packed with an Fe-bearing rock powder, which was fused to glass at 1300 °C in a Deltec 1 atm gas mixing (H_2-CO_2) furnace. The glasses were kept at an oxygen fugacity (fO_2) more reducing than the desired high-pressure experimental fO_2. Had we preconditioned the capsules at the desired fO_2, the capsule would have been in equilibrium with the glass *after* it had lost Fe. The more reducing fO_2 increases the activity of Fe^0, allowing additional Fe to diffuse into the capsule, producing a capsule that is at or near equilibrium with the complete amount of Fe in the starting composition. The glass was dissolved in a warm (50 °C) HF bath for two days in a sealed Teflon digestion bomb. The capsules were cleaned in an ethanol bath and used in piston-cylinder experiments. We attempted to run experiments close to the fO_2 conditions appropriate for the natural assemblage.

Experiments with JOR-46 powder (HTB-*x* series) used capsules that had been preconditioned at 1300 °C and NNO+1 and NNO+1.5. We found that preconditioning at NNO+1 forced excess Fe into the capsules resulting in the experimental glasses gaining Fe from the capsule during the high-pressure experiments. Later experimental capsules

were preconditioned at NNO+1.5 instead to lessen this effect. Similarly, we preconditioned capsules for AY-509 experiments (ALK*x* series) at fO_2 near NNO–NNO+0.5 to approach conditions estimated for this lava.

The post-run Fe contents of the experimental glasses and presaturated capsules were measured and used to calculate the prevailing fO_2 of the high-pressure experiments. While we were able to achieve experimental conditions near the best estimates for the natural assemblages, it was impossible to fully control the experimental fO_2, resulting in some Fe exchange during the duration of the experiment.

Piston-cylinder Experiments

For each experiment, we packed ~20 mg of rock powder into a preconditioned capsule before adding the appropriate amount of distilled H_2O with a 1.0 μL microsyringe to achieve the desired nominal H_2O content. We crimped the capsule, suspended it in an ice bath, and welded it shut with a carbon arc welder. The weights of the capsules pre- and post-welding indicate that no significant H_2O was lost during this procedure. The capsule was loaded into our assembly's off-center hot spot (Pickering et al., 1998) in a pre-drilled crushable MgO pedestal and positioned in a straight-walled graphite furnace. The furnace, in turn, was placed in a pressed and sintered CaF_2 outer sleeve.

We first pressurized the sample at room temperature using a ½ inch end-loaded, solid medium piston-cylinder apparatus before applying power at a ramping rate of 75 °C per minute until the sample was at the target temperature. The temperature was measured using a W-Re_5/W-Re_{26} thermocouple and controlled using a Eurotherm digital controller with an Omega electronic cold-junction compensator. Previous work with our assembly

demonstrates that a capsule in the off-center hot spot is well within 10 °C of the measured thermocouple temperature (Pickering et al. 1998).

Analytical Techniques

We used Fourier transform infrared (FTIR) spectroscopy to analyze the H_2O and CO_2 contents of the experimental glasses. For select experiments, glass chips were prepared as thin, polished wafers, and transmission spectra were collected. Concentrations (C) of volatiles were calculated using the Beer-Lambert equation: $C=MA/\rho d\varepsilon$, where M is the molecular weight of H_2O or CO_2, A is the absorbance of the peak of interest, ρ is the density of the glass, d is the average thickness of the wafer, and ε is the absorption coefficient. We calculated the densities of the experimental glasses using the method of Luhr (2001). H_2O concentrations were calculated from the absorbance of the total OH peak at 3550 cm^{-1}, using an absorption coefficient of 63 L/mol·cm (Dixon et al. 1995). CO_2 was calculated using the carbonate peaks at 1515 and 1435 cm^{-1}, and a corresponding compositionally-dependent absorption coefficient was calculated following Dixon and Pan (1995). Since the background in the region of the carbonate absorption peaks shows complex curvature, we utilized a background-fitting algorithm (S. Newman, unpublished) that subtracts a carbonate-free, basaltic reference spectrum from the observed spectrum to obtain the CO_2 peak heights.

The technique described above is well calibrated and established to be an accurate measure of H_2O contents of basaltic glasses. However, we had difficulty in preparing uniformly thick, polished wafers for all experimental run products, particularly those containing crystals. We therefore used the results from the transmission FTIR analyses to calibrate a reflectance IR relationship appropriate for our basaltic glasses. This technique

uses the negative 3650 cm^{-1} resonance of the reflectance spectrum relative to 3200 cm^{-1} (ΔR_{3650}) normalized to the reflectivity at 4000 cm^{-1} (R_{4000}) (Figure 15a). This ratio ($\Delta R_{3650}/R_{4000}$) is dependent on the H_2O content for a given glass refractive index and glass density (Hervig et al. 2003). This technique has been calibrated in our lab for basaltic andesite and rhyolitic glasses (Johnson et al. 2011; Weaver et al. 2011; Weber et al. 2011). However, given the sensitivity of glass refractive index and density to Fe content, we found the calibrations for rhyolitic and andesitic glasses to be inappropriate for the basaltic glasses used in this study. Accordingly, we used the transmission spectra of the experimental basaltic glasses to calibrate an appropriate reflection $\Delta R_{3650}/R_{4000}$ relationship (Figure 15b). This relationship was then used to measure the H_2O contents of all our experimental hydrous glasses.

Transmission spectra were collected for nine experimental glasses (ranging in H_2O contents from ~1.5-6 wt%) that had little capsule/glass Fe exchange and few to no crystals. The same glasses were analyzed using by reflectance FTIR and the best-fit linear relationship was found to be

$$C\ (H_2O\ wt\%) = 52.7\ (\Delta R_{3650}/R_{4000}) + 0.88;\ r^2 = 0.97$$

The fact that the linear trend does not go through the origin and has a positive y-intercept indicates the minimum detection limit of this technique. Since all the experimental glasses contain >1 wt% H_2O, it is appropriate to apply this relationship to all experimental glasses.

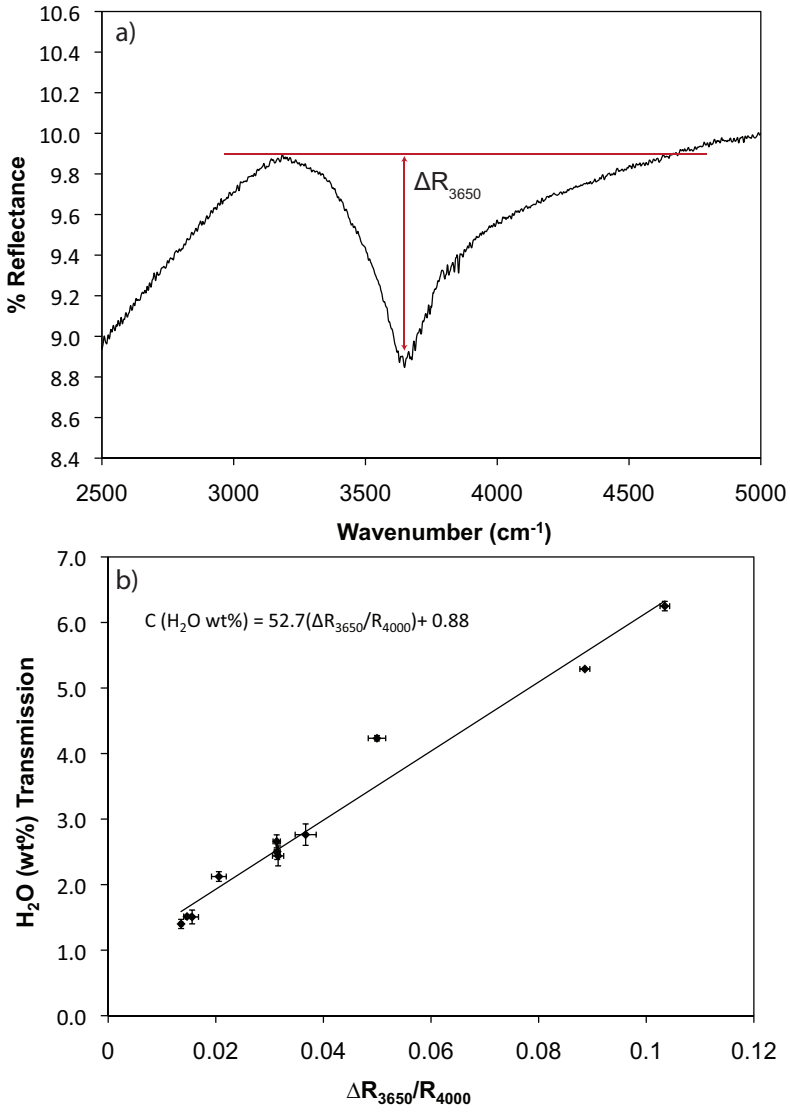

Figure 15. Sample reflectance spectra for an experimental glass with ~6.2 wt% H_2O (a); see text for details; empirical reflectance-transmission relationship using experimental glasses from ALK and HTB experiments (b).

Results

Volatile Contents of Experimental Glasses

The measured H_2O contents for our experimental glasses are near 4–6 wt% in HTB experiments (Appendix C) and 1.5 wt% in ALK experiments (Appendix E). There

is no indication that H_2O was lost during the run durations. We obtained CO_2 measurements for several glass chips that had been prepared for transmission IR. Although no source of CO_2 was added to our starting materials, 2000–5000 ppm CO_2 was measured in these glasses. This is not uncommon; CO_2-free experiments are inherently difficult to perform (e.g., Gaetani and Grove 1998) given the use of carbon based furnace assembly components and a graphite welding rod (G. Moore, personal communication). The presence of CO_2 in the experimental glasses makes them more closely resemble the natural high-pressure melts which contain significant dissolved CO_2 and H_2O (Cervantes and Wallace 2003; Vigouroux et al. 2008; Johnson et al. 2009). Since both species have an effect on olivine and orthopyroxene stability (olivine stability increases relative to orthopyroxene with H_2O, whereas the reverse is true with additional CO_2), the presence of both allows for a more appropriate interpretation of experimental phase relations (Eggler 1974).

Experimental Results for La Pilita (JOR-46)

Phase Relations

Figure 16 shows the H_2O-undersaturated experimental phase relations for JOR-46. Chemical data for equilibrium glasses and crystals can be found in Appendices C-D. At the more hydrous conditions (~6 wt% H_2O), clinopyroxene (cpx) crystallizes on the liquidus at pressures from 1.4-2.3 GPa. The liquidus mineralogy changes to an olivine + clinopyroxene assemblage near 1.4 GPa, which persists at the lower pressures investigated. Two experiments (HTB-14 and HTB-19) were performed at 1.4 GPa and 1160 °C in an effort to constrain the transition from cpx to olivine as primary liquidus phases. Experiment HTB-14 resulted in glass only, whereas HTB-19 crystallized trace

quantities of cpx. The different results of these experiments likely are due to the capsules sitting in different parts of the "hot spot" during the experiment, indicating that the liquidus is near 1160 °C at 1.4 GPa.

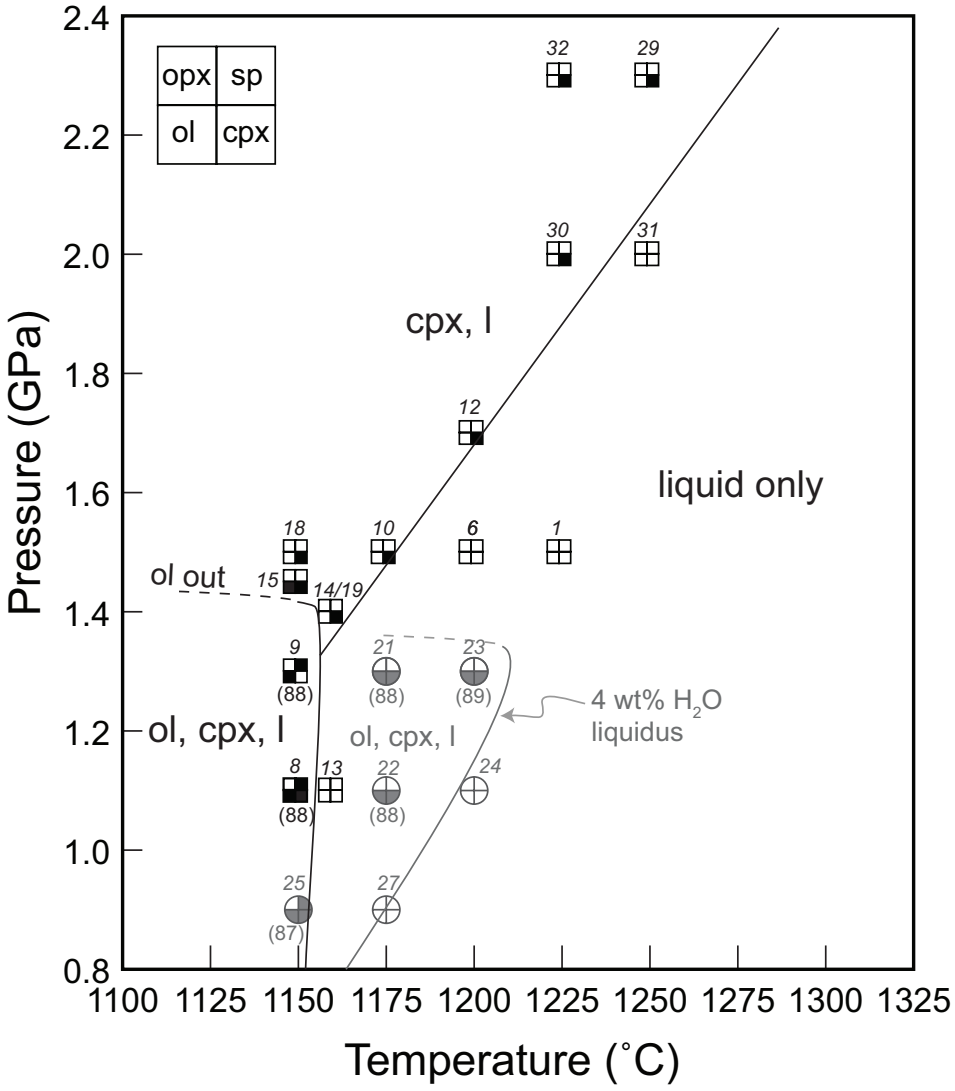

Figure 16. Near-liquidus, hydrous phase relations for JOR-46. Black boxes and liquidus lines are for experiments with 6 wt% H_2O; grey circles and lines are for experiments with 4 wt% H_2O. A filled box/circle indicates the phase is present in the experiment according to the legend in the upper left (opx: orthopyroxene, sp: spinel, cpx: clinopyroxene, ol: olivine). Unfilled symbols indicate glass (liquid) only in the experiment and are used to constrain the liquidus. Numbers in italics above each symbol is the experiment number with prefix HTB. Numbers in parentheses below symbols indicate the forsterite (Fo) content of experimental olivine.

The pressures over which cpx+ol is the liquidus assemblage change little with decreasing H_2O content (Figure 16). However, the assemblage likely transitions to olivine only at pressures <1 GPa. We base this assertion on the proportions of olivine and clinopyroxene crystals in HTB-25. We have observed that crystallinity rapidly increases when clinopyroxene appears whereas the opposite is observed for olivine (see Figure 18). The high proportion of olivine relative to clinopyroxene in HTB-25 at 0.9 GPa indicates that olivine is the likely primary liquidus phase, with cpx appearing ~10-20 °C below the liquidus. However, we were unable to distinguish separate mineral-in curves for these two phases at these P-T conditions.

Compositions and Textures of Crystalline Phases

Clinopyroxene: Some experiments showed patchy, zoned pyroxenes despite long run durations and efforts to grind the rock powder to a fine, homogenous starting mixture (Figure 17a). While the zoning does not change our interpretations of phase relations, it may contribute to poorer mass balance results. In a few experiments (HTB-13-18), we attempted a reversal technique to rehomogonize the samples to glass at 1300 °C for 3 hrs before cooling to their target experimental temperatures and holding them isothermally for 12-24 hrs. The pyroxenes that crystallized in these experiments were also zoned and showed similar textures and compositions to non-homogenized experiments.

Clinopyroxene (augite) phenocrysts in JOR-46 scoria show little compositional variation, with $Wo_{47}En_{45.5}Fs_{7.5}$ cores to $Wo_{46.5}En_{43.1}Fs_{10.4}$ rims (Appendix D). Experimental augites were large, euhedral grains with cores similar in composition to scoria phenocryst rims ($Wo_{46}En_{44}Fs_{10}$). Rim compositions of experimental augites are more Mg-rich and Ca-poor ($Wo_{39-41}En_{48-52}Fs_{9}$) relative to cores, with the most Ca-poor

pyroxene in HTB-23 ($Wo_{36}En_{55}Fs_9$, Appendix D). The large rim volumes relative to cores in the experimental phases indicate an acceptable approach to equilibrium over the run duration. We consider the rim compositions to be representative of the residuum clinopyroxene.

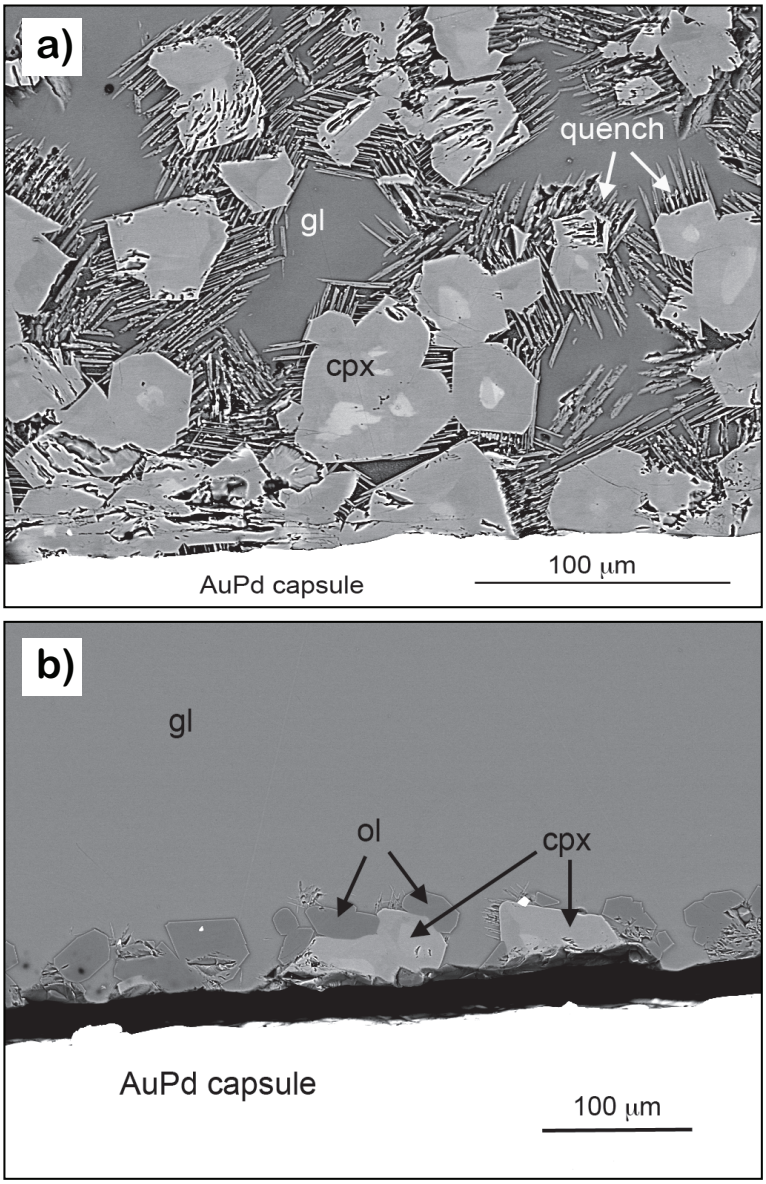

Figure 17. Backscattered SEM image of representative experimental textures. a) HTB-10: patchy zoned clinopyroxene (cpx) crystals with needle-like quench rims; b) HTB-8: near-liquidus experiment with patchy zoned cpx (light gray), unzoned olivine (ol, dark gray), and homogeneous hydrous glass (gl).

Olivine: The most magnesian olivine cores in the natural sample range from Fo_{85-88}. Experimental olivines are unzoned, subhedral to rounded grains with thin Fe-rich rims, likely formed during the quench process (Figure 17b). Their compositions vary slightly depending on the fO_2 of the experiment, but forsterite contents range from 87.6-89.2. Equilibrium K_D values were calculated for olivines using the method of Toplis (2004) at the experimental fO_2 and H_2O contents measured by FTIR. K_D values for olivine range from 0.30-0.31 indicating they have fully equilibrated with the primitive melt under the experimental conditions.

Experimental Results for Ayutla (AY-509)

Phase Relations

The phase relations for AY-509+1.5 wt% H_2O are shown in Figure 18. Olivine is the primary liquidus phase at P<1.8 GPa and is replaced by clinopyroxene (augite) at higher pressures. The melt appears to saturate with augite and olivine near 1.8 GPa and 1275-1300 °C. The liquid does not saturate with orthopyroxene at any of the conditions explored. Subliquidus phase relations show that crystallinity dramatically increases at the onset of clinopyroxene crystallization. Two subliquidus samples ALK-8 (ol only) and ALK-7 (cpx only) are both ~25 °C below the liquidus but ALK-8 contains ~2% crystals, whereas ALK-7 contains ~17% crystals. Significantly, this increase in crystallinity does not appear to change the liquid composition significantly (Appendix E). Therefore, we consider near-liquidus (within 25 °C of the liquidus) phase relations appropriate for interpreting permissible mantle residues.

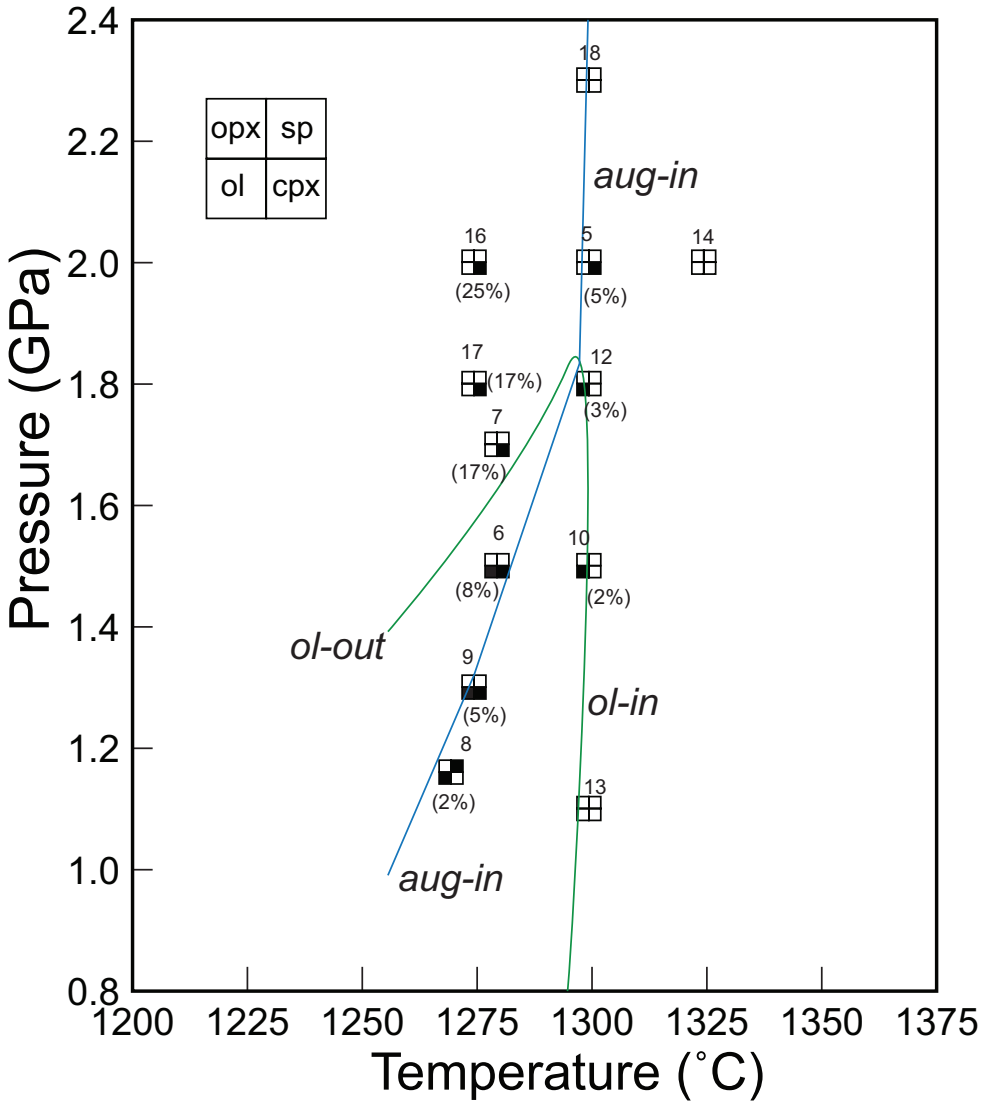

Figure 18. Near-liquidus, hydrous phase relations for AY-509+1.5 wt% H_2O. A filled box/circle indicates the phase is present in the experiment according to the legend in the upper left (opx: orthopyroxene, sp: spinel, cpx: clinopyroxene, ol: olivine). Unfilled symbols indicate glass (liquid) only in the experiment and are used to constrain the liquidus. Numbers above each symbol is the experiment number with prefix ALK. Numbers in parentheses below experiment indicate percent crystallinity. Note the increase in crystallinity when cpx crystallizes.

Compositions and Textures of Crystalline Phases

Clinopyroxene: Near-liquidus clinopyroxenes are generally large, euhedral crystals. They tend to show patchy or concentric zoning with rim compositions of augite ($Wo_{34}En_{53}Fs_{12}$). Experiment ALK7 crystallized patchy, sector zoned augite that varied in its CaO and MgO concentrations. The augite was predominately composed of sectors with the composition $Wo_{36}En_{53}Fs_{11}$ but contained sectors with lower-Ca composition $Wo_{24}En_{65}Fs_{11}$ (Appendix F).

Olivine: Experimental olivines range from $Fo_{87.1\text{-}88.5}$. The textures and sizes are similar to those of HTB experiments: 20 μm–50 μm subhedral crystals with thin Fe-rich quench rims. Complete chemical data for equilibrium crystals are in Appendix F.

Experimental Oxygen Fugacities

The goal of this work was to determine the pressures and temperatures at which these two primitive compositions equilibrated with mantle minerals. Therefore, the compositions of liquidus ferromagnesian minerals must resemble those in the mantle. The prevailing oxygen fugacity (fO_2) controls the redox state of the system, and therefore the Fe^{2+}/Mg ratios of solid solution minerals such as olivine and orthopyroxene. While our attempts to indirectly control fO_2 with the Fe-presaturation technique produced experiments over a range of acceptable fO_2, small deviations from the natural fO_2 affect the compositions of liquidus phases.

We use the empirical method of Weber et al. (2011) and theoretical model of Barr and Grove (2010) to calculate the fO_2 of near-liquidus and superliquidus experimental run products. These methods are based on the temperature- and fO_2-dependent

partitioning of Fe between the capsule and coexisting melt and are appropriate for the melts in this study.

Figure 19 shows the calculated fO_2 at the experimental temperature for super- and near-liquidus experiments. The calculated fO_2 values by both methods were generally within 0.5–1 log units of each other. HTB experiments yielded experimental fO_2 slightly more reducing than the target fO_2 of NNO+2. ALK experiments were 1–2 log units more reducing than the target fO_2 of NNO+1.

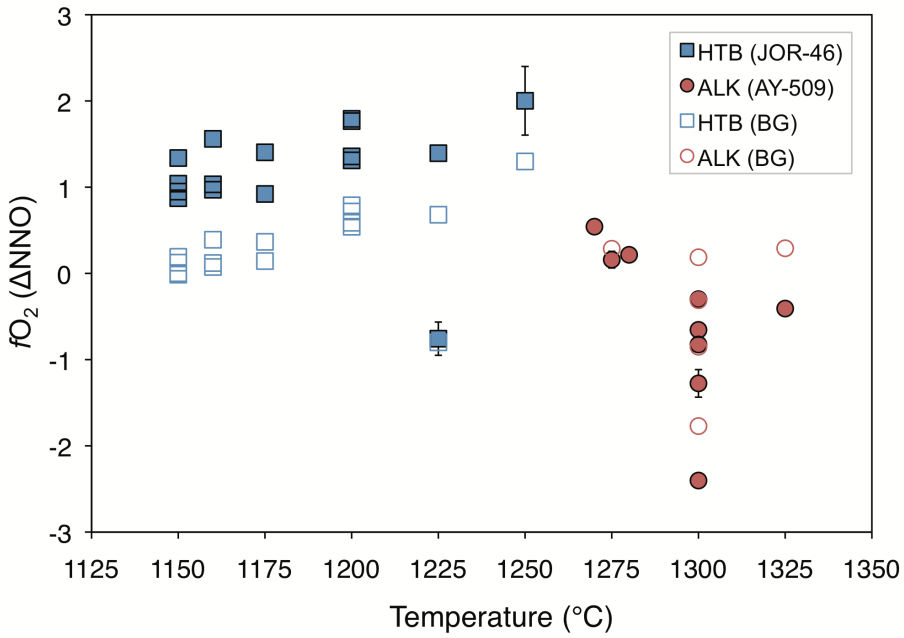

Figure 19. Calculated experimental fO_2 for superliquidus and near-liquidus experiments. Closed symbols utilize the method of Weber et al. (2012), open symbols use the Barr and Grove (BG, 2010) method. Error bars show 1σ standard deviations and may be smaller than the symbol size.

While the experimental fO_2 achieved for all samples are within a reasonable range for subduction zone lavas, deviations from the true equilibrium redox state of the natural system affects the Mg#s [molar Mg/(molar Mg+Fe^{2+})] of crystallizing ferromagnesian phases. The more reducing experimental fO_2 and subsequent Fe-gain experienced by

some of our experimental liquids may result in liquidus olivine that is more Fe-rich than typical mantle olivine (Fo_{87-89} vs. Fo_{90-91}) and shifts the liquidus to slightly lower temperatures (see Figure 6). Previous work has shown that the Fe-exchange does not strongly affect the equilibration pressures (Lee et al. 2009; Weaver et al. 2011).

Interpretation of Experimental Results

Permissible Source Residues

We use the phase relations in Figures 16 and 18 to identify P-T conditions where the hydrous melt is saturated with two or more mantle minerals on its liquidus. These multiple saturation points are interpreted as the P-T-H_2O conditions under which the indicated mineral assemblage would be a permissible residue with the melt. Multiple saturation points are considered to be the final equilibration conditions before segregating from the mantle. The pressures of equilibration are interpreted to be the average depth over which polybaric melts aggregate (Asimow and Longhi 2004) or the depth at which a melt last reequilibrated with wall rocks before its ascent through the crust and eruption.

For JOR-46, we infer that olivine is the sole liquidus phase at lower crustal pressures <1.0 GPa. With increasing pressure, there appears to be a range of P-T-H_2O conditions over which both olivine and clinopyroxene co-saturate on the liquidus. We interpret these phase relations to indicate that JOR-46 melts equilibrated with an olivine+cpx residue at a minimum pressure of 1.0 GPa and a maximum pressure of ~1.4 GPa at temperatures ~1150 °C. This maximum pressure does not appear to decrease with decreasing H_2O (Figure 16). At pressures higher than 1.4 GPa, olivine is no longer stable on the liquidus, and the melt is saturated with cpx only. Of particular note is the lack of liquidus orthopyroxene at any of the P-T-H_2O conditions explored for this melt. The

range of cpx+ol equilibration pressures (1.0–1.4 GPa) can be converted to a depth range of ~35–48 km, respectively, using approximations of crustal density (2800 kg/m^3) and thickness (35 km) for the MGVF (Wallace and Carmichael 1999; Ortega-Gutierrez et al. 2008). This pressure range, therefore, corresponds to the base of the lower crust to the uppermost mantle.

These phase relations differ dramatically from those of primitive melts from nearby Jorullo volcano over the same pressure range. Jorullo basaltic andesite melts equilibrate with olivine+opx (harzburgite) at 42–48 km (1.2–1.4 GPa and 1150–1175 °C with 5–7 wt% H_2O (Weaver et al. 2011). The high H_2O contents are supported by measurements of volatiles in olivine-hosted melt inclusions (Johnson et al. 2008). Studies of this calc-alkaline lava and similar lavas from the Cascades indicate that pervasively depleted peridotite is present in the shallow upper mantle of continental arcs (Baker et al. 1994; Grove et al. 2002). If JOR-46 melts equilibrated at similar depths and temperatures as Jorullo magmas, then a cpx+ol residue would likely exist as an olivine-clinopyroxenite (i.e. wehrlite) vein within a harzburgite host.

Phase relations of AY-509 (Figure 18) are similar to those of JOR-46. A notable difference is the maximum pressure at which the melt saturates with olivine on the liquidus. The olivine stability field extends to 1.8 GPa, where it is replaced by cpx at higher pressure. Orthopyroxene is not a crystallizing phase in any of the experiments with AY-509 at the H_2O-content explored. It was previously assumed that the pre-eruptive H_2O contents for Ayutla lavas were low (Righter and Rosas-Elguera 2001), though we do not have strict constraints on these values. Experimental results for this sample similarly show that wehrlite is a permissible assemblage with 1.5 wt% H_2O, although only one

H_2O-content was explored for this sample. Because we have better experimental constraints on the H_2O contents for JOR-46 and know the low-P phase equilibria, we are able to propose possible conditions for mantle melting, equilibration, and magma ascent for La Pilita lavas.

Mantle Melting and Proposed Ascent Path for La Pilita Magmas

The H_2O-undersaturated phase relations of JOR-46 (Figure 16) are summarized in Figure 20, a projection of the curved H_2O-undersaturated liquidus surface on to the P-T plane, on which we show contours for 4 and 6 wt% total H_2O. Nominally anhydrous phase relations are modeled using pMELTS (Ghiorso et al. 2002) whereas the H_2O-saturated liquidus is constrained by both experiments (Barclay and Carmichael 2004) and pMELTS (Ghiorso and Sack 1995; Asimow and Ghiorso 1998; Newman and Lowenstern 2002). In this projection, melt composition is essentially constant, so intersections of mineral stability surfaces are interpreted as permissible mantle residues and average P-T-H_2O conditions of mantle-melt equilibration (Asimow and Longhi 2004).

Figure 20 also shows the low pressure, H_2O-saturated phase relations of Barclay and Carmichael (2004), which constrain the P-T- H_2O conditions of phenocryst equilibration prior to eruption. Combining these low-pressure phase equilibria with our high-pressure data, we propose the following conditions of mantle equilibration and ascent path of La Pilita primitive magmas. Experiments show that JOR-46 either formed from olivine-clinopyroxenite (wehrlite) in the shallow mantle, or initially formed at some greater depth and ascended to the shallow mantle where it later equilibrated with this assemblage at pressure of 1.3–1.4 GPa (~45 km) near 1200 °C with ~5 wt% H_2O. In a later section we examine trace element patterns to shed light on the depth and source of

melt formation. The hydrous melt then segregated from the ol+cpx residue and ascended adiabatically [4°C/10^8Pa after Barclay and Carmichael (2004) and Annen et al. (2006)].

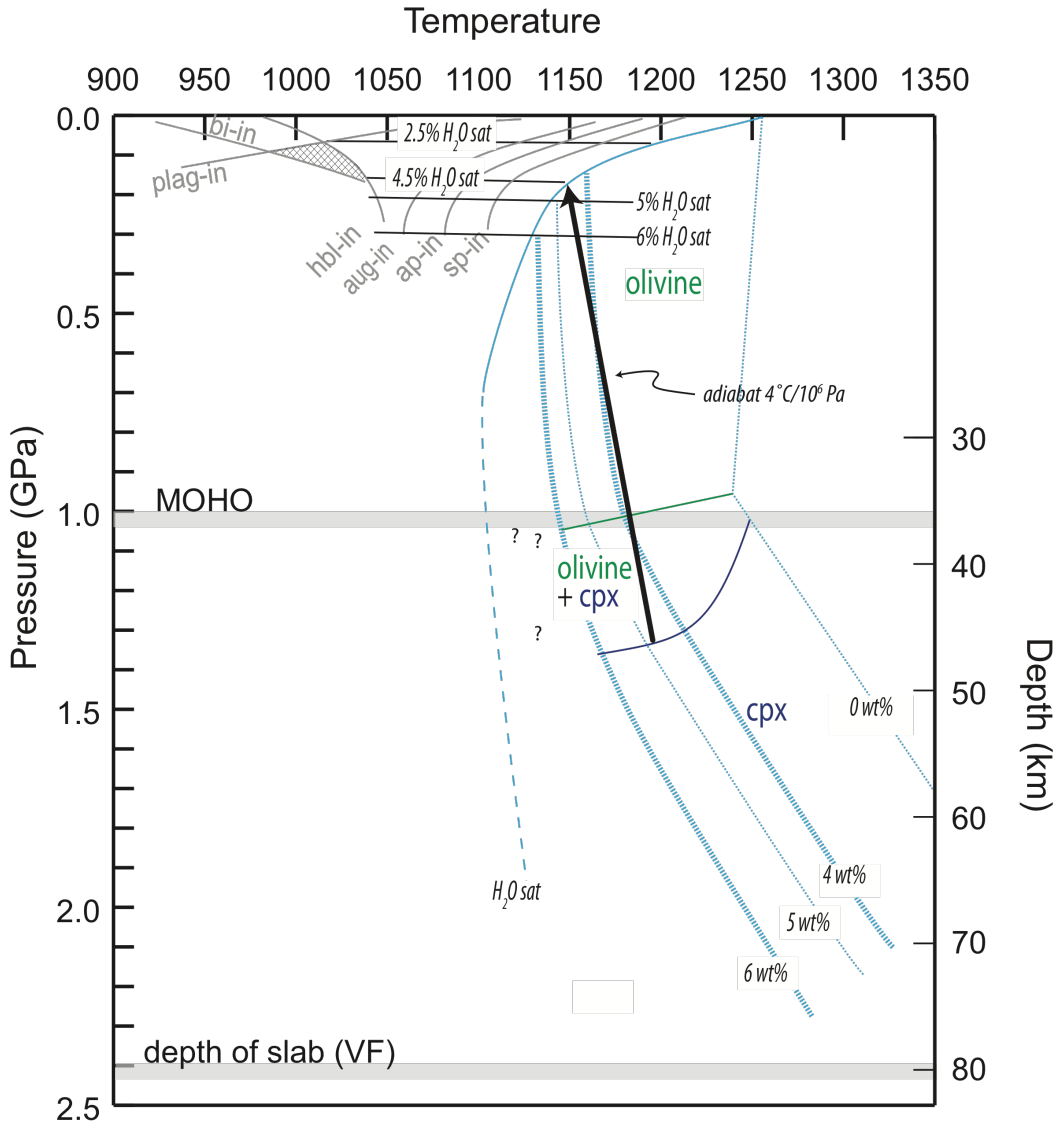

Figure 20. Near-liquidus P-T diagram and possible ascent path for JOR-46. Dashed lines are liquidus lines and are isopleths of constant H_2O. Bold 4 and 6 wt% liquidus lines are experimentally determined, anhydrous liquidus is modeled from pMELTS, 5 wt% is interpolated. At low P the H_2O-saturated phase relations are from Barclay and Carmichael (2002). The Moho and depth to slab are estimated from Wallace and Carmichael (1999) and Pardo and Suarez (1995).

During ascent the melt remained above the 5 wt% H_2O liquidus and resorbed any entrained crystals. The melt reached the 5 wt% H_2O solubility limit near 250 MPa, where

it degassed over a short pressure interval before reaching the H_2O-saturated liquidus near 200 MPa and 1150 °C. At this pressure crystallization of olivine commenced, followed by cooling and crystallization of the remaining phenocrysts. Barclay and Carmichael (2004) suggested that this crystallization process is essentially isobaric, occurring at a depth at which the melt stalls in the upper crust before eruption. Their experiments indicate a small amount of crystallization (~15%) of olivine (ol), spinel (sp), apatite (ap), and augite (aug) occurs over the 100°C temperature interval from 1150 °C–1050 °C, followed by a drastic increase in crystallization once the hornblende (hbl) stability field is reached. Low-P experiments reproduce the phenocryst assemblage and compositions over a narrow P-T-H_2O range, and define a narrow "window of eruptibility" of 50–150 MPa, 1040–940°C, and 2.5–4.5 wt% H_2O. However, crystallinities (>40%) of the experimental run products within this window all exceed that of the natural phenocryst assemblage of JOR-46 (20%). Phase relations at somewhat higher pressures (150–250 MPa) and H_2O contents do show crystallinities more consistent with the natural assemblage; however, distinct hornblende and biotite stability fields are not adequately defined at these pressures. Given the uncertainties among phase boundaries at these higher pressures, it is possible that the phase assemblage (and crystallinity) may be approached at pressures closer to 150–250 MPa with higher H_2O contents. If so, then initial magmatic H_2O contents may be upwards of 6 wt% H_2O. It is important to note that H_2O is assumed to be the only volatile component in both the low- and high-P phase diagrams, despite evidence from olivine-hosted melt inclusions in calc-alkaline and potassic samples that CO_2 is not fully degassed at these pressures (Vigouroux et al. 2008; Johnson et al. 2009). The presence of CO_2 at low P will shift positions of the vapor-saturated and undersaturated

liquidus curves. The effect of CO_2 is not quantified in either the high-P or low-P phase equilibria shown, so presumed pressures of phenocryst equilibration and magma segregation are only estimates.

Discussion

The low-H_2O phase relations for AY-509 permit segregation from a wehrlite residue at depths just above the hottest part of the mantle wedge (~60 km, Ferrari et al., 2011), though it is unknown how the phase relations change with additional H_2O. The trace element signature of this lava suggests that a small slab component may have been involved in its genesis, and that the mantle source was likely similar to an enriched OIB-like or EMORB source. The experimental pressures of equilibration are consistent with the suggestion by Righter and Rosas-Elguera (2001) that magma segregation was deep, but not within the garnet-peridotite stability range. However, we argue that melting was likely influenced by a subduction component and probably was not anhydrous as was previously assumed (Righter and Rosas-Elguera 2001).

The phase relations for JOR-46 also indicate equilibration with a wehrlite residue and do not indicate the presence of residual garnet or phlogopite. However, the steep REE pattern for this sample has been used as evidence that JOR-46 may have segregated from a garnet-bearing source (Figure 14, Luhr and Carmichael 1985). The apparent mismatch between our experimental results and the previously interpreted trace element geochemistry implies perhaps a more complex origin than initially appreciated. In the following discussion we review some relevant experimental studies with primitive potassic lavas and absarokite. In addition, we explore a variety of partial melting models in an attempt to describe the observed trace element patterns of JOR-46 and AY-509.

Near-liquidus Experimental Studies of Potassic Lavas

Generally, petrologic studies of primitive potassic alkaline lavas have been applied to anhydrous, intraplate rifting environments given the rarity of these lavas in active volcanic arcs (Nicholls and Whitford 1983; Conticelli and Peccerillo 1992; Elkins-Tanton and Grove 2003). Although subordinate to calc-alkaline suites, ultrapotassic lavas and absarokite have been observed in continental and intraoceanic arcs both as erupted lavas and as melt inclusions in olivine (Wallace and Carmichael 1989; Lange and Carmichael 1991; Vigouroux et al. 2008). The origins of such lavas have been debated and may involve a combination of melting and/or mixing of metasomatized peridotite (Nicholls and Whitford 1983) and mica-pyroxene veins (Foley 1992; Verma and Hasenaka 2004). Here we review some relevant experimental studies of primitive potassic lavas (from ultrapotassic to absarokite) and assess the similarities and differences to the phase relations of the samples used in this experimental work.

Experimental studies have been conducted on phlogopite-bearing basalts from intraplate environments (Edgar et al. 1980; Arima and Edgar 1983; Nicholls and Whitford 1983; Esperança and Holloway 1987; Elkins-Tanton and Grove 2003), with few dedicated to primitive alkaline basalts in subduction zone settings (Tatsumi and Koyaguchi 1989; Hesse and Grove 2003). Potassic liquids have saturated with peridotite residues (ol+opx±cpx) in near-liquidus experiments (Funk and Luth 2012) but more often are multiply saturated with clinopyroxene, olivine, and phlogopite, and generally lack liquidus orthopyroxene (opx) (Nicholls and Whitford 1983; Esperança and Holloway 1987; Elkins-Tanton and Grove 2003). Several lines of reasoning have been suggested to explain this lack of liquidus opx. Esperança and Holloway (1987) suggest that opx could

be consumed in a melting reaction with phlogopite (phl) where opx + phl ←→ ol + liq (Modreski and Boettcher 1973) if sufficient phlogopite is present in a metasomatized source. Elkins-Tanton and Grove (2003) postulate that an H_2O-rich fluid drives a metasomatic reaction from garnet (gt) lherzolite to mica(phl)-pyroxene peridotite: ol+opx+gt+K_2O rich fluid ⇔ phl + cpx + spinel. Orthopyroxene saturation has been achieved in some melts with additional CO_2 in the fluid phase (e.g., Edgar and Condliffe 1978), but not achieved in others even under CO_2-saturated conditions (Nicholls and Whitford 1983). In all of the studies that lack opx it has been argued that some melt/fluid/rock reaction must be occurring that consumes opx (either by a melting or metasomatic reaction) and produces a residue with phlogopite.

In contrast to the experiments on high-K and ultrapotassic melts, experiments with primitive absarokite do saturate with a peridotite mineral assemblage. In the hydrous (2 wt% H_2O) experiments of Hesse and Grove (2003), an absarokite (K_2O=1.4 wt%, MgO=11.63 wt%, Figure 13) from the Mascota region of western Mexico saturates with olivine+orthopyroxene (with cpx appearing 30 °C below the liquidus) at pressures consistent with the mantle wedge. Phlogopite is not a residual phase in their experiments. In contrast, an absarokite from Katama, SW Japan (K_2O=3.41 wt%, MgO=9.28 wt%) saturates with a phlogopite-lherzolite with ~3 wt% H_2O (Tatsumi and Koyaguchi 1989). It should be noted that compared to average absarokite (K_2O~2.4 wt%, MgO=6.24 wt%; Morrison 1980), the Mascota and Katama samples are both richer in MgO, but the former is poorer in K_2O whereas the latter is richer in K_2O. The samples in our study are intermediate between these two with respect to MgO and K_2O contents.

In light of these petrologic and experimental studies, several mechanisms proposed for origins of potassic alkaline melts have been debated: 1) formation of metasomatized, phlogopite-bearing peridotite by influx of subduction fluids followed by adiabatic decompression melting of the enriched source (Conticelli and Peccerillo 1992; Elkins-Tanton and Grove 2003; Conceicao and Green 2004) 2) initiation of melting by infiltration of asthenospheric melts followed by hybridization of non-peridotite vein melts with peridotite wall rock melts (Foley 1992; Verma and Hasenaka 2004); and 3) dehydration melting of a deep, garnet/phlogopite bearing source (lherzolite or clinopyroxenite) (Esperança and Holloway 1987) with potential further reequilibration with shallow phlogopite lherzolite (Nicholls and Whitford 1983). A suggested origin for the primitive absarokite is fluid-fluxed melting of a phlogopite peridotite followed by shallow equilibration with depleted lherzolite or harzburgite (Hesse and Grove 2003), or partial melting of phlogopite-lherzolite (Tatsumi and Koyaguchi 1989). Thus, the origins of potassic melts are commonly explained though multi-stage processes that generally involve an initial metasomatic enrichment of the mantle source, followed by a melting event and, in some cases, reequilibration at some shallower depth.

Major elements suggest JOR-46 and AY-509 are somewhat transitional between the MgO-rich absarokite of Hesse and Grove (2003) and the potassic melts (Figure 13). Our hydrous phase relations for JOR-46 and AY-509 are similar to those of the potassic melts, with liquidus olivine+cpx and lack of opx. However, our phase relations are dissimilar in the absence of liquidus phlogopite. The lack of liquidus phlogopite suggests that either 1) phlogopite was in the original source (likely as an ol+cpx+phl vein), but was consumed in a melting reaction, or 2) phlogopite was not in the original source and a

slab fluid or melt introduced K_2O and other incompatible elements to an enriched (EMORB or OIB-like) source. In the following sections we integrate our high-pressure phase relations with trace element modeling to propose plausible melting scenarios that may produce the observed lava compositions.

Trace Element Modeling: Further Constraining the Source

In interpreting the near-liquidus mineralogy of a sample, it is important to recognize that it is only representative of permissible residual assemblages at the site of last melt/residue equilibration, but has no 'memory' of the characteristics of the initial, and possibly much deeper, source. However, the trace element characteristics of the final melts have the potential to retain this 'memory'. Incompatible trace element patterns can be used to infer both the geochemistry of the source region and interaction with slab-derived components (fluids or melts). Generally, magmas that show strong depletions in HFSE relative to LILE and LREE (for example, high Ba/Nb or La/Nb) and have elevated volatile concentrations (H_2O, CO_2, Cl, S) are interpreted to have been fluxed with a subduction component such as a slab fluid or melt. Magmas that lack these depletions (such as Hoya Alvarez, Figure 14) indicate melting of an OIB-like, asthenospheric source. The chemistry of the mantle component before any addition of a slab fluid or melt is commonly deduced from enrichments or depletions in conservative elements (Nb, Ti, Dy, Y, Yb). Enrichments in these elements might indicate a low degree partial melt, potentially from an incompatible element-rich mantle source that results from upwelling of fertile asthenosphere (EMORB and OIB-type sources). Strong depletions in HREE (Yb) relative to LREE (La) are one indicator of source garnet (or garnet crystallization/fractionation).

Both AY-509 and JOR-46 show similar trace element behavior to the minettes and basanites of western Mexico, with strong enrichments in LILE and moderate depletions in HFSE relative to LILE and LREE (Figure 14). Relative to the BBA of the MGVF, both samples are elevated in HFSE. These patterns suggest that the melts formed by fluid-fluxed melting of an OIB or EMORB-type mantle source (either garnet- or spinel-lherzolite), yet the phase relations for both samples at all tested H_2O contents do not permit lherzolite as an equilibrium assemblage. Luhr and Carmichael (1985) previously interpreted the steep negatively sloping REE pattern of JOR-46 to indicate melting of a source with residual garnet or crystallization of garnet during differentiation, though the authors highlighted that there was no direct evidence (e.g., modal garnet phenocrysts) to support such a hypothesis. The absence of liquidus garnet for either sample at high pressure indicates that it was not a residual phase during later stage equilibration, but does not preclude garnet as residual during some previous melting event. The apparent mismatch between the trace element patterns and experimental observations implies a more complex origin for these lavas that likely involves interactions among distinct mantle sources (garnet-peridotite and olivine-clinopyroxenite) and a subduction-related component (slab fluid/melt).

To test this possibility and explore potential magmas that may be generated from several mantle components, we investigate trace element patterns that may be produced by initially melting garnet- or spinel-lherzolite by fluxing with a fluid component. In this section we model several melting (+fluxing) scenarios of heterogeneous mantle sources to reconcile the conflicting trace element and experimental interpretations. First, we

discuss how slab surface temperature affects the mobility of certain key trace elements that are commonly used to infer degree of melting or source/slab components.

Effects of Elevated Slab Temperatures on Slab Component Compositions

Trace element concentrations and ratios are often used as proxies for mantle source and slab-derived components of primitive melts. Primitive melts with high La/Yb are interpreted to have formed in the presence of residual garnet, and therefore deep in the mantle wedge (generally >2.5 GPa). Melts with a typical "arc signature" show high Ba/Nb or Ba/La due to the higher fluid mobility of slab-derived, non-conservative LIL elements. However, the stabilities of dehydrating minerals and partitioning behaviors of some incompatible elements are strongly dependent on the thermal state of the downgoing plate (Schmidt and Poli 1998; Hacker et al. 2003b). Specifically, experiments by Kessel et. al (2005) investigating eclogitic assemblages demonstrate that LREE (La, Ce) and some HFSE (Nb, Th, U) become increasingly more soluble in fluids/melts ($D^{fluid/solid}$ increases) at high temperatures and pressure. For example, at 700°C Ba, Rb, Pb, and Sr are fluid mobile, whereas Nb, La, and other REE are retained in the residue. However, as temperature increases to over 800 °C, Nb and light REE become fluid mobile (and are therefore no longer conservative), whereas middle (Dy) and heavy REE (Yb) continue to be held in residual slab eclogite.

The H_2O/Ce geothermometer makes use of these temperature sensitivities and has been used to calculate slab surface temperatures for arcs worldwide (Plank et al. 2009; Cooper et al. 2012). The average H_2O/Ce ratios for hydrous Mexican basalts correspond to slab surface temperatures of 891±69 °C (Cooper et al. 2012). At these temperatures, it is likely that volatiles and slab components would infiltrate the wedge as solute-rich

fluids or slab melts. Moreover, these elevated slab temperatures increase the mobility of HFSE and light REE relative to heavy REE, potentially allowing fluid or melt fluxing to mimic the typical "garnet signature."

Forward Partial Melting Models of Heterogeneous Mantle

To test whether high-T fluids mimic a garnet signature in the compositions that we studied experimentally, we use the high-T experimental fluid compositions of Kessel et al. (2005) to model the trace element signatures that may be imparted onto a partial melt if those fluids flux various mantle lithologies. For simplicity, we will refer to the slab component (SC) as a "fluid" throughout this section, though it is important to note that at 700-900 °C, the subduction component is a solute-rich fluid, whereas at 1000 °C the slab component is a H_2O-rich melt (Kessel at al. 2005). We use the procedure outlined below to answer two questions: 1) What is the effect of slab-temperature on the compositions of melts produced from fluid-fluxed fertile lherzolite if melted in the garnet or spinel stability field? 2) What is the effect of source depletion on fluid-fluxed melts of lherzolite when the underlying slab temperatures are near 900 °C (i.e., the slab component is a solute-rich fluid)? One primary goal of this modeling is to observe if melting fertile or depleted spinel (sp) lherzolite mimics the trace element pattern of garnet (gt) peridotite melting if the sp-lherzolite is fluxed with a high-temperature fluid carrying a garnet signature from the slab.

To address the first question, we first model partial melting of enriched, fertile lherzolite in both the spinel and garnet stability fields. The first step of the modeling procedure is to choose an appropriate starting source composition. We utilize previous work by Johnson et al. (2009) to calculate a hypothetical OIB mantle source that is

appropriate for the region. The OIB-type melt from Hoya Alvarez (Figure 14) shows enrichments in HFSE but no evidence of involvement of a slab fluid, so it can be used as an approximation of a melt derived from unfluxed garnet peridotite. We follow their approach and assume Hoya Alvarez is a 5% batch melt of garnet lherzolite with the modal mineralogy ol(62) + opx(26) + cpx(11) + gt (2) to back-calculate a starting OIB-source composition (*HA-OIB*) (Table 3). We then model partial melts of this *HA-OIB* source (unfluxed) by assuming batch melting in either the spinel [*HA-OIB (sp*)] or garnet [*HA-OIB (gt*)] stability fields. These models will serve as a baseline for observing trends associated with the addition of various temperature fluids (Figure 21), or the depletion of peridotite by previous melt extraction (PME; Figure 22).

The second step is to modify the HA-OIB source by fluxing it with high-temperature fluids. To do this, we modify the original source (C^0) by adding a fraction (X) of a high-temperature fluid (referred to as the subduction component [*SC*]). We use the experimental fluid compositions of Kessel et al. (2005) and calculate the concentration of each element (i) in the modified source (C^M):

$$C_i^M = C_i^{SC} X_{sc} + C_i^0 (1 - X).$$

The final modeling step is to model batch partial melting of the modified source in both the spinel and garnet stability fields. We calculate bulk partition coefficients (D_i) using the assumed modal mineralogy for each source (Table 3). For simplicity, we assume a constant bulk D_i throughout the melting routine.

Table 3. Partition coefficients and starting OIB source used in trace element modeling

Mineral-melt partition coefficients used in trace element modeling

	Ol	opx	cpx	sp	gt
Rb (ppm)	0.00001	0.0001	0.002	0.002	
Ba	0.0003	0.0001	0.00068	0.0005	
U	0.00002	0.0002	0.0038	0.01	
Th	0.00005	0.0001	0.013	0.01	0.0006
K_2O wt%	0.00006	0.0001	0.0072	0.001	0.05
Nb	0.00004	0.002	0.0077	0.4	
La	0.00003	0.00005	0.054	0.003	
Ce	0.0001	0.0002	0.09	0.003	0.01
Sr	0.0015	0.0005	0.13	0.1	0.006
Nd	0.0004	0.0005	0.15	0.005	0.071
Zr	0.0007	0.014	0.123	0.4	0.47
Sm	0.001	0.0015	0.25	0.0075	0.34
Na_2O wt%	0.001	0.0015	0.25	0.0075	
TiO_2 wt%	0.032	0.215	0.358	0.167	0.28
Dy	0.001	0.008	0.4	0.008	3.2
Y	0.01	0.01	0.4	0.023	4.1
Yb	0.024	0.038	0.22	0.007	7.4

All partition coefficients are from Eiler et al. (2005) as reported by Johnson et al. (2009)

Bulk partition coefficients and starting OIB source

For garnet(gt)/spinel(sp) lherzolite: assumed mineralogy 61% ol, 26% opx, 11% cpx, 2% gt/sp
For clinopyroxenite (cpx) vein: assumed mineralogy is 50% cpx, 50% ol
** HA-OIB calculated assuming Hoya Alvarez is a 5% partial melt generated in the garnet stability field*

	Bulk Partition Coefficients			Starting Model OIB Source
	Bulk D (gt)	Bulk D (sp)	Bulk D (cpx)	HA-OIB*
Rb (ppm)	0.00025	0.00029	0.0010	0.51
Ba	0.00028	0.00029	0.00049	7.24
U	0.00048	0.00068	0.0019	0.03
Th	0.0015	0.0017	0.0065	0.09
K_2O wt%	0.0019	0.00087	0.0036	0.05
Nb	0.0014	0.0094	0.0039	1.22
La	0.0060	0.0060	0.027	0.87
Ce	0.010	0.010	0.045	1.85
Sr	0.015	0.017	0.066	22.45
Nd	0.018	0.017	0.075	0.97
Zr	0.027	0.026	0.062	7.87
Sm	0.035	0.029	0.13	0.20
Na_2O wt%	0.029	0.029	0.13	0.20
TiO_2 wt%	0.12	0.12	0.20	0.33
Dy	0.11	0.047	0.20	0.39
Y	0.13	0.053	0.21	2.31
Yb	0.20	0.049	0.12	0.26

Effect of High-T Fluids on Lherzolite Partial Melts

The effects of slab fluids of varying temperatures are shown in Figure 21. The black curves show baseline, unfluxed partial melts of HA-OIB in the spinel (open triangles) and garnet (open squares) fields for F=0.03, 0.05, 0.10, and 0.15. These sources were then modified with 2% addition of the 700, 800, 900, and 1000 ºC fluids and partially melted at the same F values. The resulting melting curves are shown in Figure 21 alongside JOR-46, AY-509, and primitive potassic (MgO>8 wt%, K_2O>2 wt%) lavas from western Mexico (Colima, Jalisco, Mascota).

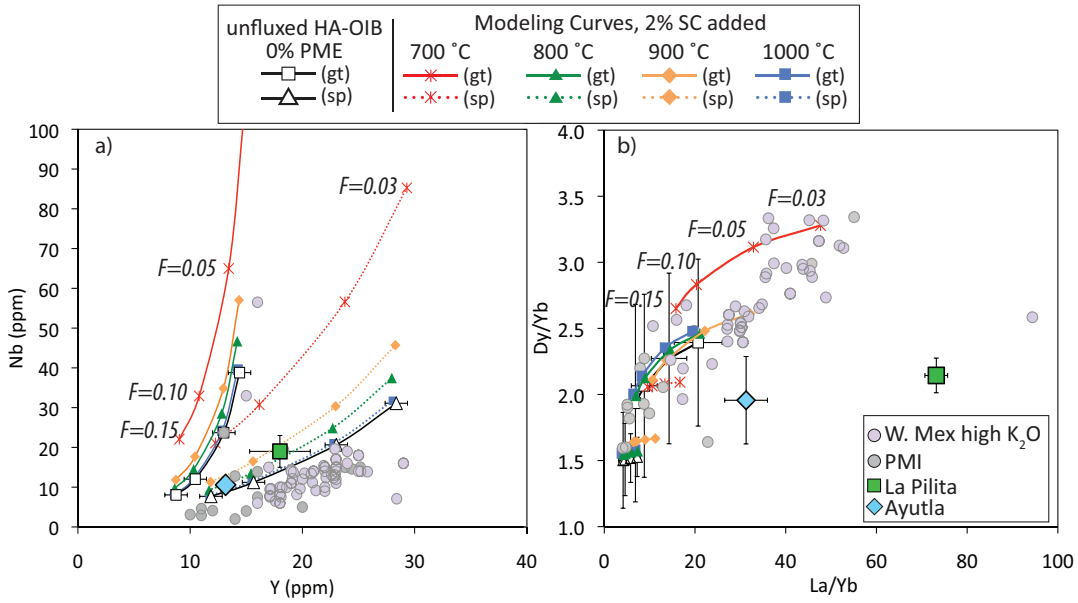

Figure 21. Effect of high-T fluid on (a) Nb vs. Y and (b) REE Dy/Yb vs La/Yb for partial melts of an OIB source in the spinel(sp) and garnet (gt) stability fields when fluxed with various temperature fluids of Kessel et al. 2005. HA-OIB source is calculated assuming alkaline lava Hoya Alvarez (HA) is a 5% partial melt (see text for discussion). Error bars for unfluxed HA-OIB show the propagation of 1σ s.d. of the average HA melt inclusion compositions and can be applied to all other melting curves. We have not considered the error associated with partition coefficients of Kessel liquids. Experimental samples are averages and show 1σ s.d. error bars. Dashed lines indicate melting in the spinel field, solid lines indicate melting in the garnet field. All lines show melt fractions (F) of 0.03, 0.05, 0.10 and 0.15. Primitive melt inclusions (PMI) are for minette, basanites, and calc-alkaline basalts of Vigouroux et al. (2008) and Johnson et al. (2009).

It is apparent that addition of a 700 °C fluid does not significantly change the melt compositions, whereas addition of an 800-1000 °C fluid does move the melt composition towards higher Nb while Y remains unaffected. The western Mexico potassic lavas (shaded circles) were previously interpreted to have formed with residual garnet and phlogopite (Vigouroux et al., 2008). The observed Nb depletions of these lavas may be due to residual phlogopite, which as been shown to retain Nb (Latourrette et al. 1995), but this effect has not been include in our model calculations. From Figure 21a, JOR-26 and AY-509 could be interpreted to be partial melts of HA-OIB that melted in the spinel stability field after having been fluxed with ~2% of an 800-900 °C subduction fluid.

A means of assessing whether high-T fluids can mimic a "garnet signature" is to plot ratios of LREE/HREE (La/Yb) against MREE/HREE (Dy/Yb) (Figure 21b). Though both of these ratios are influenced by residual garnet, a high-T fluid influences the former because D_{La}/D_{Yb} increases dramatically with temperature, whereas D_{Dy}/D_{Yb} remains relatively constant. Figure 21b shows the same baseline melting curves for unfluxed HA-OIB in spinel (sp) and garnet (gt). It is apparent that unfluxed HA-OIB(sp) will not fractionate either Dy/Yb or La/Yb in any significant way, whereas HA-OIB(gt) partial melts become strongly depleted in La/Yb at high melt fractions. Melts from the HA-OIB(sp) source that has been fluxed with 700-900 °C fluids also do not change significantly; however, melts that result from fluxing of a 1000 °C slab melt (red dashed curve, Figure 21b) do become sufficiently elevated in Dy/Yb and La/Yb to mimic an HA-OIB(gt) partial melt. HA-OIB(gt) partial melts become significantly enriched in La/Yb and Dy/Yb with the addition of 800 and 900 °C fluids.

The primitive potassic western Mexico lavas generally fall along the high-T fluid fluxed melting curves of HA-OIB(gt) (solid curves) in Figure 21b. JOR-46 and AY-509 are highly enriched in La/Yb and do not fall along any of the modeled curves at F>0.03. Very low degree melts (F<0.03, not shown) of fluxed HA-OIB(gt) would produce high enough La/Yb values but would then be too enriched in Dy/Yb to reproduce either composition. Alternately, small degree melts of unfluxed HA-OIB(gt) would produce acceptable Dy/Yb values but would be deficient in La/Yb. Only a very low degree melt (0<F<0.01, not shown) of HA-OIB(sp) fluxed with a slab fluid (1000 °C) will contain high enough La/Yb to reproduce JOR-46 and AY-509, but those melts would not contain high enough Dy/Yb values. The experimental samples do not lie along any obvious mixing line among HA-OIB(sp) and HA-OIB(gt) sources.

Effect of Previous Melt Extraction on Fluid-fluxed Lherzolite Partial Melts

In the previous models, we used the *HA-OIB* source assuming fertile mantle composition. In Figure 22 we show what effect source depletion by previous melt extraction (PME) would have on the trace element behavior. These models use as starting compositions *HA-OIB* that has been depleted by 1, 3, and 10% PME in the garnet stability field. The OIB+PME sources are shown and annotated in Figure 22. Johnson et al. (2009) followed a modified version of the inverse modeling technique of Portnyagin et al. (2007) to calculate these depleted sources (for details of this modeling procedure, we refer you to the original references). We subsequently fluxed each variably depleted source with 2% of a 900 °C fluid and modeled batch melting in either the garnet or spinel stability fields. The goal of modeling fluxed melting of OIB+PME sources is to observe

whether trace element behaviors are significantly affected by the choice of starting mantle composition if the fluid composition remains constant.

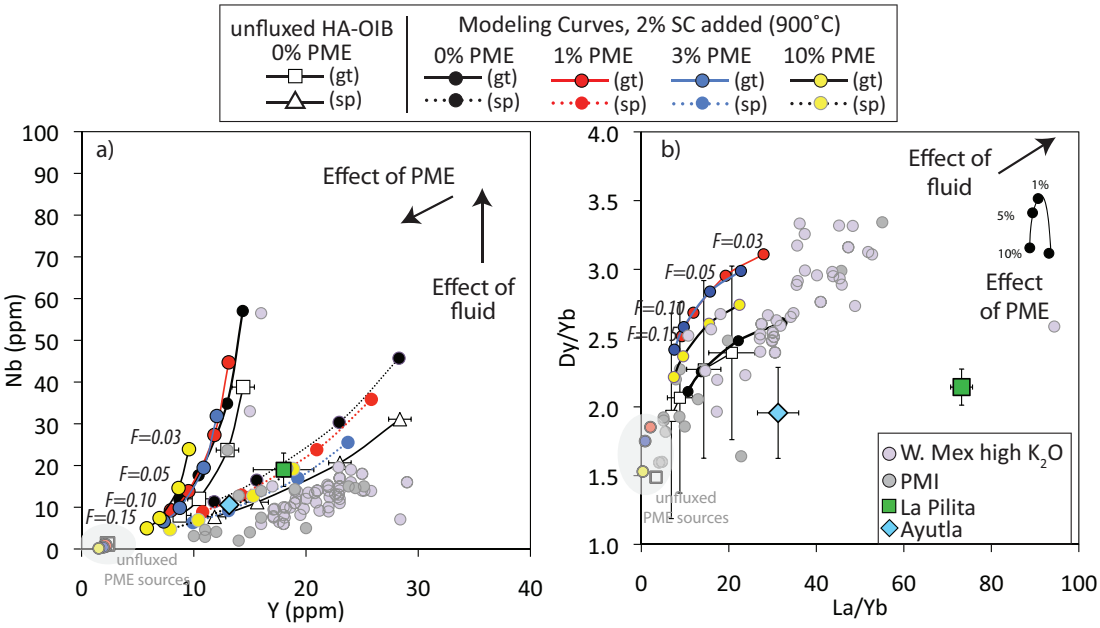

Figure 22. Effect of PME on (a) Nb vs. Y and (b) REE Dy/Yb vs La/Yb for partial melts of variably depleted OIB sources in the spinel (sp) and garnet (gt) stability fields when fluxed with 2% the 900 °C fluid of Kessel et al. (2005). Dashed lines indicate melting in the spinel field; solid lines indicate melting in the garnet field. Partial melting of unfluxed HA-OIB sources in the spinel and garnet stability fields are shown in a), with only garnet shown in b). All other symbols are the same as Figure 21.

The effect of source depletion by PME in the garnet field is to decrease the Nb and Y (Figure 22a). The combined effects of fluid addition and PME cause partial melts to first decrease in Nb and Y ("Effect of PME", Figure 22a), followed by an increase in Nb while Y remains unchanged ("Effect of fluid"). Figure 22b shows the effects of PME and fluid addition on REE patterns for the garnet stability field only. Sources with small PME that have been enriched by a fluid show the highest enrichments in Dy/Yb and La/Yb. Fluxed melts resemble unfluxed HA-OIB melts as the source becomes more depleted.

The modeled melting curves generally reproduce the array of high-K_2O melts of western Mexico. However, it is apparent that none of the melting scenarios explored by changing PME, fluid temperature, or melting depth (gt vs. sp) adequately describe the patterns of JOR-46 or AY-509. We take this as evidence that neither sample originated from garnet- or spinel-bearing lherzolite. Because our experimental phase relations indicate a garnet-free, olivine-clinopyroxene residue, we will explore the possibility that the original source was an ol-cpx vein, rather than lherzolite. To test this, we model batch partial melting using non-peridotite vein lithologies as a potential source component.

Modeling Melting of Minette Veins

Major and trace element diagrams such as Figure 13 and Figure 14 suggest that JOR-46 and AY-509 are intermediate in composition between two endmembers: minette from an enriched source and calc-alkaline basalt from a more depleted source. The previous models show that the two endmember lavas can be produced by garnet and spinel lherzolite melting. However, neither sample lies along any obvious melting or mixing curve, suggesting that they instead may be a product of vein melting.

It is likely that some minette magmas solidify within the uppermost mantle to form veins of ol+cpx+phl. Pervasive vein melting due to a lower solidus temperature would eventually remove phlogopite from the residue, leaving ol+cpx. We investigate the potential that JOR-46 and AY-509 are such melts by modeling partial melting of these veins. We chose several minette lavas that range in their enrichment as the starting sources and calculate partition coefficients consistent with a 50/50 cpx/ol modal mineralogy. Figure 23 shows the melting curves at F=0.05, 0.10, 0.25, 0.50, and 1.0 using four primitive potassic lavas as starting vein sources (Luhr et al. 1989; Maria and

Luhr 2008; Mori et al. 2009). The modal mineralogy allows for a melting trajectory that extends to lower La/Yb and higher Dy/Yb as *F* increases and adequately reproduces the signatures of JOR-46 and AY-509 at melt fractions between 0.05-0.1 (Figure 23b). Figure 23b suggests that a minette veins with the assumed mineralogy would produce melts over a range of *F* that are more enriched in La/Yb than those produced by OIB-type sources. However, the melting trajectories observed in Figure 23a require that very high degrees of melting are needed to produce Y values consistent with those of JOR-46 and AY-509. Although we cannot reconcile this disagreement in *F* values by any simple mixing process with the source components we have tested, we have shown that melting of a metasomatized vein chiefly composed of olivine+clinopyroxene can reproduce the rather unusual REE patterns.

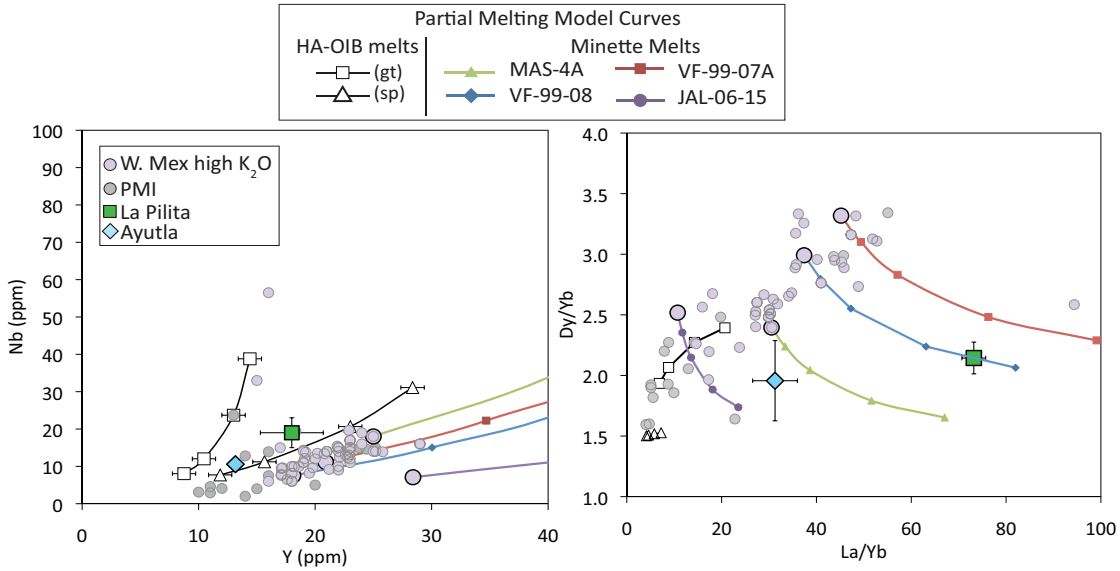

Figure 23. Effect of partial melting of minette veins on (a) Nb vs. Y and (b) REE Dy/Yb vs La/Yb. Melt fractions are plotted as F=0.05, 0.10, 0.25, 0.50, and 1.0 (back to source). Samples used as sources are MAS-4A (Luhr et al. 1997), VF-99-08 and VF-99-07A (Maria and Luhr 2008), and JAL-06-15 (Mori et al. 2009). Also plotted are unfluxed partial melts of HA-OIB(sp/gt) for comparison.

Another possible source component not explored here is one that contains hornblende. Similar to garnet, hornblende retains heavy REE (Bottazzi et al. 1999), and models that mix hornblendite melts with peridotite melts have been shown to produce melting/mixing trajectories similar to those shown in Figure 23b (e.g., Ma et al. 2011). Although hornblende was not a residual phase in our experiments, it is possible that it may have been involved in the initial melting process at depth, but not in later stage shallow reequilibration. Additional models that explore multi-stage melting and/or mixing of many sources (peridotite, hornblende pyroxenite, fluids) may satisfy both trace element signatures and experimental observations and certainly warrant further investigation.

Mantle Heterogeneity in the Trans-Mexican Volcanic Belt

The wide range of primitive alkaline magma composition erupted along the volcanic front in the Trans-Mexican Volcanic Belt indicates that magma genesis and mantle equilibration are complex processes that likely involve interactions among heterogeneous mantle components and complex slab-derived fluids or melts. Calc-alkaline lavas with typical "arc" signature are ubiquitous along the volcanic front both in central and western Mexico. Subordinate to these lavas, but present at the volcanic front are potassic basalts and lower K_2O alkaline basalts (both with subduction trace element signatures) that indicate heterogeneous mantle sources. Volatile analyses, coupled with major and trace element patterns from olivine-hosted melt inclusions are useful for inferring source components of primitive lavas. Near-liquidus experiments, such as those conducted here, are an additional tool to characterize the potential source mantle mineralogy.

The experimental results presented here constrain the source residues for two transitional alkaline lavas that have erupted at the volcanic front. The basalt from Ayutla, western Mexico (AY-509) and trachybasalt from La Pilita (JOR-46) appear to have equilibrated with olivine-clinopyroxenite at 1.7-1.8 GPa and 1.4 GPa, respectively. Ayutla lavas are presumed to have contained some, but low magmatic H_2O (~1.5 wt%), whereas La Pilita lavas are estimated to contain 4-6 wt% magmatic H_2O. Based on incompatible trace element data, it was previously suggested that AY-509 is an anhydrous, small-degree melt of an enriched (EMORB, OIB) mantle source resulting from hot, upwelling asthenosphere in the subarc mantle wedge (Righter and Rosas-Elguera 2001). Primary and parental magmas derived from such enriched mantle sources would have higher conservative element concentrations relative to those derived from more depleted sources. However, new trace element analyses presented here suggest involvement of some slab component during melting. Experiments with ~1.5 wt% H_2O do not indicate that AY-509 equilibrated with garnet- or spinel-lherzolite, and instead indicate equilibration with wehrlite. Trace element modeling and experimental observations further support that the magma is unlikely to be a direct product of lherzolite melting and that many sources, including non-peridotite veins were likely involved.

Experiments and trace element characteristics of JOR-46, a trachybasalt from Cerro La Pilita, just south of Jorullo, indicates a similarly complex origin that likely includes melting of olivine-pyroxenite (and possibly hornblende) and potential mixing with a slab fluid. Previous melt inclusion and experimental studies of the nearby Jorullo lavas show a typical “subduction signature” and indicate fluid-fluxed melting of a depleted mantle (harzburgite) source. Given that Jorullo and La Pilita are a mere 3 km

away from each other, we take this as evidence that the shallow upper mantle is notably heterogeneous. It is possible that in regions where subduction fluid-fluxed forearc has been dragged by mantle flow (as is hypothesized to be the case in western Mexico) after slab repositioning, melting of the vein component and subsequent eruption of potassic magma may be more common. Magmas with this composition are rather uncommon at the volcanic front, except in western Mexico where more highly potassic minettes have erupted. It is possible that in the case of Central Mexico, either forearc has been thermally eroded away so veined sources are rare, or that high heat flux allows pervasive mixing of wall rock and veined sources. These processes may not be unique to Mexico, and perhaps can be applied to other arcs that have complex slab histories and high heat flux.

CHAPTER V

SUMMARY: INTEGRATING PETROLOGIC MODELS WITH EXPERIMENTAL RESULTS

Equilibration Pressures of Primitive Magmas of the TMVB

In this work I have determined pressures and temperatures of equilibration for three primitive lavas in the TMVB that range in their SiO_2, K_2O, and magmatic H_2O contents. The residual mineralogy for these three samples has included harzburgite (JR-28, Jorullo) and olivine-clinopyroxenite (JOR-46, La Pilita and AY-509, Ayutla). Experimentally derived equilibration pressures for these primitive magmas ranged from 1.2-1.8 GPa, with the lowest pressures, and thus shallowest depth) observed in Jorullo magmas and the highest pressures observed for the alkaline basalt from Ayutla. The experimental results here can be combined with those of two other published experimental studies on primitive Mexican lavas to provide an along-arc profile of magma-melt equilibration within the subarc mantle wedge (Figure 24).

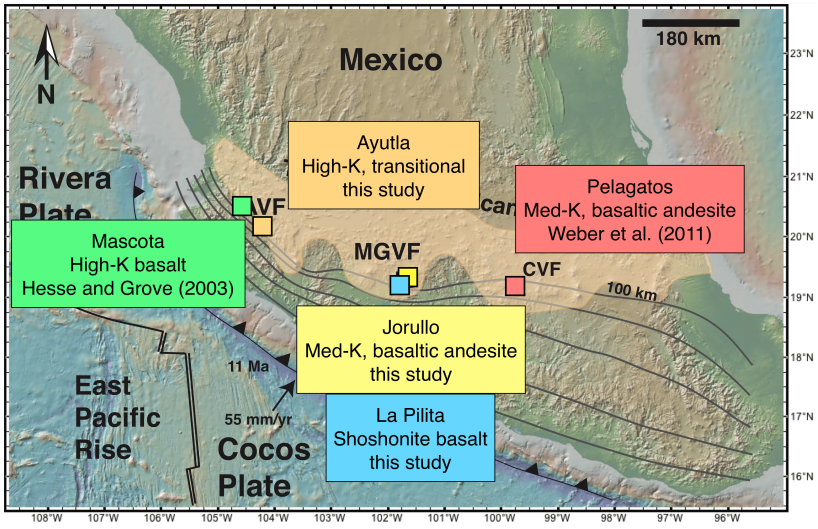

Figure 24. Sample locations for five primitive lavas used in experimental studies. Contours are in 20 km intervals and indicate depth to the top of the slab. The Trans-Mexican Volcanic Belt is in the tan shaded region.

Hydrous, high-pressure phase relations for a high-Mg andesite from Pelagatos (CVF) and primitive absarokite from Mascota (Jalisco) indicate equilibration with harzburgite at ~1.3 GPa and 1.6 GPa, respectively (Hesse and Grove 2003; Weber et al. 2011). Figure 25 summarizes the melt equilibration pressures from the western TMVB toward the central TMVB as found experimentally. In the case of the high-Mg andesite from the Chichinautzin Volcanic Field (CVF) used in Weber et al. (2011), the experimentally determined equilibration pressure was found to be near 1.0 GPa with 5 wt% H_2O. After determining the refractory nature of the mantle source and accounting for possible olivine fractionation, the authors correct this pressure to be in equilibrium with Fo_{92} (rather than Fo_{90}) using a predictive thermobarometer of Lee et al. (2009). This corrected pressure (~1.3 GPa) is plotted in Figure 25.

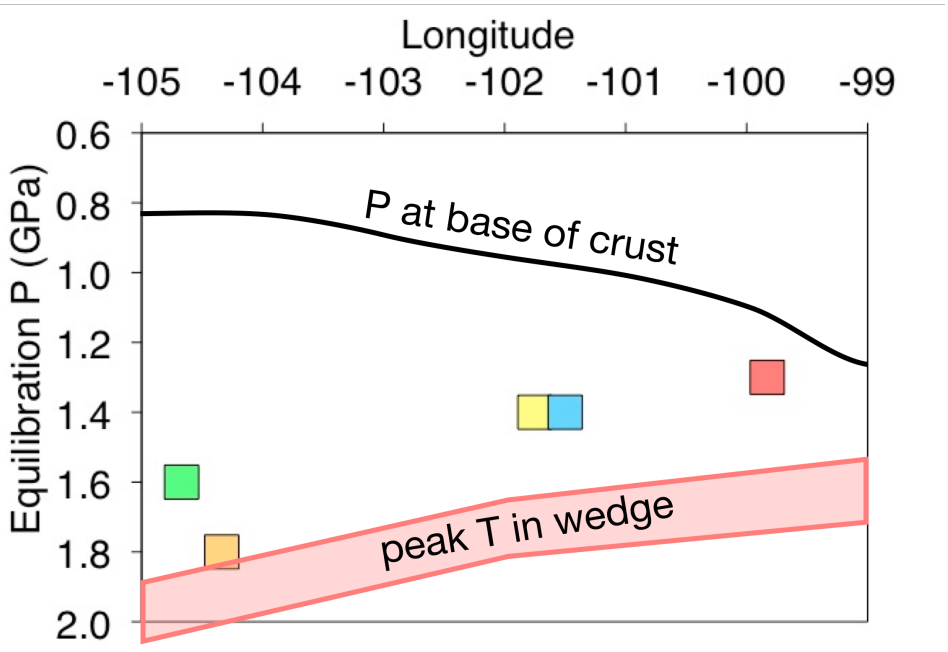

Figure 25. Experimentally determined melt equilibration pressures vs. west longitude. Samples and colors are the same as Figure 24. Solid line indicates the pressure at the base of the crust based on estimated crustal thicknesses (Wallace and Carmichael 1999). Red shaded band indicates the "hot nose" of the mantle wedge (Johnson et al. 2009, Ferrari et al. 2011).

Also plotted in Figure 25 are estimated pressures at the base of the crust (Wallace and Carmichael 1999) and pressures at which geophysical models predict peak mantle wedge temperatures (i.e., the "hot nose") (Johnson et al. 2009; Ferrari et al. 2012). The pressures at the base of the crust along the arc were estimated using crustal thicknesses of Wallace and Carmichael (1999, and references therein) assuming an average crustal density of 2800 kg/m^3. The pressures at the peak mantle wedge temperatures were estimated using the crustal thickness of the region and a mantle density of 3300 kg/m^3. The experimentally constrained equilibration pressures for all experimental studies coincide with the upper portion of the mantle wedge between the "hot nose" and the lower crust. It appears from Figure 25 that primitive magmas do not equilibrate at some common depth beneath the crust, but rather tend to equilibrate at some common distance above the "hot nose." This provides evidence that while incipient melting likely occurs in the deep portion of the mantle wedge, primary melts generally reequilibrate at some shallower depth relative to the hottest part of the wedge before erupting. This work has shown that the shallow wedge is chemically heterogeneous with respect to its mineralogy and degree of enrichment by slab fluids and inflow of asthenosphere.

The temperatures at the observed equilibration depths are consistently higher than are predicted by thermomechanical models of the mantle wedge beneath the volcanic front. This observation, coupled with the pattern shown in Figure 25, supports the hypothesis that a significant amount of heat is advected upward by ascending magmas beneath the volcanic front. This influx of heat would cause the isotherms near the "hot nose" to bend upward, reflecting locally warmer temperatures at shallower depths (e.g.,

England and Katz 2010). The consistent offset of the experimental pressures relative to the hot nose (Figure 25) provides strong support for the importance of this process.

Given the difficult and time consuming nature of experimental studies, there are several models that have been developed to predict the P-T of mantle equilibration for primitive magmas. These models are rooted in thermodynamic principles and calibrated using available experimental data (Sugawara 2000; Ghiorso et al. 2002; Lee et al. 2009; Wood and Turner 2009). One such predictive tool is the thermobarometer of Lee et al. (2009). This model (also utilized in Chapter III) calculates pressures and temperatures of melt-mantle equilibration for primitive melts. The calculated pressures are highly sensitive to changes in melt SiO_2 and alkali contents, whereas temperatures are strongly influenced by MgO and dissolved H_2O contents. I have employed this thermobarometer to calculate expected equilibrium pressures for the primitive compositions shown in Figure 24 with the goal of comparing predicted values with observed experimental data.

The first step of the Lee et al. (2009) model is to back-calculate a primitive melt from a more evolved composition by incrementally adding equilibrium olivine until a specified value for mantle olivine composition is reached (in this case, Fo_{90}). This primitive melt is then used to predict equilibrium P-T conditions. The compositions used in the experimental studies of Mexican lavas were already considered primitive (in equilibrium with Fo_{90}) and did not have olivine added to them during the experimental procedure. Consequently, this back-calculation step was not necessary for comparing predicted and observed equilibrium pressures for these five samples. The predicted values were calculated using the experimental fO_2 and H_2O contents reported by the authors. The comparison of calculated and observed results is given in Table 4. In general the

predicted equilibration pressures appear to be somewhat lower than the experimentally constrained pressures, but considering the 0.2 GPa uncertainty range of the thermobarometer, the predicted values agree well with experimental values.

Table 4. Experimental and predicted equilibration pressures for primitive TMVB lavas

Sample	Location	Approx. Exp. fO_2	Exp. H_2O (wt%)	Exp. P (GPa)	Predicted P (GPa)
M.102	Mascota (W)	QFM	2	1.6	1.5
			5	1.7	1.5
AY-509	Ayutla (W)	NNO	1.5	1.8	1.6
JR-28	MGVF (WC)	NNO	5	1.2	1.0
			7	1.4	1.1
JOR-46	MGVF (WC)	NNO+1	6	1.4	1.5
d25 (Fo_{90})	CVF (C)	NNO+0.6	5	1.0	1.0

Experiments (exp) with sample M.102 from Hesse and Grove (2003); AY-509 and JOR-46 from this study, JR-28 from Weaver et al. (2011), d25 from Weber et al. (2011). Lee et al. (2009) thermobarometer has an uncertainty of 0.2 GPa. All predicted pressures were calculated assuming equilibrium with Fo_{90} olivine. Sample d25 was also calculated for equilibrium with Fo_{92} olivine (see Weber et al. [2011] for details).

I also applied the thermobarometer to primitive melt inclusions from the TMVB. These samples were all back-corrected to be in equilibrium with Fo_{90} by adding equilibrium olivine. Figure 26 shows the results of these calculations for the calculated primitive melt inclusion (black circles) and experimental samples (open squares) with respect to SiO_2 (Figure 26a) and total alkalies (Na_2O+K_2O, Figure 26b). The calculated pressure sensitivities to these components are apparent in Figure 26, with more SiO_2-rich, and alkali-poor compositions predicted to equilibrate at generally lower pressures than SiO_2-undersaturated, alkaline melts. The experimental melts and primitive melt inclusions cover the spectrum of primitive melts that have erupted along the volcanic front in the TMVB.

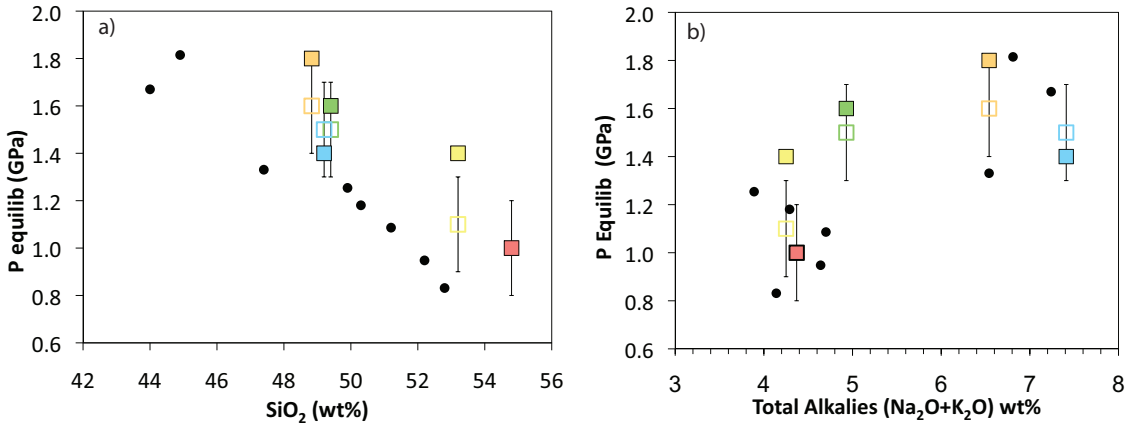

Figure 26. Predicted and measured pressures of equilibration for primitive melt inclusions and experimental samples vs. (a) SiO_2 and (b) total alkalies (Na_2O+K_2O). Melt inclusions are black circles; observed pressures for experimental samples denoted by filled squares, predicted pressures for experimental samples (as in Table 4) are denoted by open squares. Error on predicted pressures is 0.2 GPa.

It is apparent from Figure 26a that experimentally constrained pressures of equilibration are generally higher than those predicted by the model for compositions with similar SiO_2 contents, particularly for compositions with higher SiO_2 (Lee et al. 2009). There is no clear distinction between predicted and observed pressures with total alkalies. The slight offset in pressure with SiO_2 may be due to the lack of experimental data (with which this model is calibrated) for basaltic andesite and andesite compositions. It is also important to recognize that the predictive model requires the primitive melt be in equilibrium with an olivine+orthopyroxene mantle assemblage, because the silica activity (which is pressure sensitive) is buffered by the reaction $olivine_{ss}+SiO_{2\ (melt)} \Leftrightarrow orthopyroxene_{ss}$ over a range of temperatures. This requirement, therefore, precludes use of this model with any mantle-derived magma that may have equilibrated with a non-peridotite, orthopyroxene-free lithology, such as a clinopyroxene-rich vein. Despite this, the experimentally determined pressures for JOR-46 and AY-509 were both within error of

the predicted pressures. However, it is unknown how accurate the model would be for strongly Si-undersaturated melts that are products of clinopyroxenite melting (Hirschmann et al. 2003; Kogiso et al. 2004). Because clinopyroxenite residues were found experimentally in this work and others (see Chapter IV) at pressures ~1.4-1.8 GPa, the use of this barometer may be inappropriate for liquids that have equilibrated with such residues. It is likely that their low SiO_2 contents may result in predicted equilibration pressures that are higher than what would be observed from liquidus experiments. More accurate modeling results can be obtained when input parameters (i.e., magmatic H_2O, oxygen fugacity, source residue) are known. In order to have better constraints on such parameters, it is necessary to continue experimental studies that utilize chemically diverse primitive magmas under a range of P-T-H_2O conditions.

Dissertation Summary

This dissertation has focused on several geochemically distinct primitive magmas that have erupted at volcanic arcs. Primitive magmas are putative mantle melts that have undergone little to no chemical modification since last equilibrating in the mantle wedge. Since they have not been affected by differentiation processes such as crystal fractionation, magma mixing, or crustal assimilation, they can be used to infer processes occurring over the depth range ~30-80 km between their source and the surface. There were three main aims of this research: 1) to describe the role of heterogeneous mantle in producing chemically diverse primitive, mantle-derived melts; 2) to constrain the pressures (P) and temperatures (T) at which primitive magmas last equilibrated in the mantle prior to their rapid ascent to the surface; and 3) to compare experimental

observations with models (both theoretical and empirical) that aim to describe the P-T structure of subduction zones.

To address these aims I determined high-temperature, high-pressure phase equilibria for four chemically distinct primitive magmas that have erupted along the volcanic front in the Trans-Mexican Volcanic belt and the Aleutian Islands (Chapters III and IV). In Chapter II I reviewed the history of experimental petrology and provided a framework for how my experimental data set can be used to answer questions pertaining to arc magma genesis. I also described the techniques used in this work, and provided the rationale for my experimental design. These methods were referred to in the two following body chapters.

The third chapter focused on primitive lavas that represent two global endmembers in subduction zone environments. One sample is a basaltic andesite from Jorullo volcano in the Michoacán region of central Mexico, the other a basalt from Okmok volcano, central Aleutians. The goals of this study were to determine the P-T-H_2O conditions (if any) where primitive basaltic andesite may be generated in the mantle wedge, and discuss their prominence in continental arcs. One motivation for this study was the ongoing debate as to the origins of primitive basaltic andesite in which their mantle origin has been questioned. The results of my experiments show that primitive basaltic andesite lavas may be mantle-derived, and need not be differentiates of some other parental melt or products of magma mixing. Experimental phase relations show that hydrous mantle melts that have equilibrated with depleted harzburgite in the shallow upper mantle produce basaltic andesite, and that these compositions are more common in continental arc settings. Continental arcs such as Mexico and the Cascades erupt basalt

and basaltic andesite from a wide range of enriched to depleted mantle sources. In contrast, intraoceanic arcs generally produce more depleted basaltic compositions. It is evident that the processes that contribute to the formation of continental crust strongly influence the heterogeneity of the subarc mantle. The parental magmas from which more evolved compositions are derived are then strongly influenced by source mineralogy.

In Chapter IV, I concentrated on potassic alkaline basalts that show varying degrees of enrichment by subduction components (slab fluids/melts) and involve original mantle sources that are rich in incompatible trace elements, including the high field strength elements. The samples in this study are transitional between melts of enriched mantle that show little to no subduction signature (i.e., ocean island basalt [OIB] type lavas), and hydrous, potassic minette that show strong subduction signatures. The transitional nature of these magmas is evident in their major elements (K_2O, SiO_2), volatile (H_2O), and incompatible trace element signatures. They show elevated high field strength element concentrations (Nb, Ta, Ti), as well as enrichments in large ion lithophile elements (K, Rb, Sr) relative to light rare earth elements (La, Ce). Their geochemistry indicates fluid-fluxed melting of enriched sources that probably included peridotite with clinopyroxene-rich veins. Several reasons have been proposed for why such transitional lavas are rarely observed at the volcanic front. Their scarcity may be due to the low eruptibility of such magmas after the onset of low-pressure crystallization (e.g., Barclay and Carmichael 2004), and/or the likelihood that mixing of vein and wall rock melts would be high beneath the volcanic front where high-heat flux promotes melting of multiple mantle lithologies. Instead, vein melts may be more common along

regions of the arc with lower heat flow (forearc, rear arc) where vein melting would be preferential to peridotite melting due to the lower solidus temperature of the former.

A summary of this experimental work is placed in context with other experimental studies using compositions from the TMVB. This synthesis provides an along-arc perspective of primitive melt equilibration in the subarc mantle beneath the volcanic front. It appears that while melts are typically generated deep in the mantle wedge, they undergo further re-equilibration in the upper portion of the wedge just above the "hot nose."

The conclusions in this work were based on approximately 150 new high-T, high-P hydrous experiments. The experiments covered a range of P-T-H_2O-fO_2 conditions common in subduction zones and used compositions that span the natural geochemical variability of primitive arc lavas worldwide. This research successfully addressed the specific research goals, more broadly addresses outstanding questions pertaining to arc magma genesis, and provides departure points for future experimental investigations. Many experimental studies in the past have focused on incipient mantle melting at H_2O-saturated conditions with fewer studies centered on constraining H_2O-undersaturated mantle-melt phase equilibria at pressures consistent with the shallow mantle. For a variety of reasons, petrologic constraints on mantle wedge temperatures are often in disagreement with those estimated by steady-state geodynamic models. Complete experimental data sets are needed for the calibration and refining of petrologic and geophysical models that aim to describe subduction zone dynamics. Many of these geophysical models have focused on large-scale, steady state subduction zone dynamics, or more local thermal profiles of the slab-wedge interface. There remains a need for

sophisticated, well-calibrated models that focus on the shallow upper mantle wedge beneath the volcanic arc where advective heating by migrating magmas strongly influences the thermal structure. There is now significant experimental and petrologic evidence to suggest that a large proportion of primitive magmas that initially form in the deep portion of the wedge subsequently equilibrate in the shallow mantle they traverse before erupting. Therefore, the shallow mantle wedge is a key component of the larger "subduction factory", and experiments such as those presented here are essential for furthering our understanding of the genetic histories of mantle melts, from initial formation to eventual eruption.

APPENDIX A

PHASE PROPORTIONS OF JR-28 AND ID-16 EXPERIMENTS

Phase proportions (wt%) of JR-28 and ID-16 experiments calculated using a least-squares mass balance method (SIMPLEX3, M. Baker, unpublished) with standard error propagated from analytical uncertainty of phase compositions. Errors given in least units cited [e.g., 6.2(9) represents 6.2 ± 0.9]. Olivine/melt Fe/Mg K_D values calculated using Toplis (2005); Σr^2 is the sum of the squares of the residuals of mass balance calculations

	Run	P (GPa)	T (°C)	Dur (hrs)	Glass		Ol		Cpx		Opx		Sp	KD	Σr^2	Fe-Loss (Rel%)		Mg# ol/opx
Experiments with JR-28																		
~3 wt% H_2O																		
* v	CAB-38	2.0	1300	20.5	100.0						trace				0.06	-0.36	(2.3)	87
*	CAB-39	2.0	1275	11.5	90				4		6							
	CAB-45	1.7	1275	16	100.0											4.67	(2.2)	
	CAB-52	1.7	1250	17	86.1	(5)			6.2	(9)	7.7	(5)			0.23	0.07	(2.5)	85
	CAB-37	1.5	1275	20.5	100.0											-1.51	(2.2)	
	CAB-53	1.5	1250	11.5	96.5	(3)					3.5	(1)			1.24	-10.25	(2.3)	87
	CAB-54	1.5	1225	13	92.9	(3)					7.1	(2)			0.73	-10.10	(2.3)	86
	CAB-47	1.3	1250	12.5	100.0											2.47	(2.2)	
	CAB-51	1.3	1225	11	94.0	(3)					6.0	(1)			0.41	-2.40	(2.3)	86
	CAB-41	1.0	1225	20	100.0											-5.36	(2.2)	
	CAB-42	1.0	1200	12.5	98.5	(3)	1.5	(1)						0.34	0.28	-4.03	(2.3)	87
~5 Wt% H_2O																		
*	CAB-8	2.0	1275	1.5	100.0											3.61	(1.6)	
*	CAB-24	2.0	1250	18.5	97.7	(3)					2.3	(2)			0.11	-0.76	(1.5)	87
	CAB-13	2.0	1225	11.5	95.2	(6)					4.8	(4)			0.65	-4.09	(1.8)	
	CAB-33	1.7	1225	12	100.0											-2.54	(1.5)	

Appendix A (continued)

	Run	P (GPa)	T (°C)	Dur (hrs)	Glass		Ol		Cpx		Opx		Sp		KD	Σr^2	Fe-Loss (Rel%)		Mg# ol/opx
	CAB-36	1.7	1210	11.5	95.9	(3)					4.1	(1)				0.61	-5.37	(1.6)	
*	CAB-5	1.5	1225	15	100.0												0.53	(1.5)	
*	CAB-4	1.5	1200	8.5	97.1	(3)					2.9	(1)				1.14	12.37	(1.6)	87
	CAB-2	1.5	1175	7.5	97.1	(3)					2.8	(2)				0.81	7.00	(1.7)	87
*	CAB-3	1.5	1150	8	72.0	(6)			14.9	(5)	13.1	(5)				2.26	11.82	(2.3)	
*	CAB-25	1.3	1225	9	100.0												-0.67	(1.7)	
	CAB-26	1.3	1210	10	99.1	(2)							0.8	(2)		1.89	-2.71	(1.7)	
*	CAB-30	1.3	1190	11	97.6	(5)					3.3	(3)				0.80	1.00	(0.9)	88
	CAB-49	1.2	1190	11	100.0												-5.61	(1.5)	
	CAB-48	1.2	1175	12	98.3	(5)	1.7	(6)			0.0	(11)	trace		0.34	0.13	-3.63	(2.2)	88/88
*	CAB-9	1.0	1225	11	100.0								trace				5.79	(1.6)	
	CAB-7	1.0	1200	11.5	100.0								trace			0.25	0.16	(1.6)	
*	CAB-12	1.0	1175	10	98.2	(3)	1.8	(2)					trace		0.33	0.37	-3.79	(1.6)	87
~7 Wt% H_2O																			
	CAB-16	2.0	1250	12	100.0												-11.04	(5.6)	
	CAB-20	2.0	1225	11	100.0												11.30	(5.6)	
	CAB-46	2.0	1200	12.5	95.7	(5)			4.2	(4)						1.57	12.05	(5.7)	
* v	CAB-31	1.7	1200	10	99.1	(4)					0.9	(2)				0.59	3.26	(5.7)	87
	CAB-34	1.7	1175	12.5	95						5								87
	CAB-19	1.5	1225	12	100.0												-5.84	(5.6)	
	CAB-14	1.5	1200	11.5	100.0								trace				-10.03	(6.0)	
	CAB-15	1.5	1175	8.5	100.0	(4)							0.1	(9)			-3.05	(5.7)	
*	CAB-18	1.5	1150	20	95.8	(4)					4.1	(2)				1.25	-6.41	(5.6)	87

Appendix A (continued)

	Run	P (GPa)	T (°C)	Dur (hrs)	Glass		Ol		Cpx		Opx		Sp		KD	Σr^2	Fe-Loss (Rel%)		Mg# ol/opx
*	CAB-50	1.4	1150	11	99.0		0.2						trace		0.36	0.91	-1.35	(5.7)	87
	CAB-32	1.3	1185	9	100.0												-5.45	(5.6)	
	CAB-35	1.3	1160	13	99.8	(3)	0.0	(1)							0.36	1.73	3.91	(5.8)	87
	CAB-17	1.0	1175	9.5	100.0												9.35	(5.7)	
	CAB-21	1.0	1150	19	99.5	(4)	0.4	(1)							0.34	0.39	1.07	(5.6)	87
Experiments with ID-16																			
nominally anhydrous																			
	TIB-23	1.2	1315	26	99.78	(8)	0.22	(5)							0.32	1.19	9.88		89
2 wt% H_2O																			
	TIB-18	2.0	1350	19	100.0	(19)			0.00	(17)						0.52	-2.58		
	TIB-14	2.0	1325	14	91.6	(22)			8.37	(19)						1.19	-7.72		
	TIB-16	1.5	1300	12.5	93.5	(17)			6.51	(17)	0.00	(10)				0.97	2.11		87
	TIB-13	1.5	1275	9.5	79.9	(17)			19.06	(18)	1.00	(12)				0.05	1.41		85
	TIB-24	1.4	1300		100.0														
	TIB-22	1.4	1280	13	100.0	(4)	0.00	(4)							0.34	0.48	-3.94		88
	TIB-17	1.2	1280	12	98.5	(10)	1.49	(6)					0.00	(8)	0.35	0.83	-8.16		86
	TIB-19	1.1	1260	10.5	100.0								tr			0.32			
	TIB-12	1.0	1250	17.5	98.8	(8)	1.17	(5)					tr		0.34	0.43	-5.97		86
	TIB-15	1.0	1225	18	95.3	(9)	4.65	(5)					tr		0.34	0.19	-3.45		85
5 wt% H_2O																			
	TIB-5	2.0	1275	10	100.0														
	TIB-1	2.0	1250	10.5	95.0	(16)			5.01	(13)						2.76	-11.42		

Appendix A (continued)

	Run	P (GPa)	T (°C)	Dur (hrs)	Glass		Ol		Cpx		Opx		Sp		KD	Σr^2	Fe-Loss (Rel%)	Mg# ol/opx
	TIB-20	1.7	1275	16.5	100.0													
	TIB-21	1.7	1250	16.5	100.0													
	TIB-25	1.7	1225	12	85.8	(15)			12.74	(12)	1.42	(9)				1.99	-12.1	86
v	TIB-26	1.7	1200	13.5	85				15		tr							87
	TIB-7	1.5	1275	10	100.0													
	TIB-8	1.5	1250	10	100.0	(9)	0.00	(5)							0.36	0.90	-8.38	87
	TIB-9	1.5	1225	10	100.0	(9)	0.00	(5)							0.36	0.15	-3.67	87
	TIB-6	1.0	1200	10	99.9	(11)	0.05	(6)					0.00	(9)		1.37	-9.97	87
v	TIB-2	1.0	1175	10	94		4		2				tr		0.30			87
	TIB-3	1.0	1150	18.5	90.7	(15)	5.01	(5)	4.32	(11)			tr		0.34	1.06	-0.86	86

Mg# = Molar Mg/(Molar Mg + Fe) *100.
* indicates presence of quench growth
v indicates visual estimate required to obtain phase proportions due to significant quench growth

APPENDIX B

COMPOSITIONS OF EQUILIBRIUM PHASES IN JR-28 AND ID-16 EXPERIMENTS

Compositions of glasses and crystalline phases in JR-28 and ID-16 experiments with 1σ standard deviations reported below in least units cited [e.g., 49.79(30) represents 49.79 ± 0.30]. Experimental glasses of forced saturation experiments (CAB-55,56) are reported normalized anhydrous for comparison with bulk compositions reported in Table 1.

Run	P (GPa)	T (°C)	Phase	n	Na_2O	SiO_2	K_2O	Al_2O_3	MgO	CaO	TiO_2	MnO	FeO	P_2O_5	Cr_2O_3	H_2O	Total
Experiments with JR-28																	
~3 Wt% H_2O																	
CAB-38	2.0	1300	gl	6	3.31	49.79	0.76	16.20	8.89	7.79	0.71	0.11	6.90	0.23	0.09	5.22	100.0
					(19)	(30)	(1)	(20)	(12)	(25)	(3)	(1)	(9)	(1)	(3)	(32)	
			opx	5	0.18	53.66	0.00	5.37	29.71	1.58	0.06	0.16	7.81	0.00	0.70		99.3
					(1)	(44)	(0)	(85)	(39)	(7)	(1)	(2)	(9)	(1)	(11)		
CAB-39	2.0	1275	gl	7	3.37	49.84	0.81	16.63	7.93	8.18	0.77	0.13	6.76	0.25	0.07	5.26	100.0
					(11)	(34)	(1)	(24)	(3)	(25)	(2)	(2)	(6)	(1)	(1)	(36)	
			cpx	6	1.15	51.49	0.01	7.39	17.14	15.07	0.21	0.16	5.48	0.19	0.97		99.3
					(5)	(42)	(0)	(39)	(36)	(61)	(3)	(3)	(23)	(1)	(15)		
			opx	10	0.19	52.75	0.00	6.96	28.56	1.69	0.11	0.16	8.58	0.01	0.63		99.6
					(3)	(68)	(0)	(103)	(69)	(15)	(4)	(2)	(40)	(1)	(19)		
CAB-45	1.7	1275	gl	7	3.31	49.95	0.77	16.35	8.71	7.62	0.73	0.12	6.55	0.23	0.08	5.59	100.0
					(9)	(24)	(1)	(18)	(6)	(23)	(3)	(2)	(5)	(2)	(3)	(36)	
CAB-52	1.7	1250	gl	6	3.36	50.81	0.87	18.12	6.79	8.02	0.80	0.12	6.91	0.15	0.04	4.02	100.0
					(8)	(39)	(1)	(22)	(7)	(28)	(5)	(2)	(7)	(3)	(2)	(47)	
			cpx	8	1.16	50.09	0.01	8.90	16.68	15.28	0.27	0.17	5.99	0.00	0.45		99.0
					(2)	(27)	(0)	(39)	(18)	(34)	(2)	(1)	(14)	(1)	(9)		
			opx	6	0.18	51.69	0.01	7.70	28.06	1.77	0.13	0.17	9.16	0.00	0.38		99.3
					(2)	(34)	(0)	(35)	(21)	(11)	(1)	(2)	(9)	(1)			
CAB-37	1.5	1275	gl	9	3.19	49.47	0.76	15.93	8.81	8.07	0.74	0.13	6.98	0.24	0.09	5.59	100.0
					(20)	(48)	(1)	(9)	(5)	(18)	(2)	(3)	(5)	(2)	(3)	(39)	
CAB-53	1.5	1250	gl	6	3.02	49.37	0.79	16.89	8.11	7.91	0.73	0.13	7.61	0.13	0.06	5.24	100.0
					(7)	(43)	(1)	(9)	(7)	(27)	(4)	(2)	(5)	(1)	(2)		

Appendix B (continued)

Run	P (GPa)	T (°C)	Phase	n	Na_2O	SiO_2	K_2O	Al_2O_3	MgO	CaO	TiO_2	MnO	FeO	P_2O_5	Cr_2O_3	H_2O	Total
CAB-53 (continued)			opx	13	0.13	52.59	0.01	5.54	29.57	1.61	0.10	0.16	7.94	0.00	1.00		98.6
					(1)	(59)	(0)	(82)	(37)	(11)	(1)	(1)	(15)	(1)	(10)		
CAB-54	1.5	1225	gl	6	3.18	49.71	0.82	17.07	7.35	8.15	0.75	0.13	7.55	0.11	0.05	5.14	100.0
					(8)	(34)	(1)	(13)	(6)	(33)	(2)	(2)	(10)	(1)	(3)	(49)	
			opx	7	0.12	53.13	0.01	5.14	29.43	1.66	0.13	0.17	8.66	MDL	0.75		99.2
					(1)	(56)	(0)	(72)	(31)	(11)	(2)	(1)	(13)		(10)		
CAB-47	1.3	1250	gl	7	3.05	50.34	0.76	15.98	8.78	7.69	0.74	0.12	6.71	0.23	0.10	5.50	100.0
					(9)	(35)	(1)	(23)	(5)	(16)	(5)	(2)	(11)	(1)	(3)	(45)	
CAB-51	1.3	1225	gl	8	3.16	49.84	0.81	17.23	7.53	7.78	0.74	0.14	6.98	0.12	0.05	5.63	100.0
					(4)	(15)	(1)	(11)	(9)	(22)	(3)	(1)	(9)	(2)	(2)	(23)	
			opx	8	0.08	53.02	0.01	5.01	29.74	1.55	0.13	0.17	8.33	MDL	0.74		98.8
					(1)	(20)	(1)	(20)	(17)	(15)	(2)	(1)	(9)		(9)		
CAB-41	1.0	1225	gl	7	3.15	49.67	0.76	16.07	8.80	7.68	0.73	0.13	7.25	0.23	0.05	5.47	100.0
					(20)	(18)	(1)	(26)	(6)	(23)	(3)	(3)	(7)	(1)	(1)	(31)	
CAB-42	1.0	1200	gl	7	3.11	49.90	0.77	16.27	8.23	7.82	0.74	0.12	7.07	0.24	0.06	5.67	100.0
					(10)	(38)	(1)	(26)	(6)	(42)	(3)	(2)	(8)	(1)	(2)	(43)	
			ol	8	MDL	41.00	MDL	0.04	45.36	0.16	0.02	0.18	12.19	MDL	0.06		99.0
						(35)		(1)	(35)	(2)	(1)	(1)	(8)		(2)		
~5 Wt% H_2O																	
CAB-8	2.0	1275	gl	10	3.31	49.37	0.74	15.69	9.00	7.85	0.76	0.13	6.78	0.23	0.10	6.04	100.0
					(26)	(11)	(1)	(20)	(8)	(16)	(5)	(3)	(11)	(1)	(2)	(29)	
CAB-24	2.0	1250	gl	6	3.28	49.31	0.75	16.34	8.45	7.98	0.74	0.13	7.09	0.24	0.09	5.60	100.0
					(12)	(39)	(2)	(21)	(7)	(12)	(5)	(2)	(5)	(1)	(2)	(54)	
			opx	4	0.16	53.83	MDL	6.03	29.60	1.56	0.09	0.14	8.02	MDL	0.90		100.3
					(3)	(57)		(61)	(46)	(9)	(1)	(1)	(8)		(14)		
CAB-13	2.0	1225	gl	5	3.76	48.88	0.66	16.65	7.95	8.00	0.73	0.13	7.32	0.27	0.05	5.61	100.0
					(18)	(27)	(5)	(34)	(8)	(14)	(3)	(1)	(10)	(2)	(1)	(27)	
			opx	14	0.14	53.84	MDL	5.20	29.36	1.60	0.08	0.15	8.51	MDL	0.77		99.7
					(3)	(49)		(77)	(39)	(15)	(1)	(2)	(11)		(15)		

Appendix B (continued)

Run	P (GPa)	T (°C)	Phase	n	Na_2O	SiO_2	K_2O	Al_2O_3	MgO	CaO	TiO_2	MnO	FeO	P_2O_5	Cr_2O_3	H_2O	Total
CAB-33	1.7	1225	gl	7	3.33	48.17	0.74	15.72	8.72	7.86	0.69	0.13	7.12	0.22	0.09	7.21	100.0
					(17)	(19)	(1)	(13)	(6)	(13)	(2)	(3)	(8)	(1)	(2)	(16)	
CAB-36	1.7	1210	gl	7	3.25	49.21	0.75	15.65	7.92	7.99	0.64	0.11	7.32	0.12	0.05	6.97	100.0
					(48)	(18)	(1)	(29)	(5)	(10)	(5)	(2)	(8)	(1)	(1)	(69)	
			opx	8	0.09	53.60	MDL	4.31	29.81	1.57	0.07	0.12	8.17	MDL	0.72		98.5
					(3)	(74)		(111)	(64)	(9)	(2)	(2)	(18)		(14)		
CAB-5	1.5	1225	gl	10	3.43	49.32	0.73	15.65	8.81	7.80	0.73	0.13	6.98	0.24	0.08	6.11	100.0
					(23)	(19)	(2)	(27)	(5)	(23)	(5)	(3)	(7)	(2)	(2)	(22)	
CAB-4	1.5	1200	gl	11	3.58	50.19	0.75	16.51	8.36	8.03	0.72	0.12	6.24	0.21	0.06	5.22	100.0
					(16)	(29)	(4)	(43)	(5)	(26)	(2)	(2)	(23)	(1)	(2)	(73)	
			opx	6	0.13	54.65	MDL	4.19	30.03	1.57	0.12	0.14	7.70	MDL	0.82		99.4
					(2)	(65)		(84)	(29)	(15)	(2)	(1)	(6)		(15)		
CAB-2	1.5	1175	gl	10	3.40	49.24	0.74	15.68	8.17	7.93	0.74	0.11	6.43	0.22	0.07	7.28	100.0
					(16)	(27)	(4)	(30)	(17)	(16)	(4)	(3)	(19)	(1)	(3)	(54)	
			opx	29	0.14	54.12	MDL	4.96	29.27	1.68	0.14	0.15	8.01	MDL	0.90		99.4
					(3)	(42)		(47)	(29)	(20)	(2)	(1)	(9)		(14)		
CAB-3	1.5	1150	gl	9	4.30	50.84	0.91	18.87	4.44	7.25	0.81	0.11	5.63	0.25	0.01	6.57	100.0
					(48)	(40)	(6)	(35)	(80)	(17)	(6)	(3)	(40)	(2)	(2)	(61)	
			cpx	11	1.13	51.01	0.02	7.24	15.88	16.80	0.47	0.16	6.19	0.23	0.47		99.6
					(10)	(37)	(3)	(91)	(116)	(102)	(8)	(1)	(56)	(2)	(6)		
			opx	8	0.17	52.86	MDL	6.74	26.61	1.98	0.23	0.18	10.06	MDL	0.39		99.3
					(3)	(71)		(43)	(57)	(30)	(2)	(1)	(33)		(5)		
CAB-25	1.3	1225	gl	5	3.22	49.27	0.74	15.88	8.83	8.02	0.73	0.12	7.09	0.21	0.07	5.82	100.0
					(13)	(8)	(1)	(16)	(4)	(11)	(3)	(2)	(12)	(1)	(1)	(19)	
CAB-26	1.3	1210	gl	7	3.38	48.93	0.73	16.02	8.86	7.93	0.71	0.12	7.15	0.23	0.09	5.86	100.0
					(24)	(23)	(1)	(18)	(4)	(16)	(2)	(2)	(9)	(2)	(3)	(56)	
			sp	5	0.02	0.36	MDL	22.17	13.94	0.18	0.36	0.00	18.66	MDL	38.96		94.3
					(2)	(27)		(64)	(51)	(3)	(2)	(1)	(40)		(67)		
CAB-30	1.3	1190	gl	7	3.31	49.08	0.75	16.11	8.50	7.93	0.74	0.13	6.96	0.22	0.08	6.20	100.0
					(16)	(26)	(1)	(25)	(4)	(23)	(2)	(2)	(10)	(1)	(3)	(38)	

Appendix B (continued)

Run	P (GPa)	T (°C)	Phase	n	Na_2O	SiO_2	K_2O	Al_2O_3	MgO	CaO	TiO_2	MnO	FeO	P_2O_5	Cr_2O_3	H_2O	Total
CAB-30 (continued)			opx	5	0.06	54.55	MDL	4.38	30.73	1.38	0.12	0.15	7.56	MDL	1.22		100.2
					(1)	(23)		(28)	(37)	(19)	(2)	(1)	(7)		(10)		
CAB-49	1.2	1190	gl	6	2.94	48.73	0.79	14.91	8.61	7.36	0.68	0.13	7.24	0.12	0.08	8.41	100.0
					(17)	(15)	(1)	(16)	(6)	(11)	(3)	(2)	(5)	(3)	(1)	(37)	
CAB-48	1.2	1175	gl	6	3.19	49.45	0.82	15.89	8.20	7.88	0.71	0.14	7.19	0.11	0.05	6.38	100.0
					(12)	(17)	(1)	(14)	(7)	(27)	(3)	(2)	(9)	(3)	(2)	(41)	
			ol	4	MDL	40.22	MDL	0.05	46.46	0.16	0.02	0.15	11.76	MDL	0.06		98.9
						(27)		(3)	(33)	(1)	(1)	(1)	(12)		(1)		
			opx	9	0.10	54.45	0.04	3.90	30.80	1.32	0.15	0.15	7.81	MDL	0.83		99.6
					(8)	(48)	(6)	(82)	(107)	(23)	(5)	(1)	(32)		(10)		
CAB-9	1.0	1225	gl	10	3.34	49.68	0.74	15.89	8.88	7.92	0.73	0.12	6.64	0.23	0.10	5.74	100.0
					(17)	(36)	(2)	(31)	(4)	(17)	(4)	(2)	(11)	(2)	(3)	(67)	
CAB-7	1.0	1200	gl	10	3.27	49.46	0.74	15.60	8.89	7.81	0.74	0.12	7.01	0.25	0.06	6.06	100.0
					(14)	(19)	(1)	(18)	(9)	(18)	(8)	(2)	(10)	(2)	(1)	(56)	
CAB-12	1.0	1175	gl	5	3.28	50.28	0.76	16.35	8.07	8.05	0.77	0.12	7.33	0.26	0.04	4.69	100.0
					(24)	(66)	(1)	(16)	(3)	(23)	(3)	(2)	(9)	(2)	(1)	(76)	
			ol	3	0.07	41.34	0.03	0.49	44.44	0.33	0.05	0.15	12.02	MDL	0.06		99.0
					(9)	(111)	(4)	(63)	(178)	(20)	(4)	(4)	(63)		(2)		
~7 Wt% H_2O																	
CAB-16	2.0	1250	gl	3	2.49	47.99	0.69	15.58	8.78	7.70	0.67	0.12	7.89	0.25	0.08	7.75	100.0
					(12)	(44)	(2)	(9)	(7)	(33)	(3)	(2)	(13)	(3)	(1)	(67)	
CAB-20	2.0	1225	gl	6	3.45	47.72	0.74	15.66	8.88	9.09	0.71	0.11	6.35	0.23	0.09	6.98	100.0
					(22)	(23)	(1)	(16)	(3)	(11)	(3)	(2)	(9)	(1)	(3)	(36)	
CAB-46	2.0	1200	gl	7	3.28	47.21	0.76	16.28	8.41	8.44	0.72	0.14	6.32	0.25	0.04	8.15	100.0
					(12)	(24)	(1)	(15)	(5)	(42)	(4)	(3)	(7)	(2)	(1)	(65)	
			cpx	8	0.86	53.15	MDL	4.71	17.62	18.15	0.16	0.13	4.40	0.21	0.78		100.2
					(9)	(58)		(82)	(66)	(67)	(3)	(2)	(24)	(2)	(10)		
CAB-31	1.7	1200	gl	7	2.81	48.00	0.73	15.64	8.55	8.00	0.72	0.12	6.83	0.23	0.08	8.29	100.0
					(15)	(17)	(3)	(13)	(13)	(27)	(3)	(2)	(14)	(1)	(2)	(38)	
			opx	8	0.07	54.75	MDL	4.32	30.63	1.30	0.09	0.16	7.87	MDL	1.06		100.2
					(1)	(21)		(36)	(31)	(10)	(1)	(1)	(9)		(5)		

Appendix B (continued)

Run	P (GPa)	T (°C)	Phase	n	Na_2O	SiO_2	K_2O	Al_2O_3	MgO	CaO	TiO_2	MnO	FeO	P_2O_5	Cr_2O_3	H_2O	Total
CAB-34	1.7	1175	gl	7	5.38	48.49	0.82	14.54	7.97	7.43	0.56	0.08	6.79	0.10	0.06	7.79	100.0
					(52)	(25)	(3)	(26)	(11)	(11)	(3)	(1)	(14)	(2)	(3)	(52)	
			opx	17	0.06	53.79	MDL	4.01	29.86	1.35	0.08	0.12	8.27	MDL	0.76		98.3
					(4)	(52)		(43)	(41)	(13)	(2)	(2)	(14)		(9)		
CAB-19	1.5	1225	gl	7	2.86	48.03	0.74	15.16	8.70	7.78	0.70	0.12	7.49	0.22	0.09	8.10	100.0
					(20)	(34)	(1)	(8)	(11)	(10)	(2)	(2)	(9)	(2)	(1)	(43)	
CAB-14	1.5	1200	gl	5	2.28	48.20	0.69	15.71	8.72	7.71	0.71	0.12	7.82	0.24	0.10	7.70	100.0
					(9)	(38)	(1)	(14)	(3)	(19)	(2)	(2)	(32)	(2)	(3)	(67)	
			sp	5	0.00	0.14	MDL	23.09	13.16	0.15	0.49	0.00	22.03	MDL	38.58		97.5
					(3)	(10)		(31)	(22)	(2)	(6)	(2)	(40)		(84)		
CAB-15	1.5	1175	gl	5	2.17	48.56	0.72	15.72	8.68	7.61	0.67	0.11	7.28	0.25	0.07	8.17	100.0
					(12)	(18)	(2)	(21)	(20)	(21)	(3)	(3)	(15)	(3)	(3)	(45)	
CAB-18	1.5	1150	gl	6	2.22	47.90	0.75	16.20	7.85	7.86	0.70	0.11	7.49	0.26	0.05	8.62	100.0
					(15)	(44)	(2)	(16)	(5)	(32)	(2)	(2)	(9)	(1)	(1)	(68)	
			opx	26	0.09	54.25	0.01	3.99	30.02	1.36	0.10	0.16	8.35	MDL	0.89		99.2
					(2)	(56)	(1)	(62)	(40)	(14)	(1)	(2)	(29)		(13)		
CAB-50	1.4	1150	gl	6	2.72	48.74	0.81	15.18	8.40	7.31	0.66	0.13	7.21	0.14	0.05	8.65	100.0
					(3)	(20)	(3)	(20)	(3)	(39)	(2)	(2)	(13)	(1)	(1)	(53)	
			ol	8	MDL	39.73	MDL	0.03	46.13	0.13	0.02	0.14	12.49	MDL	0.05		100.0
						(8)		(0)	(25)	(2)	(1)	(1)	(24)		(2)		
CAB-32	1.3	1185	gl	7	3.08	47.70	0.73	15.62	8.70	7.81	0.68	0.11	7.49	0.23	0.06	7.80	100.0
					(18)	(43)	(2)	(11)	(10)	(19)	(3)	(2)	(10)	(1)	(1)	(46)	
CAB-35	1.3	1160	gl	7	2.64	48.41	0.73	14.62	8.81	8.06	0.58	0.10	7.20	0.11	0.06	8.67	100.0
					(31)	(31)	(1)	(27)	(7)	(18)	(4)	(3)	(12)	(1)	(2)	(59)	
			ol	12	MDL	40.17	MDL	0.03	45.75	0.15	0.01	0.12	11.95	MDL	0.05		98.4
						(39)		(2)	(14)	(4)	(2)	(3)	(9)		(3)		
CAB-17	1.0	1175	gl	4	4.57	47.87	0.74	15.55	7.89	7.76	0.62	0.12	6.41	0.24	0.08	8.15	100.0
					(42)	(54)	(13)	(10)	(8)	(49)	(4)	(2)	(9)	(2)	(1)	(66)	
CAB-21	1.0	1150	gl	7	3.29	48.44	0.72	15.71	8.67	7.83	0.74	0.14	7.06	0.23	0.05	7.14	100.0
					(26)	(29)	(1)	(12)	(3)	(29)	(2)	(1)	(6)	(1)	(1)	(45)	

Appendix B (continued)

Run	P (GPa)	T (°C)	Phase	n	Na_2O	SiO_2	K_2O	Al_2O_3	MgO	CaO	TiO_2	MnO	FeO	P_2O_5	Cr_2O_3	H_2O	Total
			ol	11	MDL	41.18	MDL	0.05	45.75	0.17	0.02	0.16	11.81	MDL	0.06		99.2
						(25)		(4)	(57)	(2)	(1)	(1)	(8)		(1)		
CAB-23	1.0	1125	gl	7	3.68	49.68	0.70	15.39	7.45	7.06	0.62	0.09	6.56	0.15	0.02	8.59	100.0
					(23)	(30)	(4)	(17)	(9)	(9)	(2)	(2)	(5)	(1)	(1)	(42)	
			ol	10	MDL	39.95	MDL	0.04	44.91	0.14	0.01	0.14	13.17	MDL	0.05		98.6
						(29)		(3)	(11)	(4)	(1)	(1)	(12)		(2)		
Forced Saturation Glasses (Normalized Anhydrous)																	
CAB-55	1.2	1175	gl	14	3.44	52.40	0.80	16.84	9.40	8.43	0.77	0.13	7.47	0.24	0.09		100.0
					(17)	(27)	(1)	(24)	(4)	(16)	(4)	(2)	(6)	(1)	(2)		
CAB-56	1.4	1150	gl	14	3.50	51.81	0.83	17.08	9.44	8.02	0.75	0.13	8.25	0.13	0.06		100.0
					(6)	(27)	(1)	(45)	(8)	(11)	(4)	(2)	(6)	(1)	(2)		
Experiments with ID-16																	
nominally anhydrous																	
TIB-23	1.2	1315	gl	6	2.05	47.61	0.54	15.95	11.31	10.60	0.71	0.16	7.72	0.10	0.09	3.16	100.0
					(18)	(41)	(0)	(17)	(12)	(18)	(3)	(2)	(4)	(1)	(3)	(36)	
			ol	8	MDL	39.70	MDL	0.07	47.92	0.25	0.01	0.18	10.91	MDL	0.06		99.1
						(30)		(1)	(33)	(3)	(2)	(1)	(25)		(1)		
2 wt% H_2O																	
TIB-18	2.0	1350	gl	6	2.11	46.51	0.56	15.41	11.31	10.26	0.70	0.18	8.13	0.10	0.09	4.64	100.0
					(20)	(37)	(1)	(26)	(10)	(34)	(4)	(2)	(7)	(2)	(2)	(36)	
			cpx	10	0.71	51.96	MDL	6.40	20.34	13.01	0.13	0.19	6.02	MDL	0.53		99.3
					(12)	(75)		(111)	(130)	(145)	(6)	(1)	(45)		(15)		
TIB-14	2.0	1325	gl	4	2.36	47.64	0.65	16.37	10.61	9.99	0.78	0.16	7.81	0.13	0.06	3.43	100.0
					(17)	(35)	(1)	(14)	(5)	(15)	(3)	(3)	(7)	(1)	(3)	(49)	
			cpx	9	0.93	50.02	0.02	9.52	17.49	14.48	0.22	0.17	5.98	MDL	0.33		99.1
					(5)	(20)	(0)	(36)	(43)	(61)	(2)	(2)	(26)		(9)		
TIB-16	1.5	1300	gl	6	2.12	46.40	0.57	15.31	10.63	10.09	0.71	0.17	9.37	0.11	0.07	4.45	100.0
					(8)	(40)	(1)	(18)	(3)	(34)	(2)	(1)	(15)	(2)	(2)	(57)	
			cpx	5	0.52	51.24	MDL	6.38	19.71	14.88	0.16	0.17	5.73	MDL	0.67		99.4
					(5)	(35)		(37)	(67)	(84)	(4)	(2)	(18)		(14)		

Appendix B (continued)

Run	P (GPa)	T (°C)	Phase	n	Na_2O	SiO_2	K_2O	Al_2O_3	MgO	CaO	TiO_2	MnO	FeO	P_2O_5	Cr_2O_3	H_2O	Total
			opx	7	0.09	52.42	MDL	6.61	29.36	2.12	0.10	0.17	7.71	MDL	0.64		99.2
					(3)	(29)		(40)	(16)	(9)	(1)	(1)	(8)		(7)		
TIB-13	1.5	1275	gl	4	2.41	46.59	0.69	17.37	9.00	9.52	0.80	0.16	8.87	0.13	0.04	4.42	100.0
					(13)	(18)	(1)	(35)	(18)	(36)	(6)	(3)	(10)	(2)	(1)	(22)	
			cpx	5	0.59	50.54	MDL	7.65	18.08	15.55	0.24	0.17	5.94	MDL	0.40		99.2
					(6)	(50)		(73)	(41)	(39)	(4)	(2)	(13)		(5)		
			opx	5	0.19	51.78	0.02	7.72	27.40	2.66	0.17	0.18	8.66	MDL	0.32		99.10
					(10)	(70)	(3)	(92)	(196)	(97)	(8)	(1)	(10)		(5)		
TIB-24	1.4	1300	gl	6	1.94	46.98	0.52	15.52	11.21	10.07	0.68	0.17	9.15	0.10	0.09	3.58	100.0
					(3)	(28)	(1)	(11)	(6)	(30)	(4)	(2)	(4)	(2)	(2)	(39)	
TIB-22	1.4	1280	gl	6	2.04	47.03	0.53	15.75	10.80	10.46	0.67	0.17	8.88	0.09	0.09	3.49	100.0
					(3)	(25)	(1)	(19)	(6)	(31)	(2)	(3)	(6)	(0)	(2)	(56)	
			ol	14	MDL	40.05	MDL	0.07	47.37	0.22	0.00	0.18	11.69	0.00	0.09		99.7
						(25)		(1)	(18)	(2)	(1)	(2)	(20)	(1)	(6)		
TIB-17	1.2	1280	gl	6	2.11	46.86	0.56	15.50	10.18	10.34	0.70	0.19	9.19	0.08	0.09	4.19	100.0
					(15)	(31)	(1)	(10)	(3)	(26)	(2)	(1)	(8)	(1)	(2)	(49)	
			ol	6	MDL	39.71	MDL	0.06	45.82	0.24	0.01	0.20	12.82	MDL	0.07		98.9
						(19)		(1)	(15)	(2)	(1)	(2)	(10)		(1)		
			sp	3	MDL	0.26	MDL	39.37	16.99	0.11	0.28	0.17	16.42	MDL	25.98		99.6
						(6)		(31)	(5)	(4)	(1)	(1)	(7)		(5)		
TIB-19	1.1	1260	gl	6	2.02	46.60	0.56	15.37	11.17	10.18	0.72	0.18	8.47	0.08	0.11	4.56	100.0
					(16)	(19)	(1)	(26)	(6)	(22)	(3)	(2)	(7)	(1)	(2)	(34)	
TIB-12	1.0	1250	gl	6	2.05	46.97	0.56	15.56	10.44	10.47	0.69	0.18	8.98	0.10	0.08	3.92	100.0
					(11)	(30)	(0)	(26)	(3)	(17)	(4)	(3)	(3)	(1)	(3)	(56)	
			ol	8	MDL	39.92	MDL	0.04	45.75	0.25	0.01	0.22	13.01	MDL	0.04		99.2
						(42)		(1)	(57)	(4)	(1)	(2)	(73)		(1)		
TIB-15	1.0	1225	gl	6	2.25	47.11	0.58	15.95	9.27	10.73	0.73	0.18	8.54	0.11	0.08	4.46	100.0
					(10)	(28)	(1)	(11)	(3)	(30)	(3)	(3)	(7)	(2)	(3)	(52)	
			ol	10	MDL	39.61	MDL	0.04	44.81	0.23	0.01	0.23	13.65	MDL	0.05		98.6
						(21)		(1)	(63)	(3)	(1)	(3)	(69)		(1)		

Appendix B (continued)

Run	P (GPa)	T (°C)	Phase	n	Na_2O	SiO_2	K_2O	Al_2O_3	MgO	CaO	TiO_2	MnO	FeO	P_2O_5	Cr_2O_3	H_2O	Total
5 wt% H_2O																	
TIB-5	2.0	1275	gl	6	1.88	45.04	0.53	14.64	10.83	10.00	0.65	0.15	9.41	0.09	0.08	6.69	100.0
					(12)	(33)	(1)	(17)	(6)	(23)	(5)	(4)	(10)	(2)	(2)	(25)	
TIB-1	2.0	1250	gl	7	2.06	44.59	0.54	15.09	10.63	10.04	0.62	0.14	9.45	0.10	0.07	6.66	100.0
					(12)	(34)	(1)	(22)	(6)	(17)	(2)	(3)	(14)	(2)	(2)	(59)	
			cpx	7	0.69	50.81	MDL	6.14	16.98	17.31	0.15	0.10	5.03	0.01	0.50		97.8
					(8)	(32)		(15)	(12)	(42)	(1)	(1)	(14)	(1)	(5)		
TIB-20	1.7	1275	gl	6	1.95	44.65	0.50	14.68	10.70	9.64	0.64	0.17	10.29	0.10	0.09	6.60	100.0
					(4)	(16)	(1)	(19)	(3)	(22)	(2)	(2)	(6)	(2)	(2)	(33)	
TIB-21	1.7	1250	gl	6	1.95	45.12	0.50	14.92	10.70	9.78	0.66	0.16	9.27	0.10	0.08	6.75	100.0
					(7)	(34)	(0)	(13)	(4)	(29)	(3)	(2)	(9)	(2)	(1)	(27)	
TIB-25	1.7	1225	gl	6	2.05	44.69	0.56	15.90	9.72	9.42	0.71	0.17	9.89	0.10	0.04	6.76	100.0
					(5)	(40)	(1)	(16)	(2)	(12)	(3)	(2)	(9)	(2)	(3)	(60)	
			cpx	8	0.61	50.84	MDL	6.52	17.37	17.84	0.20	0.16	5.52	MDL	0.47		99.5
					(6)	(73)		(85)	(115)	(106)	(3)	(2)	(25)		(7)		
			opx	7	0.07	52.80	MDL	6.20	29.63	1.65	0.09	0.17	8.55	MDL	0.35		99.5
					(1)	(49)		(99)	(41)	(17)	(2)	(2)	(49)		(7)		
TIB-26	1.7	1200	gl	6	1.97	44.29	0.56	16.11	9.58	9.14	0.71	0.18	9.87	0.11	0.04	7.43	100.0
					(2)	(28)	(1)	(26)	(5)	(29)	(4)	(4)	(7)	(3)	(2)	(40)	
			cpx	4	0.57	51.36	MDL	5.65	17.38	18.38	0.18	0.15	5.21	MDL	0.60		99.5
					(4)	(68)		(87)	(51)	(63)	(4)	(2)	(27)		(15)		
			opx	6	0.06	53.20	MDL	5.47	29.92	1.60	0.08	0.17	8.15	MDL	0.47		99.1
					(1)	(45)		(44)	(42)	(11)	(1)	(1)	(41)		(4)		
TIB-7	1.5	1275	gl	7	1.93	45.21	0.53	14.66	10.74	9.77	0.66	0.15	9.65	0.09	0.10	6.51	100.0
					(11)	(52)	(1)	(16)	(4)	(13)	(2)	(2)	(16)	(1)	(1)	(59)	
TIB-8	1.5	1250	gl	6	1.94	45.04	0.54	14.70	10.63	9.99	0.64	0.20	8.90	0.09	0.10	7.25	100.0
					(14)	(24)	(1)	(18)	(7)	(24)	(5)	(2)	(15)	(2)	(2)	(42)	
			ol	7	MDL	39.78	MDL	0.04	46.56	0.19	0.01	0.18	11.85	MDL	0.06		98.7
						(33)		(1)	(9)	(2)	(1)	(2)	(12)		(1)		

Appendix B (continued)

Run	P (GPa)	T (°C)	Phase	n	Na_2O	SiO_2	K_2O	Al_2O_3	MgO	CaO	TiO_2	MnO	FeO	P_2O_5	Cr_2O_3	H_2O	Total
TIB-9	1.5	1225	gl	6	1.93	45.56	0.54	14.73	10.63	9.97	0.70	0.18	8.53	0.08	0.09	7.06	100.0
					(9)	(22)	(1)	(15)	(5)	(29)	(5)	(1)	(10)	(2)	(2)	(50)	
			ol	10	MDL	40.03	MDL	0.04	46.67	0.21	0.02	0.17	11.91	MDL	0.05		99.1
						(13)		(2)	(9)	(3)	(1)	(1)	(7)		(1)		
TIB-6	1.0	1200	gl	6	2.00	45.33	0.54	14.89	10.43	10.04	0.64	0.16	9.19	0.08	0.08	6.61	100.0
					(14)	(24)	(1)	(15)	(3)	(39)	(4)	(3)	(10)	(2)	(1)	(73)	
			ol	8	MDL	39.89	MDL	0.05	46.18	0.23	0.02	0.19	12.14	MDL	0.04		98.8
						(18)		(6)	(28)	(5)	(2)	(1)	(27)		(1)		
TIB-2	1.0	1175	gl	6	3.58	42.88	0.93	17.47	8.58	13.43	0.63	0.17	7.54	0.12	0.01	4.67	100.0
					(20)	(56)	(2)	(51)	(9)	(34)	(3)	(2)	(18)	(1)	(1)	(83)	
			cpx	8	0.41	49.12	MDL	7.90	14.49	22.35	0.42	0.08	3.52	MDL	0.57		98.9
					(3)	(43)		(51)	(27)	(49)	(5)	(1)	(8)		(27)		
TIB-3	1.0	1150	gl	7	2.09	46.24	0.54	15.28	8.33	9.93	0.62	0.13	8.13	0.13	0.03	8.57	100.0
					(15)	(21)	(1)	(27)	(6)	(9)	(3)	(3)	(6)	(1)	(2)	(60)	
			ol	17	MDL	39.71	MDL	0.07	44.92	0.22	0.01	0.17	12.90	MDL	0.03		98.2
						(22)		(10)	(43)	(4)	(1)	(2)	(25)		(2)		
			cpx	8	0.37	49.79	MDL	6.14	15.91	19.87	0.32	0.09	5.22	MDL	0.71		98.5
					(7)	(60)		(81)	(69)	(67)	(7)	(2)	(19)		(17)		

Phase abbreviations are as follows: gl: glass, ol: olivine, opx: orthopyroxene, cpx: clinopyroxene
MDL: below the minimum detection limit
All Fe reported as FeO.

APPENDIX C

PHASE PROPORTIONS AND COMPOSITIONS OF MELTS IN HTB EXPERIMENTS

Phase proportions and compositions of melts in HTB experiments (JOR-46) with 1σ standard deviations.

5-6 wt% H_2O experiments

Run (HTB-*x*)	Bulk	31		30		12		1		6		10		18		14	
P (GPa)	--	2.0		2.0		1.7		1.5		1.5		1.5		1.5		1.4	
T (°C)	--	1250		1225		1200		1225		1200		1175		1150		1160	
fO_2 (ΔNNO)	2	2.0		-2.4		1.3		1.4		1.4		0.9		1.0		1.0	
gl		100.0				94.4		100.0		100.0		93.0		90.4		100.0	
ol																	
cpx						5.3						7.0		9.6			
sp																	
ΣR^2						0.12						0.55		0.39			
n						*7*		*6*		*6*		*7*		*8*		*7*	
		wt%	1σ sd														
Na_2O	4.71	4.37	0.36	4.91	0.14	5.01	0.16	3.62	0.20	4.49	0.18	4.90	0.38	4.79	0.46	4.61	0.26
SiO_2	50.49	50.01	0.36	48.60	0.18	50.33	0.40	51.62	0.39	50.41	0.48	50.20	0.40	49.72	0.30	50.03	0.35
K_2O	2.89	2.55	0.04	2.80	0.24	2.59	0.01	2.64	0.03	2.78	0.03	2.58	0.03	3.01	0.11	2.79	0.02
Al_2O_3	14.56	14.48	0.35	15.67	0.35	14.98	0.27	14.30	0.34	14.24	0.57	15.22	0.28	15.46	0.19	14.71	0.23
MgO	8.54	8.67	0.08	8.25	0.10	8.09	0.03	8.66	0.04	8.71	0.04	8.08	0.04	7.58	0.11	8.51	0.06
CaO	7.88	8.10	0.27	10.03	0.14	7.19	0.21	7.57	0.18	7.92	0.35	7.07	0.27	7.36	0.24	7.83	0.29
TiO_2	1.36	1.30	0.08	1.30	0.08	1.35	0.06	1.36	0.03	1.25	0.06	1.35	0.06	1.37	0.06	1.24	0.08
MnO	0.12	0.12	0.02	0.10	0.02	0.14	0.02	0.12	0.01	0.12	0.02	0.12	0.02	0.13	0.03	0.11	0.03
FeO	8.04	8.92	0.09	6.77	0.14	8.81	0.10	8.65	0.08	8.69	0.11	8.94	0.09	9.07	0.13	8.75	0.11
P_2O_5	1.41	1.41	0.03	1.53	0.03	1.47	0.03	1.40	0.04	1.35	0.06	1.51	0.02	1.48	0.02	1.38	0.03
Cr_2O_3		0.06	0.02	0.03	0.04	0.04	0.03	0.05	0.01	0.04	0.03	0.02	0.02	0.03	0.02	0.05	0.04
H_2O_{trans}	1.19									6.25							
H_2O_{ref}		4.05		5.26		5.13		6.32		6.33		5.90				5.91	

Appendix C (continued)

5-6 wt% H_2O experiments

Run (HTB-*x*)	Bulk	19		3		4		9		13		8	
P (GPa)	--	1.4		1.3		1.3		1.3		1.1		1.1	
T (°C)	--	1160		1200		1175		1150		1160		1150	
fO_2 (ΔNNO)	2	1.0		1.8		1.7		0.9		1.6		1.3	
gl		99.9		100.0		100.0		98.9		100.0		97.9	
ol								1.0				1.4	
cpx		0.0										0.7	
sp								tr				tr	
ΣR^2		0.25						0.22				0.13	
n		*7*		*7*		*7*		*7*		*7*		*7*	
Na_2O	4.71	4.90	0.31	4.05	0.13	4.41	0.18	4.49	0.16	4.39	0.15	4.69	0.16
SiO_2	50.49	50.39	0.71	51.38	0.19	51.66	0.31	50.42	0.35	50.41	0.26	51.14	0.26
K_2O	2.89	2.85	0.02	2.65	0.03	1.53	0.04	2.76	0.03	2.68	0.04	2.42	0.03
Al_2O_3	14.56	14.50	0.42	14.22	0.15	14.39	0.15	14.52	0.26	14.18	0.26	14.62	0.39
MgO	8.54	8.70	0.06	8.69	0.05	8.86	0.04	8.12	0.04	8.66	0.09	7.92	0.05
CaO	7.88	8.21	0.16	7.57	0.14	7.57	0.12	7.93	0.22	8.01	0.26	7.91	0.44
TiO_2	1.36	1.32	0.07	1.34	0.02	1.35	0.05	1.33	0.07	1.28	0.05	1.27	0.05
MnO	0.12	0.13	0.03	0.12	0.02	0.12	0.01	0.12	0.01	0.12	0.02	0.12	0.02
FeO	8.04	8.94	0.10	8.55	0.07	8.61	0.05	8.86	0.06	8.82	0.09	8.44	0.15
P_2O_5	1.41	1.38	0.05	1.37	0.03	1.44	0.04	1.42	0.03	1.36	0.03	1.43	0.05
Cr_2O_3		0.04	0.02	0.05	0.01	0.05	0.02	0.03	0.04	0.07	0.04	0.03	0.04
H_2O_{trans}	1.19									5.29			
H_2O_{ref}				5.51		5.29		5.68		5.55		5.84	

Appendix C (continued)

3-4 wt% H_2O experiments

Run	23		21		24		22		27		25	
P (Gpa)	1.3		1.3		1.1		1.1		0.9		0.9	
T (°C)	1200		1175		1200		1175		1175		1150	
fO_2 (ΔNNO)	1.9		0.6		1.8		1.4		0.5		0.3	
gl	96		89.8		100		97		100		93	
ol	1		0.1				0.3				2	
cpx	3		9.2				3.0				4	
sp												
ΣR^2	0.38		0.58				0.66				0.97	
n	*7*		*7*		*7*		*6*		*6*		*6*	
Na_2O	4.68	0.33	4.90	0.24	4.67	0.20	4.94	0.12	4.53	0.31	4.65	0.40
SiO_2	50.82	0.48	51.13	0.30	50.87	0.24	50.97	0.16	51.37	0.43	52.12	0.37
K_2O	2.75	0.03	2.61	0.03	2.62	0.02	2.63	0.01	2.80	0.01	2.92	0.02
Al_2O_3	14.69	0.34	15.28	0.19	14.11	0.22	14.55	0.08	14.16	0.18	14.97	0.49
MgO	8.30	0.07	7.58	0.08	8.65	0.07	8.05	0.03	8.29	0.04	6.79	0.06
CaO	7.32	0.26	6.66	0.24	7.53	0.41	7.41	0.12	7.34	0.09	7.56	0.22
TiO_2	1.27	0.07	1.36	0.09	1.27	0.08	1.32	0.02	1.30	0.07	1.33	0.05
MnO	0.13	0.02	0.12	0.02	0.15	0.04	0.11	0.01	0.13	0.01	0.10	0.03
FeO	8.62	0.11	8.88	0.13	8.78	0.12	8.64	0.05	8.52	0.04	7.97	0.07
P_2O_5	1.35	0.05	1.47	0.07	1.30	0.05	1.34	0.01	1.53	0.02	1.57	0.03
Cr_2O_3	0.06	0.03	0.01	0.03	0.05	0.04	0.04	0.01	0.03	0.03	0.03	0.03
H_2O_{trans}												
H_2O_{ref}	3.51		4.30		3.97		3.98		3.32		4.40	

All Fe reported as FeO

Phase abbreviations: gl: glass, ol: olivine, cpx: clinopyroxene, sp: spinel, tr: trace

H_2O contents obtained by transmission (trans) or reflective (ref) FTIR techniques

APPENDIX D

COMPOSITIONS OF CRYSTALLINE PHASES IN HTB EXPERIMENTS

Compositions of equilibrium crystal phases in HTB experiments (JOR-46) with 1σ standard deviations

Pyroxene Compositions

Run (HTB-*x*)	29		32		30		12				10				18	
P (GPa)	2.3		2.3		2.0		1.7				1.5				1.5	
T (°C)	1250		1225		1225		1200				1175				1150	
fO_2 (ΔNNO)							1.3				0.9				1.4	
	wt%	1σ sd					*Rim*		*Core*		*Rim*		*Core*			
Na_2O	1.66	0.12	1.63	0.13	1.08	0.17	1.42	0.08	0.54	0.05	1.16	0.11	0.45	0.09	1.10	0.08
SiO_2	54.11	0.40	53.72	0.53	54.55	0.38	52.77	0.50	51.13	0.47	52.56	0.36	52.4	1.42	52.36	0.35
K_2O	0.02	0.01	0.01	0.00	0.01	0.01										
Al_2O_3	7.93	0.52	4.90	0.76	3.97	0.70	4.70	0.43	3.39	0.35	4.12	0.26	2.47	0.94	4.04	0.17
MgO	16.69	0.43	16.49	0.84	16.61	0.47	16.98	0.16	14.92	0.20	17.24	0.27	15.67	0.74	16.43	0.26
CaO	15.76	0.97	18.69	0.80	20.82	1.09	18.11	0.73	22.76	0.40	18.32	0.24	22.51	0.41	19.06	0.45
TiO_2	0.53	0.10	0.35	0.09	0.32	0.04	0.39	0.05	1.10	0.10	0.41	0.04	0.78	0.25	0.46	0.04
MnO	0.13	0.01	0.10	0.02	0.09	0.02	0.12	0.01	0.11	0.02	0.12	0.02	0.13	0.03	0.12	0.02
FeO	6.20	0.19	5.33	0.18	4.40	0.82	6.10	0.21	6.77	0.25	5.95	0.19	6.21	0.68	6.09	0.14
P_2O_5	0.03	0.02	0.03	0.01	0.03	0.01						0.01		0.04		
Cr_2O_3	0.18	0.08	0.50	0.22	0.28	0.07	0.39	0.06	0.11	0.16	0.59	0.18	0.16	0.14	0.46	0.08
NiO																
Total	103.24		101.75		102.17		100.98		100.85		100.47		100.81		100.12	
Composition																
Wo	36		41		44		39		47		39		46		41	
En	*53*		*50*		*49*		51		43		51		44		49	
Fs	*11*		*9*		*7*		10		10		10		10		10	

Appendix D (continued)

Pyroxene Compositions

Run (HTB-*x*)	19		8		23				21		22	
P (GPa)	1.4		1.1		1.3				1.3		1.1	
T (°C)	1160		1150		1200				1175		1175	
fO_2 (ΔNNO)	1.0		1.3		1.9				1.6		1.4	
	wt%	1σ sd			*A*		*B*					
Na_2O	0.95	0.13	0.81	0.12	0.94	0.06	1.05	0.04	1.15	0.06	0.99	0.11
SiO_2	53.27	0.78	53.2	1.2	52.55	0.26	50.91	0.18	50.23	0.32	51.23	0.49
K_2O												
Al_2O_3	2.80	0.68	2.76	0.82	2.77	0.14	4.05	0.25	4.64	0.19	3.36	0.42
MgO	17.9	1.1	18.3	1.1	18.64	0.28	16.41	0.22	15.83	0.43	16.70	0.75
CaO	18.63	0.80	19.27	0.63	17.08	0.52	18.90	0.37	18.98	0.47	18.69	0.34
TiO_2	0.29	0.05	0.36	0.12	0.27	0.02	0.42	0.03	0.59	0.11	0.39	0.06
MnO	0.11	0.02	0.13	0.01	0.14	0.01	0.11	0.01	0.12	0.01	0.12	0.01
FeO	5.11	0.20	5.34	0.44	5.40	0.09	5.53	0.10	6.31	0.21	5.38	0.20
P_2O_5					0.02	0.01	0.03	0.02	0.05	0.02	0.06	0.03
Cr_2O_3	0.70	0.25	0.62	0.20	0.66	0.06	0.94	0.08	0.47	0.19	0.92	0.13
NiO					0.07	0.01	0.07	0.02	0.08	0.01	0.07	0.01
Total	99.76		100.70		98.55		98.42		98.47		97.92	
Composition												
Wo	37-41		38-43		36		41		41		39-41	
En	50-54		48-53		55		50		48		48-52	
Fs	8-9		8-10		9		9		11		9	

Appendix D (continued)

Olivine Compositions

Run (HTB-*x*)	9		8		23		21		22		25	
P (GPa)	1.3		1.1		1.3		1.3		1.1		0.9	
T (°C)	1150		1150		1200		1175		1175		1150	
fO_2 (ΔNNO)	0.9		1.3		1.9		1.6		1.4		0.25	
Na_2O												
SiO_2	40.79	0.20	40.67	0.12	40.27	0.16	39.83	0.18	40.19	0.18	40.81	0.23
K_2O												
Al_2O_3	0.03	0.01	0.03	0.02	0.03	0.02	0.02	0.01	0.02	0.01	0.02	0.01
MgO	47.21	0.28	47.75	0.07	47.31	0.09	46.19	0.25	46.80	0.20	45.78	0.10
CaO	0.16	0.02	0.16	0.02	0.18	0.03	0.18	0.02	0.16	0.02	0.16	0.05
TiO_2	0.03	0.01	0.03	0.01	0.02	0.02	0.02	0.02	0.01	0.02	0.02	0.02
MnO	0.17	0.01	0.15	0.01	0.16	0.02	0.17	0.01	0.17	0.02	0.17	0.01
FeO	11.79	0.34	11.36	0.09	10.23	0.09	11.69	0.21	11.36	0.20	12.06	0.17
P_2O_5	0.04	0.01	0.04	0.01	0.04	0.02	0.05	0.03	0.05	0.02	0.04	0.02
Cr_2O_3	0.03	0.02	0.03	0.02	0.02	0.01	0.03	0.01	0.02	0.01	0.02	0.02
NiO					0.44	0.03	0.44	0.04	0.43	0.06		
Total	100.21		100.19		98.70		98.79		99.23		99.09	
Mg#	87.7		88.2		89.2		87.6		88.0		87.1	
K_D	0.31		0.31		0.30		0.31		0.30		0.3	
FeO/FeO^T	0.70		0.66		0.60		0.74		0.65		0.75	

All Fe reported as FeO
Composition abbreviations: Wo: wollastonite, En: enstatite, Fs: ferrosilite
Mg#=Molar Mg/(Molar Mg+Fe)*100

APPENDIX E

PHASE PROPORTIONS AND COMPOSITIONS OF MELTS IN ALK EXPERIMENTS

Phase proportions and compositions of melts in ALK experiments (AY-509) with 1σ standard deviations.

1.5 wt% H_2O experiments

Run	Bulk	ALK18		ALK14		ALK5		ALK16		ALK12		ALK17		ALK7		ALK10	
P (GPa)	--	2.3		2.0		2.0		2.0		1.8		1.8		1.7		1.5	
T (°C)	--	1300		1325		1300		1275		1300		1275		1280		1300	
fO_2 (ΔNNO)		-1.3		-0.4		0.7				-0.3		-0.5		0.2		-0.8	
gl		100		100		94.6		75		96.5		83		82.9		98	
ol										2.7		16.9				2	
cpx						5.4		23						12.1(A); 5(B)			
ΣR^2						0.13		3.3*		0.41		0.22		0.8		.57*	
n		*6*		*6*		*9*		*6*		*6*		*6*		*7*		*6*	
		wt%	1σ s.d.														
Na_2O	5.05	4.84	0.30	4.94	0.21	5.13	0.16	6.79	0.27	4.94	0.20	5.27	0.29	5.58	0.22	5.17	0.15
SiO_2	49.57	49.66	0.35	50.20	0.36	49.81	0.45	49.80	0.50	50.37	0.29	49.04	0.56	48.37	0.35	50.41	0.27
K_2O	1.59	1.57	0.11	1.66	0.02	1.70	0.05	2.45	0.26	1.70	0.03	1.93	0.07	1.78	0.04	1.69	0.02
Al_2O_3	14.91	15.45	0.45	15.13	0.26	15.26	0.67	18.11	0.19	15.37	0.17	16.63	0.24	16.45	0.10	15.31	0.40
MgO	9.99	10.25	0.14	9.71	0.05	9.75	0.27	8.73	0.07	8.92	0.09	8.66	0.27	9.03	0.14	9.58	0.11
CaO	8.42	8.54	0.23	7.74	0.29	7.84	0.32	8.48	0.47	8.20	0.14	7.28	0.27	7.22	0.26	7.88	0.34
TiO_2	1.11	1.11	0.08	1.06	0.06	1.14	0.04	1.34	0.11	1.14	0.07	1.24	0.09	1.15	0.09	1.15	0.10
MnO	0.13	0.12	0.03	0.11	0.02	0.14	0.02	0.12	0.02	0.12	0.02	0.14	0.02	0.13	0.02	0.15	0.02
FeO	8.21	7.28	0.07	8.18	0.08	8.13	0.15	2.68	0.21	7.98	0.33	8.55	0.09	9.09	0.14	7.41	0.11
P_2O_5	1.02	1.07	0.06	1.21	0.04	1.04	0.08	1.51	0.07	1.20	0.04	1.25	0.04	1.17	0.04	1.19	0.03
Cr_2O_3		0.11	0.03	0.05	0.03	0.06	0.03	-0.01	0.03	0.06	0.03	0.01	0.02	0.02	0.03	0.06	0.04
H_2O_{trans}						1.51								2.12			
H_2O_{ref}						1.70								1.96			

Appendix E (continued)

1.5 wt% H_2O experiments

Run	Bulk	ALK6		ALK9		ALK8		ALK13	
P (GPa)	--	1.5		1.3		1.2		1.1	
T (°C)	--	1280		1275		1270		1300	
fO_2 (ΔNNO)		0.2		0.2		0.5		-2.4	
gl		92.1		95.3		98.2		100	
ol		0.6		1		1.8			
cpx		7.3		4					
sp						tr			
ΣR^2		0.32		0.43		0.66			
n		*7*		*6*		*7*		*6*	
Na_2O	5.05	5.19	0.20	5.21	0.13	5.21	0.36	4.84	0.24
SiO_2	49.57	49.30	0.32	49.36	0.25	49.36	0.27	50.90	0.22
K_2O	1.59	1.71	0.02	1.66	0.02	1.66	0.02	1.71	0.02
Al_2O_3	14.91	15.59	0.28	15.16	0.19	15.16	0.17	15.13	0.23
MgO	9.99	9.01	0.04	9.14	0.07	9.14	0.06	11.28	0.03
CaO	8.42	7.95	0.18	8.31	0.27	8.31	0.29	9.99	0.25
TiO_2	1.11	1.15	0.07	1.12	0.03	1.12	0.08	1.14	0.05
MnO	0.13	0.14	0.02	0.13	0.02	0.13	0.02	0.14	0.03
FeO	8.21	8.89	0.11	8.89	0.09	8.89	0.09	3.66	0.13
P_2O_5	1.02	1.05	0.04	0.98	0.03	0.98	0.04	1.18	0.03
Cr_2O_3		0.03	0.02	0.04	0.04	0.04	0.02	0.03	0.03
H_2O_{trans}		1.51				1.40			
H_2O_{ref}		1.65				1.59			

All Fe reported as FeO

Phase abbreviations: gl: glass, ol: olivine, cpx: clinopyroxene, sp: spinel, tr: trace

H_2O contents obtained by transmission (trans) or reflective (ref) FTIR techniques

APPENDIX F

COMPOSITIONS OF CRYSTALLINE PHASES IN ALK EXPERIMENTS

Compositions of equilibrium crystal phases in ALK experiments (AY-509) with 1σ standard deviations.

Pyroxene Compositions

Run	ALK5		ALK16		ALK17		ALK7(A)		ALK7(B)		ALK6		ALK9	
P (GPa)	2.0		2.0		1.8		1.7		1.7		1.5		1.3	
T (°C)	1300		1275		1275		1280		1280		1280		1275	
fO_2 (ΔNNO)	0.7				-0.5		0.2		0.2		0.2		0.5	
Na_2O	1.85	0.12	1.94	0.09	1.69	0.09	1.63	0.11	1.08	0.10	1.18	0.07	1.25	0.07
SiO_2	50.06	0.53	51.83	0.44	53.95	0.39	49.45	0.58	52.50	0.28	51.04	0.78	50.8	0.21
K_2O	0.02	0.02	0.03	0.01	0.02	0.01	0.01	0.00	0.00	0.01	0.00	0.00		
Al_2O_3	8.79	0.30	8.36	0.37	8.13	0.31	8.02	0.40	4.04	0.26	5.86	1.02	6.45	0.16
MgO	15.85	0.52	16.10	0.39	17.59	0.32	16.37	0.37	22.29	0.48	17.45	0.85	16.95	0.15
CaO	14.28	0.52	16.03	1.44	14.34	0.60	15.82	0.42	11.28	0.66	16.28	0.59	15.68	0.23
TiO_2	0.48	0.11	0.46	0.06	0.50	0.06	0.50	0.11	0.21	0.03	0.36	0.08	0.37	0.03
MnO	0.15	0.01	0.12	0.02	0.15	0.02	0.14	0.01	0.18	0.01	0.14	0.01	0.13	0.01
FeO	6.62	0.32	3.61	1.09	6.49	0.28	6.55	0.18	6.72	0.20	5.96	0.14	5.41	0.17
P_2O_5	0.04	0.02	0.03	0.01	0.04	0.02	0.02	0.01	0.01	0.01	0.01	0.02	0.04	0.01
Cr_2O_3	0.16	0.05	0.21	0.08	0.18	0.06	0.24	0.07	0.29	0.07	0.61	0.10	0.66	0.08
NiO	0.04	0.02	n/a		n/a		0.06	0.01	0.08	0.01	0.04	0.01		0.41
Total	98.33		98.71		103.08		98.80		98.69		98.93		97.71	
Composition														
Wo	34		39		33		36		24		36		36	
En	53		54		56		53		65		53		54	
Fs	12		7		11		11		11		10		10	

Appendix F (continued)

Olivine Compositions

Run	ALK12		ALK10		ALK6		ALK9		ALK8	
P (GPa)	1.8		1.5		1.5		1.3		1.2	
T (°C)	1300		1300		1280		1275		1270	
fO_2 (ΔNNO)	-0.3		-0.8		0.2		0.2		0.5	
Na_2O	0.03	0.02	0.02	0.02	0.03	0.01	0.01	0.02	0.03	0.05
SiO_2	41.04	0.10	41.06	0.24	40.10	0.17	41.12	0.19	40.19	0.23
K_2O	0.00	0.00	0.00	0.01	0.01	0.00	0.00	0.00	0.00	0.01
Al_2O_3	0.06	0.02	0.07	0.02	0.06	0.02	0.07	0.01	0.09	0.14
MgO	46.51	0.15	46.47	0.08	46.08	0.41	46.51	0.14	47.22	0.30
CaO	0.20	0.02	0.20	0.03	0.23	0.04	0.21	0.02	0.26	0.09
TiO_2	0.01	0.02	0.01	0.02	0.02	0.02	0.01	0.01	0.02	0.02
MnO	0.16	0.02	0.15	0.02	0.17	0.01	0.16	0.01	0.16	0.01
FeO	11.67	0.10	11.01	0.16	12.15	0.16	11.37	0.10	10.99	0.25
P_2O_5	0.05	0.03	0.07	0.02	0.05	0.02	0.05	0.03	0.07	0.04
Cr_2O_3	0.05	0.02	0.05	0.02	0.03	0.02	0.04	0.01	0.05	0.02
NiO					0.23	0.02			0.31	0.02
Total	99.78		99.11		99.15		99.54		99.39	
Mg#	0.877		0.883		0.871		0.879		0.885	
K_D	0.31		0.31		0.30		0.30		0.30	
FeO/FeO^T	0.80		0.84		0.77		0.74		0.74	

All Fe reported as FeO

Composition abbreviations: Wo: wollastonite, En: enstatite, Fs: ferrosilite

Mg#=Molar Mg/(Molar Mg+Fe)*100

REFERENCES CITED

Chapter I

Abers G, van Keken P, Kneller E, Ferris A, Stachnik J (2006) The thermal structure of subduction zones constrained by seismic imaging: Implications for slab dehydration and wedge flow. Earth Planet Sci Lett 241:387-397

Asimow P, Longhi J (2004) The significance of multiple saturation points in the context of polybaric near-fractional melting. J Petrol 45(12):2349-2367

Baker MB, Grove TL, Price R (1994) Primitive basalts and andesites from the Mt Shasta Region, N California - products of varying melt fraction and water-content. Contrib Mineral Petrol 118(2):111-129

Carmichael I, Lange R, Luhr J (1996) Quaternary minettes and associated volcanic rocks of Mascota, western Mexico: A consequence of plate extension above a subduction modified mantle wedge. Contrib Mineral Petrol 124:302-333

Falloon TJ, Danyushevsky LV (2000) Melting of refractory mantle at 1.5, 2 and 2.5 GPa under, anhydrous and H_2O-undersaturated conditions: Implications for the petrogenesis of high-Ca boninites and the influence of subduction components on mantle melting. J Petrol 41(2):257-283

Ferrari L (2004) Slab detachment control on mafic volcanic pulse and mantle heterogeneity in central Mexico. Geology 32(1):77

Ferrari L, Petrone CM, Francalanci L (2001) Generation of oceanic-island basalt–type volcanism in the western Trans-Mexican volcanic belt by slab rollback, asthenosphere infiltration, and variable flux melting. Geology 29(6):507

Gaetani G, Grove T (1998) The influence of water on melting of mantle peridotite. Contrib Mineral Petrol 131:323-346

Grove TL, Chatterjee N, Parman SW, Médard E (2006) The influence of H_2O on mantle wedge melting. Earth Planet Sci Lett 249:74-98

Hacker BR, Abers GA, Peacock SM (2003) Subduction factory - 1. Theoretical mineralogy, densities, seismic wave speeds, and H_2O contents. J Geophys Res 108(B1):10.1029/2001jb001127

Hesse M, Grove TL (2003) Absarokites from the western Mexican Volcanic Belt: constraints on mantle wedge conditions. Contrib Mineral Petrol 146(1):10-27

Hirose K (1997) Melting experiments on lherzolite KLB-1 under hydrous conditions and generation of high-magnesian andesitic melts. Geology 25(1):42

Hirose K, Kawamoto T (1995) Hydrous partial melting of lherzolite at 1 GPa: the effect of H_2O on the genesis of basaltic magmas. Earth Planet Sci Lett 133(3-4):463-473

Johnson ER, Wallace PJ, Delgado Granados H, Manea VC, Kent AJR, Bindeman IN, Donegan CS (2009) Subduction-related volatile recycling and magma generation beneath Central Mexico: Insights from melt inclusions, oxygen isotopes and geodynamic models. J Petrol 50(9):1729-1764

Kushiro I (1969) System forsterite-diopside-silica with and without water at high pressures. Am J Sci 267:269-294

Kushiro I (1972) Effect of water on composition of magmas formed at high-pressures. J Petrol 13(2):311-334

Lange RA, Carmichael ISE (1990) Hydrous basaltic andesites associated with minette and related lavas in western Mexico. J Petrol 31(6):1225-1259

Liu X, O'Neill HSC, Berry AJ (2006) The effects of small amounts of H_2O, CO_2 and Na_2O on the partial melting of spinel lherzolite in the system $CaO{-}MgO{-}Al_2O_3{-}SiO_2 \pm H_2O \pm CO_2 \pm Na_2O$ at 1.1 GPa. J Petrol 47(2):409-434

Luhr JF (1997) Extensional tectonics and the diverse primitive volcanic rocks in the western Mexican Volcanic Belt. Can Mineral 35:473-500

Luhr JF, Allan JF, Carmichael ISE, Nelson SA, Hasenaka T (1989) Primitive calc-alkaline and alkaline rock types from the Western Mexican Volcanic Front. J Geophys Res 94(B4):4515-4530

Luhr JF, Carmichael ISE (1985) Jorullo Volcano, Michoacan, Mexico (1759-1774): The earliest stages of fractionation in calc-alkaline magmas. Contrib Mineral Petrol 90:142-161

Manea VC, Manea M, Kostoglodov V, Currie CA, Sewell G (2004) Thermal structure, coupling and metamorphism in the Mexican subduction zone beneath Guerrero. Geophys J Int 158(2):775-784

Médard E, Grove TL (2008) The effect of H_2O on the olivine liquidus of basaltic melts: experiments and thermodynamic models. Contrib Mineral Petrol 155(4):417-432

Nicholls IA, Ringwood AE (1973) The effect of water on olivine stability in tholeiites and the production of silica-saturated magmas in the island arc environment. J Geol 81:285-300

Pardo M, Suarez G (1993) Steep subduction geometry of the Rivera plate beneath the Jalisco block in Western Mexico. Geophys Res Lett 20(21):2391-2394

Pardo M, Suarez G (1995) Shape of the subducted Rivera and Cocos plates in Southern Mexico - Seismic and tectonic tmplications. J Geophys Res 100(B7):12357-12373

Parman SW, Grove TL (2004) Harzburgite melting with and without H_2O: Experimental data and predictive modeling. J Geophys Res 109(B2):B02201

Peacock SM, Rushmer T, Thompson AB (1994) Partial melting of subducting oceanic-crust. Earth Planet Sci Lett 121(1-2):227-244

Perez-Campos X, Kim Y, Husker A, Davis PM, Clayton RW, Iglesias A, Pacheco JF, Singh SK, Manea VC, Gurnis M (2008) Horizontal subduction and truncation of the Cocos Plate beneath central Mexico. Geophys Res Lett 35(18):L18303

Pichavant M, Mysen BO, Macdonald R (2002) Source and H_2O content of high-MgO magmas in island arc settings: An experimental study of a primitive calc-alkaline basalt from St. Vincent, Lesser Antilles Arc. Geochim Cosmochim Acta 66(12):2193-2209

Schmidt MW, Poli S (1998) Experimentally based water budgets for dehydrating slabs and consequences for arc magma generation. Earth Planet Sci Lett 163(1-4):361-379

Stern C, Huang W-L, Wyllie PJ (1975) Basalt-andesite-rhyolite-H_2O: crystallization intervals with excess H_2O and H_2O-undersaturated liquidus surfaces to 35 kilobars, with implications for magma genesis. Earth Planet Sci Lett 28:189-196

Straub SM, LaGatta AB, Martin-Del Pozzo AL, Langmuir CH (2008) Evidence from high-Ni olivines for a hybridized peridotite/pyroxenite source for orogenic andesites from the central Mexican Volcanic Belt. Geochem Geophys Geosyst 9(3)

Streck MJ, Leeman WP, Chesley J (2007) High-magnesian andesite from Mount Shasta: A product of magma mixing and contamination, not a primitive mantle melt. Geology 35(4):351-354

van Keken PE, Kiefer B, Peacock SM (2002) High-resolution models of subduction zones: Implications for mineral dehydration reactions and the transport of water into the deep mantle. Geochem Geophys Geosyst 3:doi: 10.1029/2001gc000256

Wallace P, Carmichael ISE (1999) Quaternary volcanism near the Valley of Mexico: implications for subduction zone magmatism and the effects of crustal thickness variations on primitive magma compositions. Contrib Mineral Petrol 135(4):291-314

Wallace PJ (2005) Volatiles in subduction zone magmas: concentrations and fluxes based on melt inclusion and volcanic gas data. J Volcanol Geotherm Res 140(1-3):217-240

Winter JD (2001) An introduction to igneous and metamorphic petrology. Prentice Hall, Upper Saddle River

Yang T, Grand SP, Wilson D, Guzman-Speziale M, Gomez-Gonzalez JM, Dominguez-Reyes T, Ni J (2009) Seismic structure beneath the Rivera subduction zone from finite-frequency seismic tomography. J Geophys Res 114

Yoder HS, Tilley CE (1962) Origin of basalt magmas: An experimental study of natural and synthetic rock systems. J Petrol 3(3):342-532

Chapter II

Baker MB, Grove TL, Price R (1994) Primitive basalts and andesites from the Mt Shasta Region, N California - products of varying melt fraction and water-content. Contrib Mineral Petrol 118(2):111-129

Baker MB, Hirschmann MM, Ghiorso MS, Stolper EM (1995) Compositions of near-solidus peridotite melts from experiments and thermodynamic calculations. Nature 375(6529):308-311

Baker MB, Stolper EM (1994) Determining the composition of high-pressure mantle melts using diamond aggregates. Geochim Cosmochim Acta 58(13):2811-2827

Bowen NL (1914) The ternary system: diopside-forsterite-silica. Am J Sci 4(38):207-264

Bowen NL, Anderson O (1914) The binary system MgO-SiO_2. Am J Sci 4(37):487-500

Cagnioncle AM, Parmentier EM, Elkins-Tanton LT (2007) Effect of solid flow above a subducting slab on water distribution and melting at convergent plate boundaries. J Geophys Res 112(B9):B09402

Day AL (1906) Investigation of mineral solution and fusion under high temperatures and pressures. CIWYB 5:177-185

Gaetani G, Grove T (1998) The influence of water on melting of mantle peridotite. Contrib Mineral Petrol 131:323-346

Geschwind C-H (1995) Becoming interested in experiments: American igneous petrologists and the Geophysical Laboratory, 1905-1965. Earth Sciences History 14(1):47-61

Ghiorso MS, Hirschmann MM, Reiners PW, Kress VC (2002) The pMELTS: A revision of MELTS for improved calculation of phase relations and major element partitioning related to partial melting of the mantle to 3 GPa. Geochem Geophys Geosyst 3(1030):doi: 10.1029/2001gc000217

Gill JB (1981) Orogenic andesites and plate tectonics. Springer Verlag, Berlin

Green DH, Ringwood AE (1967) The genesis of basaltic magmas. Contrib Mineral Petrol 15(2):103-190

Grove T, Parman S, Bowring S, Price R, Baker M (2002) The role of an H_2O-rich fluid component in the generation of primitive basaltic andesites and andesites from the Mt. Shasta region, N California. Contrib Mineral Petrol 142(4):375-396

Hall LJ, Brodie J, Wood BJ, Carroll MR (2004) Iron and water losses from hydrous basalts contained in $Au_{80}Pd_{20}$ capsules at high pressure and temperature. Mineral Mag 68(1):75-81

Hirose K, Kawamoto T (1995) Hydrous partial melting of lherzolite at 1 GPa: the effect of H_2O on the genesis of basaltic magmas. Earth Planet Sci Lett 133(3-4):463-473

Hirose K, Kushiro I (1993) Partial melting of dry peridotites at high-pressures - determination of compositions of melts segregated from peridotite using aggregates of diamond. Earth Planet Sci Lett 114(4):477-489

Hirschmann MM, Baker MB, Stolper EM (1998) The effect of alkalis on the silica content of mantle-derived melts. Geochim Cosmochim Acta 62(5):883-902

Kawamoto T, Hirose K (1994) Au-Pd sample containers for melting experiments on iron and water-bearing systems. Eur J Mineral 6(3):381-385

Kelemen PB (1995) Genesis of high Mg-number andesites and the continental crust. Contrib Mineral Petrol 120(1):1-19

Kushiro I (1968) Compositions of magmas formed by partial zone melting of Earth's upper mantle. J Geophys Res 73(2):619-634

Kushiro I (1969a) Effect of water on compositions of magmas formed in upper mantle. EOS., Trans AGU 50(4):355

Kushiro I (1969b) System forsterite-diopside-silica with and without water at high pressures. Am J Sci 267:269-294

Kushiro I (1972) Effect of water on composition of magmas formed at high-pressures. J Petrol 13(2):311-334

Lee C-TA, Luffi P, Plank T, Dalton H, Leeman WP (2009) Constraints on the depths and temperatures of basaltic magma generation on Earth and other terrestrial planets using new thermobarometers for mafic magmas. Earth Planet Sci Lett 279(1-2):20-33

Myers J, Eugster HP (1983) The system Fe-Si-O - oxygen buffer calibrations to 1,500 K. Contrib Mineral Petrol 82(1):75-90

Nicholls IA, Ringwood AE (1973) The effect of water on olivine stability in tholeiites and the production of silica-saturated magmas in the island arc environment. J Geol 81:285-300

O'Hara MJ (1965) Primary magmas and the orign of basalts. Scott J Geol 1:19-40

Parman SW, Grove TL (2004) Harzburgite melting with and without H_2O: Experimental data and predictive modeling. J Geophys Res 109(B2):B02201

Pickering-Witter J, Johnston A (2000) The effects of variable bulk composition on the melting systematics of fertile peridotitic assemblages. Contrib Mineral Petrol 140:190-211

Presnall DC (1966) Join forsterite-diopside-iron oxide and its bearing on crystallization of basaltic and ultramafic magmas. Am J Sci 264(10):753-809

Schwab B, Johnston A (2001) Melting systematics of modally variable, compositionally intermediate peridotites and the effects of mineral fertility. J Petrol 42(10):1789-1811

Straub SM, LaGatta AB, Martin-Del Pozzo AL, Langmuir CH (2008) Evidence from high-Ni olivines for a hybridized peridotite/pyroxenite source for orogenic andesites from the central Mexican Volcanic Belt. Geochem Geophys Geosyst 9(3)

Streck MJ, Leeman WP, Chesley J (2007) High-magnesian andesite from Mount Shasta: A product of magma mixing and contamination, not a primitive mantle melt. Geology 35(4):351-354

Tatsumi Y (1982) Origin of high-magnesian andesites in the Setouchi volcanic belt, southwest Japan, II. Melting phase relations at high pressures. Earth Planet Sci Lett 60:305-317

van Keken PE, Currie C, King SD, Behn MD, Cagnioncle A, He J, Katz RF, Lin S-C, Parmentier EM, Spiegelman M (2008) A community benchmark for subduction zone modeling. Phys Earth Planet Inter 171(1-4):187-197

Weaver SL, Wallace PJ, Johnston AD (2011) A comparative study of continental vs. intraoceanic arc mantle melting: Experimentally determined phase relations of hydrous primitive melts. Earth Planet Sci Lett 308(1-2):97-106

Weber RM, Wallace PJ, Dana Johnston A (2011) Experimental insights into the formation of high-Mg basaltic andesites in the trans-Mexican volcanic belt. Contrib Mineral Petrol 165(5):825-840

Wood BJ, Bryndzia LT, Johnson KE (1990) Mantle oxidation-state and its relationship to tectonic environment and fluid speciation. Science 248(4953):337-345

Wyllie PJ (1971) Role of water in magma generation and initiation of diapiric uprise in the mantle. J Geophys Res 76(1328-1338)

Yoder HS, Tilley CE (1962) Origin of basalt magmas: An experimental study of natural and synthetic rock systems. J Petrol 3(3):342-532

Chapter III

Asimow, P.D., Ghiorso, M.S., 1998. Algorithmic modifications extending MELTS to calculate subsolidus phase relations. Am Mineral 83, 1127-1132.

Asimow, P.D., Longhi, J., 2004. The significance of multiple saturation points in the context of polybaric near-fractional melting. J Petrol 45, 2349-2367.

Baker, M.B., Grove, T.L., Price, R., 1994. Primitive basalts and andesites from the Mt Shasta Region, N California - products of varying melt fraction and water-content. Contrib Mineral Petrol 118, 111-129.

Baker, M.B., Stolper, E.M., 1994. Determining the composition of high-pressure mantle melts using diamond aggregates. Geochim Cosmochim Acta 58, 2811-2827.

Barr, J.A., Grove, T.L., 2010. AuPdFe ternary solution model and applications to understanding the fO_2 of hydrous, high-pressure experiments. Contrib Mineral Petrol 160, 631-643.

Byers, F.M.J., 1959. Geology of Umnak and Bogoslof Islands, Aleutian Islands, Alaska. U.S. Geological Survey Bulletin 1028-L, 267-369.

Cagnioncle, A.M., Parmentier, E.M., Elkins-Tanton, L.T., 2007. Effect of solid flow above a subducting slab on water distribution and melting at convergent plate boundaries. J Geophys Res 112, B09402.

Cooper, L.B., Plank, T., Arculus, R.J., Hauri, E.H., Hall, P.S., Parman, S.W., 2010. High-Ca boninites from the active Tonga Arc. J Geophys Res 115.

Dewey, M.R., 1996. The effect of H_2O on the near-liquidus phase relations on an Aleutian high magnesia basalt. M.S. thesis, Geological Sciences, University of Oregon

Draper, D.S., Johnston, A.D., 1992. Anhydrous PT-phase relations of an Aleutian high-MgO basalt: an investigation of the role of olivine-liquid reaction in the generation of arc high-alumina basalts. Contrib Mineral Petrol 112, 501-519.

Elkins-Tanton, L.T., Grove, T.L., Donnelly-Nolan, J., 2001. Hot, shallow mantle melting under the Cascades volcanic arc. Geology 29, 631-634.

England, P.C., Katz, R.F., 2010. Melting above the anhydrous solidus controls the location of volcanic arcs. Nature 468, E6-E7.

Falloon, T.J., Danyushevsky, L.V., 2000. Melting of refractory mantle at 1.5, 2 and 2.5 GPa under, anhydrous and H_2O-undersaturated conditions: Implications for the petrogenesis of high-Ca boninites and the influence of subduction components on mantle melting. J Petrol 41, 257-283.

Ghiorso, M.S., Carmichael, I.S.E., Rivers, M.L., Sack, R.O., 1983. The Gibbs free-energy of mixing of natural silicate liquids - an expanded regular solution approximation for the calculation of magmatic intensive variables. Contrib Mineral Petrol 84, 107-145.

Ghiorso, M.S., Hirschmann, M.M., Reiners, P.W., Kress, V.C., 2002. The pMELTS: A revision of MELTS for improved calculation of phase relations and major element partitioning related to partial melting of the mantle to 3 GPa. Geochem Geophys Geosyst 3, doi: 10.1029/2001gc000217.

Ghiorso, M.S., Sack, R.O., 1995. Chemical mass-transfer in magmatic processes. IV. A revised and internally consistent thermodynamic model for the interpolation and extrapolation of liquid-solid equilibria in magmatic systems at elevated temperatures and pressures. Contrib Mineral Petrol 119, 197-212.

Grove, T., Elkins-Tanton, L., Parman, S., 2003. Fractional crystallization and mantle-melting controls on calc-alkaline differentiation trends. Contrib Mineral Petrol 145(5) 515-533.

Grove, T., Parman, S., Bowring, S., Price, R., Baker, M., 2002. The role of an H_2O-rich fluid component in the generation of primitive basaltic andesites and andesites from the Mt. Shasta region, N California. Contrib Mineral Petrol 142, 375-396.

Grove, T.L., Chatterjee, N., Parman, S.W., Médard, E., 2006. The influence of H_2O on mantle wedge melting. Earth Planet Sci Lett 249, 74-98.

Hall, P.S., Cooper, L.B., Plank, T., 2010. Mantle flow, melting, and the evolution of the sub-arc mantle in the Lau Basin - Tonga Arc system. AGU Fall Meeting.

Hasenaka, T., Carmichael, I.S.E., 1985a. The cinder cones of Michoacan-Guanajuato, Central Mexico: Their age, volume and distribution, and magma discharge rate. J Volcanol Geotherm Res 25, 105-124.

Hasenaka, T., Carmichael, I.S.E., 1985b. A compilation of location, size, and geomorphological parameters of volcanoes of the Michoacan-Guanajuato Volcanic Field, Central Mexico. Geofis Int 24, 577-607.

Hasenaka, T., Carmichael, I.S.E., 1987. The cinder cones of Michoacan-Guanajuato, central Mexico: petrology and chemistry. J Petrol 28, 241-269.

Hesse, M., Grove, T.L., 2003. Absarokites from the western Mexican Volcanic Belt: constraints on mantle wedge conditions. Contrib Mineral Petrol 146, 10-27.

Hirose, K., Kawamoto, T., 1995. Hydrous partial melting of lherzolite at 1 GPa: the effect of H_2O on the genesis of basaltic magmas. Earth Planet Sci Lett 133, 463-473.

Hirose, K., Kushiro, I., 1993. Partial melting of dry peridotites at high-pressures - determination of compositions of melts segregated from peridotite using aggregates of diamond. Earth Planet Sci Lett 114, 477-489.

Huebner, J.S., Sato, M., 1970. Oxygen fugacity-temperature relationships of manganese oxide and nickel oxide buffers. Am Mineral 55, 934-952.

Johnson, E.R., Wallace, P.J., Cashman, K.V., Granados, H.D., Kent, A.J.R., 2008. Magmatic volatile contents and degassing-induced crystallization at Volcán Jorullo, Mexico: Implications for melt evolution and the plumbing systems of monogenetic volcanoes. Earth Planet Sci Lett 269, 478-487.

Johnson, E.R., Wallace, P.J., Delgado Granados, H., Manea, V.C., Kent, A.J.R., Bindeman, I.N., Donegan, C.S., 2009. Subduction-related volatile recycling and magma generation beneath Central Mexico: Insights from melt inclusions, oxygen isotopes and geodynamic models. J Petrol 50, 1729-1764.

Katz, R.F., Spiegelman, M., Langmuir, C.H., 2003. A new parameterization of hydrous mantle melting. Geochem Geophys Geosyst 4, doi: 10.1029/2002gc000433.

Kay, S.M., Kay, R.W., Citron, G.P., 1982. Tectonic controls on tholeiitic and calc-alkaline magmatism in the Aleutian arc. J Geophys Res 87, 4051-4072.

Kelemen, P., Dick, H., Quick, J., 1992. Formation of harzburgite by pervasive melt/rock reaction in the upper mantle. Nature 358, 356-641.

Kelemen, P.B., Rilling, J.L., Parmentier, E.M., Mehl, L., Hacker, B., 2003a. Thermal structure due to solid-state flow in the mantle wedge beneath arcs, Inside the Subduction Factory. American Geophysical Union, pp. 293-311.

Kelemen, P.B., Yogodzinski, G.M., Scholl, D.W., 2003b. Along-strike variation in lavas of the Aleutian Island Arc: Implications for the genesis of high Mg# andesite and the continental crust, Inside the Subduction Factory. American Geophysical Union, pp. 223-276.

Kogiso, T., Hirschmann, M.M., Pertermann, M., 2004. High-pressure partial melting of mafic lithologies in the mantle. J Petrol 45, 2407-2422.

Kress, V.C., Carmichael, I.S.E., 1991. The compressibility of silicate liquids containing Fe_2O_3 and the effect of composition, temperature, oxygen fugacity and pressure on their redox states. Contrib Mineral Petrol 108, 82-92.

Kushiro, I., 1972. Effect of water on composition of magmas formed at high-pressures. J Petrol 13, 311-334.

Kushiro, I., 1996. Partial melting of a fertile mantle peridotite at high pressures: an experimental study using aggregates of diamond, in: Basu, A., Hart, S. (Eds.), Earth Processes: Reading the Isotopic Code. American Geophysical Union, Washington, DC, pp. 109-122.

Lee, C.-T.A., Luffi, P., Plank, T., Dalton, H., Leeman, W.P., 2009. Constraints on the depths and temperatures of basaltic magma generation on Earth and other terrestrial planets using new thermobarometers for mafic magmas. Earth Planet Sci Lett 279, 20-33.

Luhr, J.F., 1997. Extensional tectonics and the diverse primitive volcanic rocks in the western Mexican Volcanic Belt. Can Mineral 35, 473-500.

Luhr, J.F., Allan, J.F., Carmichael, I.S.E., Nelson, S.A., Hasenaka, T., 1989. Primitive calc-alkaline and alkaline rock types from the Western Mexican Volcanic Front. J Geophys Res 94, 4515-4530.

Luhr, J.F., Carmichael, I.S.E., 1985. Jorullo Volcano, Michoacan, Mexico (1759-1774): The earliest stages of fractionation in calc-alkaline magmas. Contrib Mineral Petrol 90, 142-161.

Manea, V., Manea, M., Kostoglodov, V., Sewell, G., 2005. Thermo-mechanical model of the mantle wedge in Central Mexican subduction zone and a blob tracing approach for the magma transport. Phys Earth Planet Inter 149, 165-186.

Manea, V.C., Manea, M., Kostoglodov, V., Currie, C.A., Sewell, G., 2004. Thermal structure, coupling and metamorphism in the Mexican subduction zone beneath Guerrero. Geophys J Int 158, 775-784.

McCarron, J.J., Smellie, J.L., 1998. Tectonic implications of fore-arc magmatism and generation of high-magnesian andesites: Alexander Island, Antarctica. J Geol Soc 155, 269-280.

Médard, E., Grove, T.L., 2008. The effect of H_2O on the olivine liquidus of basaltic melts: experiments and thermodynamic models. Contrib Mineral Petrol 155, 417-432.

Mercer, C.N., Johnston, A.D., 2007. Experimental studies of the P–T–H_2O near-liquidus phase relations of basaltic andesite from North Sister Volcano, High Oregon Cascades: constraints on lower-crustal mineral assemblages. Contrib Mineral Petrol 155, 571-592.

Muntener, O., Ulmer, P., 2006. Experimentally derived high-pressure cumulates from hydrous arc magmas and consequences for the seismic velocity structure of lower arc crust. Geophys Res Lett 33, L21308 doi: 21310.21029/22006gl027629.

Newman, S., Lowenstern, J.B., 2002. VolatileCalc: A silicate melt-H_2O-CO_2 solution model written in VISUAL BASIC for Excel. Comput Geosci 28, 597-604.

Nye, C.J., Reid, M.R., 1986. Geochemistry of primary and least fractionated lavas from Okmok Volcano, central Aleutians; implications for arc magmagenesis. J Geophys Res 91, 10271-10287.

Ortega-Gutierrez, F., Elias-Herrera, M., Guadalupe Davalos-Elizondo, M., 2008. On the nature and role of the lower crust in the volcanic front of the Trans-Mexican Volcanic Belt and its fore-arc region, southern and central Mexico. Rev Mex Cienc Geol 25, 346-364.

Parman, S.W., Grove, T.L., 2004. Harzburgite melting with and without H_2O: Experimental data and predictive modeling. J Geophys Res 109, B02201.

Peacock, S., Wang, K., 1999. Seismic consequences of warm versus cool subduction metamorphism: Examples from southwest and northeast Japan. Science 286, 937-939.

Peacock, S.M., 1991. Numerical-simulation of subduction zone pressure temperature time paths - constraints on fluid production and arc magmatism. Philos Trans R Soc Lond 335, 341-353.

Pichavant, M., Macdonald, R., 2007. Crystallization of primitive basaltic magmas at crustal pressures and genesis of the calc-alkaline igneous suite: experimental evidence from St Vincent, Lesser Antilles arc. Contrib Mineral Petrol 154, 535-558.

Pichavant, M., Mysen, B.O., Macdonald, R., 2002. Source and H_2O content of high-MgO magmas in island arc settings: An experimental study of a primitive calc-alkaline basalt from St. Vincent, Lesser Antilles Arc. Geochim Cosmochim Acta 66, 2193-2209.

Pickering, J.M., Schwab, B.E., Johnston, A.D., 1998. Off-center hot spots: Double thermocouple determination of the thermal gradient in a 1.27 cm (1/2 in) CaF_2 piston-cylinder furnace assembly. Am Mineral 83, 228-235.

Pickering-Witter, J., Johnston, A., 2000. The effects of variable bulk composition on the melting systematics of fertile peridotitic assemblages. Contrib Mineral Petrol 140, 190-211.

Portnyagin, M., Hoernle, K., Plechov, P., Mironov, N., Khubunaya, S., 2007. Constraints on mantle melting and composition and nature of slab components in volcanic arcs from volatiles (H_2O, S, Cl, F) and trace elements in melt inclusions from the Kamchatka Arc. Earth Planet Sci Lett 255, 53-69.

Roman, D.C., Cashman, K.V., Gardner, C.A., Wallace, P.J., Donovan, J.J., 2006. Storage and interaction of compositionally heterogeneous magmas from the 1986 eruption of Augustine Volcano, Alaska. Bull Vol 68, 240-254.

Schwab, B., Johnston, A., 2001. Melting systematics of modally variable, compositionally intermediate peridotites and the effects of mineral fertility. J Petrol 42, 1789-1811.

Shillington, D.J., Van Avendonk, H.J.A., Holbrook, W.S., Kelemen, P.B., Hornbach, M.J., 2004. Composition and structure of the central Aleutian island arc from arc-parallel wide-angle seismic data. Geochem Geophys Geosyst 5.

Sobolev, A.V., Danyushevsky, L.V., 1994. Petrology and geochemistry of boninites from the north termination of the Tonga trench - constraints on the generation conditions of primary high-Ca boninite magmas. J Petrol 35, 1183-1211.

Straub, S.M., LaGatta, A.B., Martin-Del Pozzo, A.L., Langmuir, C.H., 2008. Evidence from high-Ni olivines for a hybridized peridotite/pyroxenite source for orogenic andesites from the central Mexican Volcanic Belt. Geochem Geophys Geosyst 9.

Streck, M.J., Leeman, W.P., Chesley, J., 2007. High-magnesian andesite from Mount Shasta: A product of magma mixing and contamination, not a primitive mantle melt. Geology 35, 351-354.

Sugawara, T., 2000. Empirical relationships between temperature, pressure, and MgO content in olivine and pyroxene. J Geophys Res 105, 8457-8472.

Syracuse, E.M., van Keken, P.E., Abers, G.A., 2010. The global range of subduction zone thermal models. Phys Earth Planet Inter 183(1-2), 73-90.

Toplis, M.J., 2005. The thermodynamics of iron and magnesium partitioning between olivine and liquid: criteria for assessing and predicting equilibrium in natural and experimental systems. Contrib Mineral Petrol 149, 22-39.

Ulmer, P., 2007. Differentiation of mantle-derived calc-alkaline magmas at mid to lower crustal levels: experimental and petrologic constraints. Period Mineral 76, 309-325.

van Keken, P.E., 2003. The structure and dynamics of the mantle wedge. Earth Planet Sci Lett 215, 323-338.

van Keken, P.E., Kiefer, B., Peacock, S.M., 2002. High-resolution models of subduction zones: Implications for mineral dehydration reactions and the transport of water into the deep mantle. Geochem Geophys Geosyst 3, doi: 10.1029/2001gc000256.

van Keken, P.E., Syracuse, E.M., Hacker, B.H., Abers, G.A., Fischer, K.M., Kneller, E.A., Spiegelman, M., 2009. Modeling the subduction factory: The ins and outs from a thermal and dynamical perspective. Geochim Cosmochim Acta 73, A1372-A1372.

Wada, I., Wang, K., 2009. Common depth of slab-mantle decoupling: Reconciling diversity and uniformity of subduction zones. Geochem Geophys Geosyst 10.

Wallace, P., Carmichael, I.S.E., 1999. Quaternary volcanism near the Valley of Mexico: implications for subduction zone magmatism and the effects of crustal thickness variations on primitive magma compositions. Contrib Mineral Petrol 135, 291-314.

Wallace, P.J., 2005. Volatiles in subduction zone magmas: concentrations and fluxes based on melt inclusion and volcanic gas data. J Volcanol Geotherm Res 140, 217-240.

Weaver, S., 2007. P-T-H_2O phase relations of an Aleutian, high MgO basalt: results from hydrous experimental studies and thermodynamic modeling. Department of Geological Sciences, University of Oregon.

Weber, R.M., Wallace, P.J., Dana Johnston, A., 2011. Experimental insights into the formation of high-Mg basaltic andesites in the trans-Mexican volcanic belt. Contrib Mineral Petrol 165, 825-840.

Wood, B.J., Turner, S.P., 2009. Origin of primitive high-Mg andesite: Constraints from natural examples and experiments. Earth Planet Sci Lett 283, 59-66.

Zimmer, M.M., Plank, T., Hauri, E.H., Yogodzinski, G.M., Stelling, P., Larsen, J., Singer, B., Jicha, B., Mandeville, C., Nye, C.J., 2010. The role of water in generating the calc-alkaline trend: New volatile data for Aleutian magmas and a new tholeiitic index. J Petrol 51, 2411-2444.

Chapter IV

Allan JF, Carmichael ISE (1984) Lamprophyric lavas in the Colima Graben, SW Mexico. Contrib Mineral Petrol 88(3):203-216

Arima M, Edgar AD (1983) High-pressure experimental studies on a katungite and their bearing on the genesis of some potassium-rich magmas of the west branch of the African rift. J Petrol 24(2):166-187

Asimow PD, Ghiorso MS (1998) Algorithmic modifications extending MELTS to calculate subsolidus phase relations. Am Mineral 83(9-10):1127-1132

Asimow PD, Longhi J (2004) The significance of multiple saturation points in the context of polybaric near-fractional melting. J Petrol 45(12):2349-2367

Baker MB, Grove TL, Price R (1994) Primitive basalts and andesites from the Mt Shasta Region, N California - products of varying melt fraction and water-content. Contrib Mineral Petrol 118(2):111-129

Barclay J, Carmichael I (2004) A hornblende basalt from western Mexico: Water-saturated phase relations constrain a pressure-temperature window of eruptibility. J Petrol 45(3):485-506

Barr JA, Grove TL (2010) AuPdFe ternary solution model and applications to understanding the fO_2 of hydrous, high-pressure experiments. Contrib Mineral Petrol 160(5):631-643

Bottazzi P, Tiepolo M, Vannucci R, Zanetti A, Brumm R, Foley SF, Oberti R (1999) Distinct site preferences for heavy and light REE in amphibole and the prediction of $^{Amph/L}D/_{REE}$. Contrib Mineral Petrol 137(1-2):36-45

Carmichael I, Lange R, Luhr J (1996) Quaternary minettes and associated volcanic rocks of Mascota, western Mexico: A consequence of plate extension above a subduction modified mantle wedge. Contrib Mineral Petrol 124:302-333

Cervantes P, Wallace P (2003) Role of H_2O in subduction-zone magmatism: New insights from melt inclusions in high-Mg basalts from central Mexico. Geology 31(3):235-238

Conceicao RV, Green DH (2004) Derivation of potassic (shoshonitic) magmas by decompression melting of phlogopite plus pargasite lherzolite. Lithos 72(3-4):209-229

Conticelli S, Peccerillo A (1992) Petrology and geochemistry of potassic and ultrapotassic volcanism in central Italy - Petrogenesis and inferences on the evolution of the mantle sources. Lithos 28:221-240

Cooper LB, Ruscitto DM, Plank T, Wallace PJ, Syracuse EM, Manning CE (2012) Global variations in H_2O/Ce: 1. Slab surface temperatures beneath volcanic arcs. Geochem Geophy Geosyst 13

Dixon JE, Pan V (1995) Determination of the molar absorptivity of dissolved carbonate in basanitic glass. Am Mineral 80(11-12):1339-1342

Dixon JE, Stolper EM, Holloway JR (1995) An experimental study of water and carbon dioxide solubilities in mid ocean ridge basaltic liquids. 1. Calibration and solubility models. J Petrol 36(6):1607-1631

Edgar AD, Condliffe E (1978) Derivation of K-rich ultramafic magmas from a peridotitic mantle source. Nature 275(5681):639-640

Edgar AD, Condliffe E, Barnett RL, Shirran RJ (1980) An experimental study of an olivine ugandite magma and mechanisms for the formation of its K-enriched derivatives. J Petrol 21(3):475-497

Eggler DH (1974) Effects of CO_2 on the melting of peridotite. CIWYB 73:215-224

Elkins-Tanton LT, Grove T (2003) Evidence for deep melting of hydrous metasomatized mantle: Pliocene high-potassium magmas from the Sierra Nevadas. J Geophys Res 108(B7)

Esperança S, Holloway JR (1987) On the origin of some mica-lamprophyres - Experimental evidence from a mafic minette. Contrib Mineral Petrol 95(2):207-216

Ferrari L, Petrone CM, Francalanci L (2001) Generation of oceanic-island basalt-type volcanism in the western Trans-Mexican volcanic belt by slab rollback, asthenosphere infiltration, and variable flux melting. Geology 29(6):507-510

Foley S (1992) Vein-plus-wall-rock melting mechanisms in the lithosphere and the origin of potassic alkaline magmas. Lithos 28:435-453

Funk SP, Luth RW (2012) An experimental study of a minette from the Milk River area, southern Alberta, Canada. Contrib Mineral Petrol:1-11

Gaetani G, Grove T (1998) The influence of water on melting of mantle peridotite. Contrib Mineral Petrol 131:323-346

Ghiorso MS, Hirschmann MM, Reiners PW, Kress VC (2002) The pMELTS: A revision of MELTS for improved calculation of phase relations and major element partitioning related to partial melting of the mantle to 3 GPa. Geochem Geophys Geosyst 3(1030):doi: 10.1029/2001gc000217

Ghiorso MS, Sack RO (1995) Chemical mass-transfer in magmatic processes. IV. A revised and internally consistent thermodynamic model for the interpolation and extrapolation of liquid-solid equilibria in magmatic systems at elevated temperatures and pressures. Contrib Mineral Petrol 119(2-3):197-212

Grove T, Parman S, Bowring S, Price R, Baker M (2002) The role of an H_2O-rich fluid component in the generation of primitive basaltic andesites and andesites from the Mt. Shasta region, N California. Contrib Mineral Petrol 142(4):375-396

Hacker BR, Peacock SM, Abers GA, Holloway SD (2003) Subduction factory - 2. Are intermediate-depth earthquakes in subducting slabs linked to metamorphic dehydration reactions? J Geophys Res 108(B1):Doi 10.1029/2001jb001129

Hall LJ, Brodie J, Wood BJ, Carroll MR (2004) Iron and water losses from hydrous basalts contained in $Au_{80}Pd_{20}$ capsules at high pressure and temperature. Mineral Mag 68(1):75-81

Hasenaka T, Carmichael ISE (1985) The cinder cones of Michoacan-Guanajuato, Central Mexico: Their age, volume and distribution, and magma discharge rate. J Volcanol Geotherm Res 25:105-124

Hasenaka T, Carmichael ISE (1987) The cinder cones of Michoacan-Guanajuato, central Mexico: petrology and chemistry. J Petrol 28(2):241-269

Hervig RL, Mazdab FK, Moore G, McMillan PF (2003) Analyzing hydrogen (H_2O) in silicate glass by secondary ion mass spectrometry and reflectance Fourier transform infrared spectroscopy. In: DeVivo B, Bodnar R (eds) Melt Inclusions in Volcanic Systems, vol 5. Elsevier, Amsterdam, pp 83-103

Hesse M, Grove TL (2003) Absarokites from the western Mexican Volcanic Belt: constraints on mantle wedge conditions. Contrib Mineral Petrol 146(1):10-27

Huebner JS, Sato M (1970) Oxygen fugacity-temperature relationships of manganese oxide and nickel oxide buffers. Am Mineral 55(5-6):934-952

Johnson ER, Kamenetsky VS, McPhie J, Wallace PJ (2011) Degassing of the H_2O-rich rhyolites of the Okataina Volcanic Center, Taupo Volcanic Zone, New Zealand. Geology 39(4):311-314

Johnson ER, Wallace PJ, Cashman KV, Granados HD, Kent AJR (2008) Magmatic volatile contents and degassing-induced crystallization at Volcán Jorullo, Mexico: Implications for melt evolution and the plumbing systems of monogenetic volcanoes. Earth Planet Sci Lett 269(3-4):478-487

Johnson ER, Wallace PJ, Delgado Granados H, Manea VC, Kent AJR, Bindeman IN, Donegan CS (2009) Subduction-related volatile recycling and magma generation beneath Central Mexico: Insights from melt inclusions, oxygen isotopes and geodynamic models. J Petrol 50(9):1729-1764

Kagi R, Muntener O, Ulmer P, Ottolini L (2005) Piston-cylinder experiments on H_2O undersaturated Fe-bearing systems: An experimental setup approaching fO_2 conditions of natural calc-alkaline magmas. Am Mineral 90(4):708-717

Kessel R, Schmidt MW, Ulmer P, Pettke T (2005) Trace element signature of subduction-zone fluids, melts and supercritical liquids at 120-180 km depth. Nature 437(7059):724-727

Kuritani T, Yokoyama T, Nakamura E (2008) Generation of rear-arc magmas induced by influx of slab-derived supercritical liquids: Implications from alkali basalt lavas from Rishiri Volcano, Kurile arc. J Petrol 49(7):1319-1342

Lange RA, Carmichael ISE (1990) Hydrous basaltic andesites associated with minette and related lavas in western Mexico. J Petrol 31(6):1225-1259

Lange RA, Carmichael ISE (1991) A potassic volcanic front in western Mexico - the lamprophyric and related lavas of San Sebastian. Geol Soc Am Bull 103(7):928-940

Latourrette T, Hervig RL, Holloway JR (1995) Trace-element partitioning between amphibole, phlogopite, and basanite melt. Earth Planet Sci Lett 135(1-4):13-30

Lee C-TA, Luffi P, Plank T, Dalton H, Leeman WP (2009) Constraints on the depths and temperatures of basaltic magma generation on Earth and other terrestrial planets using new thermobarometers for mafic magmas. Earth Planet Sci Lett 279(1-2):20-33

Luhr JF (1997) Extensional tectonics and the diverse primitive volcanic rocks in the western Mexican Volcanic Belt. Can Mineral 35:473-500

Luhr JF (2001) Glass inclusions and melt volatile contents at Paricutin Volcano, Mexico. Contrib Mineral Petrol 142(3):261-283

Luhr JF, Allan JF, Carmichael ISE, Nelson SA, Hasenaka T (1989) Primitive calc-alkaline and alkaline rock types from the Western Mexican Volcanic Front. J Geophys Res 94(B4):4515-4530

Luhr JF, Carmichael ISE (1981) The Colima Volcanic Complex, Mexico .2. Late-Quaternary Cinder Cones. Contrib Mineral Petrol 76(2):127-147

Luhr JF, Carmichael ISE (1985) Jorullo Volcano, Michoacan, Mexico (1759-1774): The earliest stages of fractionation in calc-alkaline magmas. Contrib Mineral Petrol 90:142-161

Ma GSK, Malpas J, Xenophontos C, Chan GHN (2011) Petrogenesis of latest Miocene-Quaternary continental intraplate volcanism along the northern Dead Sea fault system (Al Ghab-Homs Volcanic Field), western Syria: Evidence for lithosphere-asthenosphere interaction. J Petrol 52(2):401-430

Maria AH, Luhr JF (2008) Lamprophyres, basanites, and basalts of the western Mexican Volcanic Belt: volatile contents and a vein-wallrock melting relationship. J Petrol 49(12):2123-2156

Marquez A, Oyarzun R, Dobias M, Verma SP (1999) Alkalic (ocean-island basalt type) and calc-alkalic volcanism in the Mexican volcanic belt: A case for plume-related magmatism and propagating rifting at an active margin? Geology 27(1):51-54

Médard E, Grove TL (2007) The effect of H_2O on the olivine liquidus of basaltic melts: experiments and thermodynamic models. Contrib Mineral Petrol 155(4):417-432

Meriggi L, Macias JL, Tommasini S, Capra L, Conticelli S (2008) Heterogeneous magmas of the Quaternary Sierra Chichinautzin volcanic field (central Mexico): the role of an amphibole-bearing mantle and magmatic evolution processes. Rev Mex Cien Geol 25(2):197-216

Modreski PJ, Boettcher AL (1973) Phase relationships of phlogopite in the system K_2O-MgO-CaO-Al_2O_3-SiO_2-H_2O to 35-Kilobars - A better model for micas in the interior of the earth. Am J Sci 273(5):385-414

Mori L, Gomez-Tuena A, Schaaf P, Goldstein SL, Perez-Arvizu O, SolIs-Pichardo G (2009) Lithospheric Removal as a Trigger for Flood Basalt Magmatism in the Trans-Mexican Volcanic Belt. J Petrol 50(11):2157-2186

Morrison GW (1980) Characteristics and tectonic setting of the shoshonite rock association. Lithos 13(1):97-108

Newman S, Lowenstern JB (2002) VolatileCalc: A silicate melt-H_2O-CO_2 solution model written in VISUAL BASIC for Excel. Comput Geosci 28(5):597-604

Nicholls I, Whitford D (1983) Potassium-rich volcanic rocks of the Muriah complex, Java, Indonesia: Products of multiple magma sources? J Volcanol Geotherm Res 18(1-4):337-359

Ortega-Gutierrez F, Elias-Herrera M, Guadalupe Davalos-Elizondo M (2008) On the nature and role of the lower crust in the volcanic front of the Trans-Mexican Volcanic Belt and its fore-arc region, southern and central Mexico. Rev Mex Cienc Geol 25(2):346-364

Pardo M, Suarez G (1995) Shape of the subducted Rivera and Cocos plates in Southern Mexico - Seismic and tectonic tmplications. J Geophys Res 100(B7):12357-12373

Pickering JM, Schwab BE, Johnston AD (1998) Off-center hot spots: Double thermocouple determination of the thermal gradient in a 1.27 cm (1/2 in) CaF_2 piston-cylinder furnace assembly. Am Mineral 83:228-235

Plank T, Cooper LB, Manning CE (2009) Emerging geothermometers for estimating slab surface temperatures. Nat Geosci 2(9):611-615

Righter K, Rosas-Elguera J (2001) Alkaline lavas in the volcanic front of the western Mexican Volcanic Belt: Geology and petrology of the Ayutla and Tapalpa volcanic fields. J Petrol 42(12):2333-2361

Salters VJM, Stracke A (2004) Composition of the depleted mantle. Geochem Geophy Geosyst 5

Schmidt MW, Poli S (1998) Experimentally based water budgets for dehydrating slabs and consequences for arc magma generation. Earth Planet Sci Lett 163(1-4):361-379

Sorbadere F, Schiano P, Metrich N, Garaebiti E (2011) Insights into the origin of primitive silica-undersaturated arc magmas of Aoba volcano (Vanuatu arc). Contrib Mineral Petrol 162(5):995-1009

Tatsumi Y, Koyaguchi T (1989) An absarokite from a phlogopite Iherzolite source. Contrib Mineral Petrol 102(1):34-40

Toplis MJ (2004) The thermodynamics of iron and magnesium partitioning between olivine and liquid: criteria for assessing and predicting equilibrium in natural and experimental systems. Contrib Mineral Petrol 149(1):22-39

Verma SP, Hasenaka T (2004) Sr, Nd, and Pb isotopic and trace element geochemical constraints for a veined-mantle source of magmas in the Michoacán-Guanajuato Volcanic Field, west-central Mexican Volcanic Belt. Geochem J Jap 38(1):43-66

Vigouroux N, Wallace PJ, Kent AJR (2008) Volatiles in high-K magmas from the western Trans-Mexican Volcanic Belt: Evidence for fluid fluxing and extreme enrichment of the mantle wedge by subduction processes. J Petrol 49(9):1589-1618

Wallace P, Carmichael ISE (1989) Minette lavas and associated leucitites from the western front of the Mexican Volcanic Belt - Petrology, chemistry, and origin. Contrib Mineral Petrol 103(4):470-492

Wallace P, Carmichael ISE (1999) Quaternary volcanism near the Valley of Mexico: implications for subduction zone magmatism and the effects of crustal thickness variations on primitive magma compositions. Contrib Mineral Petrol 135(4):291-314

Wallace P, Carmichael ISE, Righter K, Becker TA (1992) Volcanism and tectonism in Western Mexico - A contrast of style and substance. Geology 20(7):625-628

Weaver SL, Wallace PJ, Johnston AD (2011) A comparative study of continental vs. intraoceanic arc mantle melting: Experimentally determined phase relations of hydrous primitive melts. Earth Planet Sci Lett 308(1-2):97-106

Weber RM, Wallace PJ, Dana Johnston A (2011) Experimental insights into the formation of high-Mg basaltic andesites in the trans-Mexican volcanic belt. Contrib Mineral Petrol 165(5):825-840

Yang T, Grand SP, Wilson D, Guzman-Speziale M, Gomez-Gonzalez JM, Dominguez-Reyes T, Ni J (2009) Seismic structure beneath the Rivera subduction zone from finite-frequency seismic tomography. J Geophys Res 114

Chapter V

Barclay J, Carmichael I (2004) A hornblende basalt from western Mexico: Water-saturated phase relations constrain a pressure-temperature window of eruptibility. J Petrol 45(3):485-506

England PC, Katz RF (2010) Melting above the anhydrous solidus controls the location of volcanic arcs. Nature 468(7325):E6-E7

Ferrari L, Orozco-Esquivel T, Manea M (2012) The dynamic history of the Trans-Mexican Volcanic Belt and the Mexico subduction zone. Tectonophysics 522-523:122-149

Ghiorso MS, Hirschmann MM, Reiners PW, Kress VC (2002) The pMELTS: A revision of MELTS for improved calculation of phase relations and major element partitioning related to partial melting of the mantle to 3 GPa. Geochem Geophys Geosyst 3(1030):doi: 10.1029/2001gc000217

Hesse M, Grove TL (2003) Absarokites from the western Mexican Volcanic Belt: constraints on mantle wedge conditions. Contrib Mineral Petrol 146(1):10-27

Hirschmann MM, Kogiso T, Baker MB, Stolper EM (2003) Alkalic magmas generated by partial melting of garnet pyroxenite. Geology 31(6):481-484

Johnson ER, Wallace PJ, Delgado Granados H, Manea VC, Kent AJR, Bindeman IN, Donegan CS (2009) Subduction-related volatile recycling and magma generation beneath Central Mexico: Insights from melt inclusions, oxygen isotopes and geodynamic models. J Petrol 50(9):1729-1764

Kogiso T, Hirschmann MM, Pertermann M (2004) High-pressure partial melting of mafic lithologies in the mantle. J Petrol 45(12):2407-2422

Lee C-TA, Luffi P, Plank T, Dalton H, Leeman WP (2009) Constraints on the depths and temperatures of basaltic magma generation on Earth and other terrestrial planets using new thermobarometers for mafic magmas. Earth Planet Sci Lett 279(1-2):20-33

Sugawara T (2000) Empirical relationships between temperature, pressure, and MgO content in olivine and pyroxene. J Geophys Res 105(B4):8457-8472

Wallace P, Carmichael ISE (1999) Quaternary volcanism near the Valley of Mexico: implications for subduction zone magmatism and the effects of crustal thickness variations on primitive magma compositions. Contrib Mineral Petrol 135(4):291-314

Weaver SL, Wallace PJ, Johnston AD (2011) A comparative study of continental vs. intraoceanic arc mantle melting: Experimentally determined phase relations of hydrous primitive melts. Earth Planet Sci Lett 308(1-2):97-106

Weber RM, Wallace PJ, Dana Johnston A (2011) Experimental insights into the formation of high-Mg basaltic andesites in the trans-Mexican volcanic belt. Contrib Mineral Petrol 165(5):825-840

Wood BJ, Turner SP (2009) Origin of primitive high-Mg andesite: Constraints from natural examples and experiments. Earth Planet Sci Lett 283(1-4):59-66